Declassified and Approved For Release 2013/03/04 : CIA-RDP10-02196R000300010003-8

ISSN 0038-531X

Russian Original Vol. 53, No. 3, September, 1982

March, 1983

SATEAZ 53(3) 577-654 (1982)

SOVIET ATOMIC ENERGY

АТОМНАЯ ЭНЕРГИЯ
(ATOMNAYA ÉNERGIYA)

TRANSLATED FROM RUSSIAN

PEEL HERE

1

c/b CONSULTANTS BUREAU, NEW YORK

Declassified and Approved For Release 2013/03/04 : CIA-RDP10-02196R000300010003-8

Declassified and Approved For Release 2013/03/04 : CIA-RDP10-02196R000300010003-8

SOVIET ATOMIC ENERGY

Soviet Atomic Energy is abstracted or indexed in *Chemical Abstracts, Chemical Titles, Pollution Abstracts, Science Research Abstracts, Parts A and B, Safety Science Abstracts Journal, Current Contents, Energy Research Abstracts,* and *Engineering Index.*

Mailed in the USA by Publications Expediting, Inc., 200 Meacham Avenue, Elmont, NY 11003.

POSTMASTER: Send address changes to *Soviet Atomic Energy,* Plenum Publishing Corporation, 233 Spring Street, New York, NY 10013.

Soviet Atomic Energy is a translation of *Atomnaya Énergiya,* a publication of the Academy of Sciences of the USSR.

An agreement with the Copyright Agency of the USSR (VAAP) makes available both advance copies of the Russian journal and original glossy photographs and artwork. This serves to decrease the necessary time lag between publication of the original and publication of the translation and helps to improve the quality of the latter. The translation began with the first issue of the Russian journal.

Editorial Board of *Atomnaya Énergiya:*

Editor: O. D. Kazachkovskii

Associate Editors: N. A. Vlasov and N. N. Ponomarev-Stepnoi

Secretary: A. I. Artemov

I. N. Golovin
V. I. Il'ichev
V. F. Kalinin
P. L. Kirillov
Yu. I. Koryakin
E. V. Kulov
B. N. Laskorin
V. V. Matveev
I. D. Morokhov
A. A. Naumov
A. S. Nikiforov
A. S. Shtan'
B. A. Sidorenko
M. F. Troyanov
E. I. Vorob'ev

Copyright © 1983, Plenum Publishing Corporation. *Soviet Atomic Energy* participates in the program of Copyright Clearance Center, Inc. The appearance of a code line at the bottom of the first page of an article in this journal indicates the copyright owner's consent that copies of the article may be made for personal or internal use. However, this consent is given on the condition that the copier pay the stated per-copy fee through the Copyright Clearance Center, Inc. for all copying not explicitly permitted by Sections 107 or 108 of the U.S. Copyright Law. It does not extend to other kinds of copying, such as copying for general distribution, for advertising or promotional purposes, for creating new collective works, or for resale, nor to the reprinting of figures, tables, and text excerpts.

Consultants Bureau journals appear about six months after the publication of the original Russian issue. For bibliographic accuracy, the English issue published by Consultants Bureau carries the same number and date as the original Russian from which it was translated. For example, a Russian issue published in December will appear in a Consultants Bureau English translation about the following June, but the translation issue will carry the December date. When ordering any volume or particular issue of a Consultants Bureau journal, please specify the date and, where applicable, the volume and issue numbers of the original Russian. The material you will receive will be a translation of that Russian volume or issue.

Subscription (2 volumes per year)
Vols. 52 & 53: $440 (domestic); $489 (foreign)
Vols. 54 & 55: $500 (domestic); $555 (foreign)
Single Issue: $50
Single Article: $7.50

CONSULTANTS BUREAU, NEW YORK AND LONDON

c/b
233 Spring Street
New York, New York 10013

Published monthly. Second-class postage paid at Jamaica, New York 11431.

Declassified and Approved For Release 2013/03/04 : CIA-RDP10-02196R000300010003-8

Declassified and Approved For Release 2013/03/04 : CIA-RDP10-02196R000300010003-8

SOVIET ATOMIC ENERGY

A translation of *Atomnaya Énergiya*

March, 1983

Volume 53, Number 3 **September, 1982**

CONTENTS

Declassified and Approved For Release 2013/03/04 : CIA-RDP10-02196R000300010003-8

Declassified and Approved For Release 2013/03/04 : CIA-RDP10-02196R000300010003-8

CONTENTS

(continued)

Engl./Russ.

The Russian press date (podpisano k pechati) of this issue was 8/23/1982. Publication therefore did not occur prior to this date, but must be assumed to have taken place reasonably soon thereafter.

Declassified and Approved For Release 2013/03/04 : CIA-RDP10-02196R000300010003-8

Declassified and Approved For Release 2013/03/04 : CIA-RDP10-02196R000300010003-8

ARTICLES

DISTRIBUTED MICROPROCESSOR-BASED SYSTEM FOR MONITORING RADIATION IN NUCLEAR POWER PLANTS*

A. A. Denisov, V. S. Zhernov,
I. S. Krasheninnikov, V. V. Matveev,
N. V. Ryzhov, and V. M. Skatkin

UDC 621.317.794+621.039.564

Protection of the environment from anthropogenic actions is becoming a more urgent problem with each passing year. With the rapid growth of nuclear power, one of the complex and specific problems in this area is ecologically safe operation of nuclear electrical power plants, nuclear thermoelectrical power plants, AST, etc. The most important part of the problem is creating measuring and information gathering systems and control systems, which permit monitoring the changes in the environment due to the action of such objects, i.e., monitoring factors acting on the environment, evaluating the actual state of the environment at any given time, and forecasting the possible future effect.

The presently available radiation monitoring systems [1-3] provide the necessary information on the radiation state of the main and auxiliary equipment, enclosures, emissions of radioactive substances into air, water, radiation exposure of personnel, etc. However, in the future, such systems must encompass all possible perturbing factors and must not only provide information, but also in some cases control.

Systems for monitoring such enormous commercial objects as, for example, nuclear power plants, include geographical and biological, impact and regional monitoring in the presence of combined radiation, physical, and chemical perturbing factors, i.e., they on the one hand represent the most complex and important systems for providing monitoring information and, on the other, they are the most advanced (developed) systems that lay the path for developing other similar monitoring systems.

Aside from expanding the functions and increasing the amount of monitoring and control, further development of such systems is directed toward increasing the measuring capabilities, since measurement of physical parameters is the primary function of these systems. The accuracy of measurements can be increased by decreasing the influence of external background and the background accumulating at the monitoring points, eliminating systematic error, and including automatic compensation of the nonlinearity of the detectors.

The economic factors in creating and using such systems are an important aspect. The cost of the systems is in many ways determined by the cost of replacement parts, communication lines, assembly, and startup operations. The operational cost is determined by the cost of maintaining constant parameters of the system by the service personnel, the number and quality of personnel, and their errors.

Increasing the requirements for reliability, accuracy of measurements, especially in real-time, and fast response, expanding the functions together with the economic factors determine the requirements and criteria for constructing modern systems, choosing the structure, elements, and composition of the main and peripheral installations and the organization of their communication.

The development of computer technology and the advent of accessible, inexpensive microprocessers and microcomputers permit new solutions to these problems and may permit taking the next qualitative step in creating and improving radiation monitoring systems in nuclear power plants. The success in solving the monitoring problems is in many ways determined by the state of knowledge about the object, the choice of an appropriate information and measuring model with optimum monitoring capacity for the given object.

*This paper is based on a report at the 2nd Conference of Member-Countries of the Council on Mutual Economic Aid on Radiation Safety of Nuclear Power Plants, Vilnius, May 18-21, 1982.

Translated from Atomnaya Énergiya, Vol. 53, No. 3, pp. 131-138, September, 1982.

0038-531X/82/5303-0577$07.50 © 1983 Plenum Publishing Corporation

Declassified and Approved For Release 2013/03/04 : CIA-RDP10-02196R000300010003-8

Declassified and Approved For Release 2013/03/04 : CIA-RDP10-02196R000300010003-8

The pragmatic side of constructing modern systems is the development of a complete, basic set of functional installations, which permit creating in a planned manner an object-oriented system with optimum functional capacity, control points, equipment for maintaining operation, i.e., making it possible for the planners of radiation safety monitoring complexes to account for the characteristics of the object without considerable additional expenditures.

In this paper, we examine the problems of constructing modern systems for monitoring radiation in nuclear power plants. We emphasize the problem of operational radiation monitoring and we demonstrate, using this problem as an example, the possibilities of microprocessors and microcomputers and distribution of functions over subsystem levels.

Radiation Monitoring System Structure. The structure of the system for monitoring radiation in a nuclear power plant is based on realization of two basic planning principles: separating in the overall problem the most independent parts and introducing a hierarchy of ordered levels for solving it. Both principles are effectively satisfied in the radiation monitoring system: first, due to the possibility of solving the overall problem in the form of a parallel construction of the entire set of weakly coupled (from the point of view of the interaction dynamics) problems: radiation monitoring of enclosures and equipment in the power block; radioecological monitoring of adjacent territories; monitoring pass-through and exit paths; individual dosimetric monitoring of nuclear power plant personnel; and, second, the specific nature of each problem is reflected in the choice of the optimum number and organization of levels in its solution.

Figure 1 shows the structure of the complex of radiation monitoring apparatus in the form of a three-level, hierarchial system for a two-block nuclear power plant with a water-cooled water-moderated power reactor.

The use of standard computer equipment in the system (microcomputers and microprocessors) permits automating most of the routine work in the operation of the complex and leads to a more flexible interaction of the operator (dosimetrist) with the system due to the use of a dialogue mode instead of functional keyboards. The program realization of the system functions decreases the range of technical equipment and improves its adaptation to the characteristic of the object. The use of standard peripheral equipment at operator stations permits broad standardization of the methods for recording and displaying the state of the object and permits using standard forms of report documentation. Each problem is realized on a separate subsystem of the technical equipment, and the high-frequency dynamics of the object are localized in them. The interaction of subsystems at the upper level of the system represents its low-frequency component.

We shall examine the structure of the subsystems for solving the problems enumerated above.

Radiation and radioecological monitoring is characterized by a large number of monitoring points (300-500) distributed over enclosures and the territory encompassed by the power plant, continuity and efficiency, and requirements for minimum delays in transformation [1, 2]. The choice of structure for a subsystem with two processing levels is determined by the economic saving due to the reduction of cable lengths, which is achieved by placing the processing equipment closer to the monitoring points. The lower level of the subsystems consists of stations for collecting data, containing the primary transducers including the detection blocks, weather sensors, flowrate meters, as well as systems for local alarms and control, radially connected to the base modules. At this level, the parameters being monitored are measured and calculated in real-time, the control actions are drawn up, the working order of the equipment is checked, and data is formed for transmitting to the upper level of the subsystems.

The base modules form a distributed computed system, in which several loops and modules, cascade-connected by communication lines in series with an interface, according to GOSTu 23765—79, are separated. Each loop begins and terminates in the executive module, the loop control. In contrast to the structure in [4], the use of an executive module in the loop permits organizing horizontally independent groups of computers (for example, for solving subproblems involving monitoring of protective shields in the first and second loops or in the auxiliary equipment), radially connected by lines from a series interface to the upper level of the subsystem. One loop can encompass 100 monitoring points. The survivability of data collecting stations with a breakdown in the communication lines to the series-connected interface is ensured by retaining the measurement, alarm, and control functions of the base modules and the possibility for controlling the operational modes of the module through its built-in digital display.

Declassified and Approved For Release 2013/03/04 : CIA-RDP10-02196R000300010003-8

Declassified and Approved For Release 2013/03/04 : CIA-RDP10-02196R000300010003-8

The operational control and display functions, introduction of operational records and transmission of data to upper levels of the system for centralized display of the monitoring processes and introduction of the main radiation monitoring system records are executed in the upper level of the subsystems. Radioecological monitoring of the adjacent territory includes group analysis and accumulation of data from measurements of soil, water, and other samples, which the operator introduces at the second level of the subsystem from results of laboratory measurements.

Monitoring of the pass-through and exit paths for contamination of hands, body, clothing, and transport is characterized by short permissible computing time and high reliability of the decisions adopted. The subsystem contains one level of technical equipment, whose high capacity is achieved by local concentration of computers. The link to the upper level of the system is established when necessary by centralized recording to contamination events.

The subsystem for individual dosimetric monitoring of nuclear power plant personnel consists of two processing levels. Data collected from the ionization and thermoluminescence dosimeters, as well as information on the content of radionuclides in the body are collected and preliminarily processed and the personnel are identified. The results of measurements are processed at the upper level, where an intermediate data file is formed, which is then sent to the upper level of the system into a data bank for individual dosimetric monitoring of nuclear power plant personnel. Operational information on random (in time) queries, for example, in the case of regulation or repair and preventive work, as well as a periodic listing of the exposure of the nuclear power plant personnel to external and internal irradiation, are displayed by the display systems in the upper subsystem level. The data band contains information on each worker: the γ, β, and neutron irradiation doses over a ten-day period, the current month and year, over the time of work in the nuclear power plant, and from the beginning of professional work together with an indication of the last name, name, the department, section, specialty indication, and classification number.

Centralized radiation monitoring systems permit concentrating at the operator or dosimetrist total information on monitoring processes and radiation conditions at the plant [3]. However, increased attention to the radiation safety of nuclear power plants has increased the number of monitoring channels up to 200-300 for each block in the nuclear power plant and approximately to 500 in the two-block plant. Information is given to the operator in the form of signals showing an increase above the warning and accident thresholds and reports on the working order of the channels, translating them into the verification regime and other auxiliary regimes (in all there are about 1500-2500 positional signals), as well as in the form of results of measurements for each channel. Receiving this quantity of information and adopting operational solutions for normalizing the radiation state at the nuclear power plant leads to appreciable psychological pressure on the operator and operator fatigue. The general problem of man–machine dialogue requires finding an optimal solution for the problem of representing incoming information in a convenient and compact form with preliminary selection by importance and management efficiency.

Possibilities have recently been discussed for comprehensive representation of the diverse information on radiation conditions at the nuclear power plant using colored CRT displays [4]. The information content of reports is increased and the time required by the operator, who is responsible for the safe operation of the nuclear power plant, for analyzing events and making decisions is decreased by the colored displays in separate channels automatically changing in accordance with the program loaded into the microcomputer.

We can consider the application of a single colored display with variable display format or simultaneously two and even three display formats, for example, for a two-block power plant, etc. In order that the operator can rapidly comprehend and evaluate the background or the changing radiation conditions, it is first necessary to display the presence or absence of alarm signals (accident, warning, or malfunction signals), using for this purpose contrasting colors and positioning of symbols convenient for perception.

The format shown in Fig. 2 consists of 300 rectangles, grouped either according to channel number, for the channels used at the power plant (variant I or II), or according to the connection to some base module (variant III). For normal conditions at the nuclear power plant, all rectangles are green. When the first threshold has been exceeded in some channel, the color changes to a blinking yellow color and when the second threshold is exceeded to a blinking red color. In order to make the work of the operator easier, these channels are

Declassified and Approved For Release 2013/03/04 : CIA-RDP10-02196R000300010003-8

Declassified and Approved For Release 2013/03/04 : CIA-RDP10-02196R000300010003-8

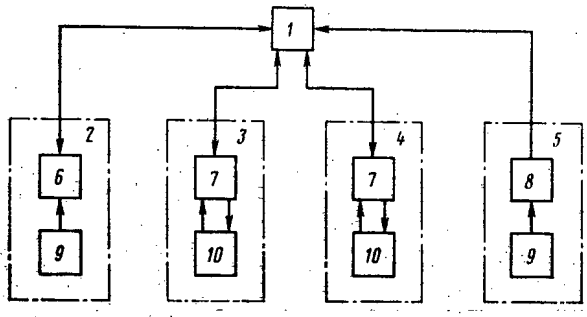

Fig. 1. Structure of the complex for monitoring radiation safety at a nuclear power plant: 1) central console of the radiation monitoring system; 2, 3, 4) subsystem for individual dosimetric, radioecological, and radiation monitoring, respectively; 5) subsystem for monitoring contamination; 6) dosimetrist's console; 7) operating console; 8) contamination monitoring units; 9) primary processing units; 10) data collection stations.

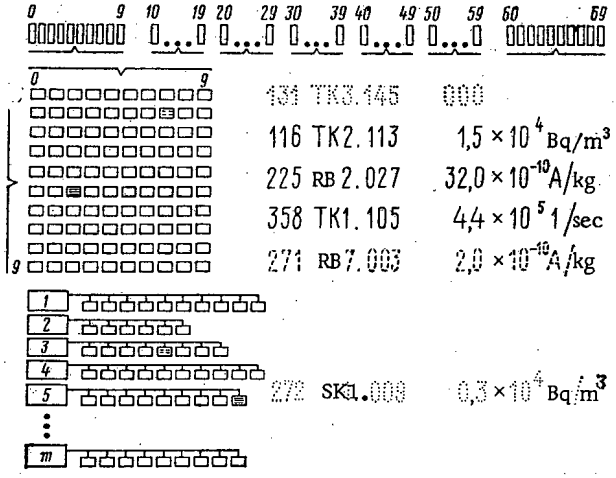

Fig. 2. Format of states: ...) blue; ——) red; ---) yellow.

automatically displayed on the screen for continuous measurements with the appropriate color. In so doing, the alphanumerical label of the channel, used for the given power plant within the scope of a unified automated control system, as well as the physical dimensionality of the parameter measured is indicated. The operator can put the indication manually into a continuously lit state, so as to make it possible to evaluate rapidly the change in the conditions in other channels (according to the blinking display). If a threshold has been exceeded in some channel and then the monitored quantity has returned to the norm, then the corresponding rectangle is transformed into a green triangle (the fact that the threshold has been exceeded in this channel is remembered). When a malfunction is discovered in the channel, the color of the rectangle changes to blue, and while the channel is switched-off for the time period required to make a check, the rectangle has a light-blue color. Priority in the representation of information is given to the blue color, and then light-blue, red, and yellow. At the same time, the operator can query the measurements in any other channel, which will be displayed by a green color. This format must be constantly present for efficient evaluation of the overall situation at the power plant.

In addition to the format presented above, it is also useful to have a second format in the form of a group analog histogram (Fig. 3), which indicates the current values of the

Declassified and Approved For Release 2013/03/04 : CIA-RDP10-02196R000300010003-8

Declassified and Approved For Release 2013/03/04 : CIA-RDP10-02196R000300010003-8

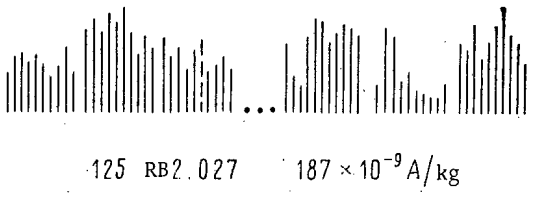

Fig. 3. Format of the group histogram on a black and white display.

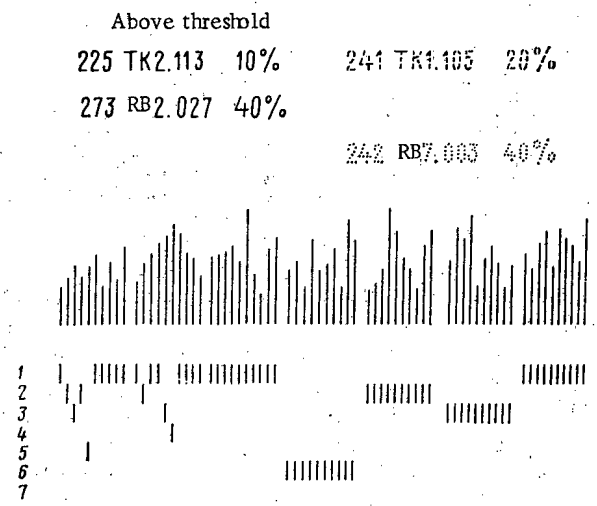

Fig. 4. Group histogram format on color display.

level of measured parameters in a chosen group of channels in the form of vertical lines. The number of channels in such a group is limited by the resolution of the CRT and is usually about 100 for black and white displays [5]. For more efficient evaluation of information in channels where the first or second thresholds have been exceeded, the corresponding channel is transformed into the blinking line mode and can be represented in digital form on the same screen.

The colored display increases the information content of such a format. Here, it is possible either to increase the number of channels in a group to 250, changing at the same time the color of the lines from green to yellow and red (when thresholds in separate channels are exceeded), or to remain in the 100 channel format (using different colors) while introducing different information.

Figure 4 shows the format used in monitoring radioactive inert gases, for which each detection block is used for measurements in several enclosures by means of remote switching of air ducts. In addition to the colored histogram, a picture is shown on the format indicating the open valve and the number of the enclosure from which the gas being monitored is entering. If the threshold has been exceeded in some channel, then the number of this channel and the value of the excess above the threshold level in percent, calculated using the equation

$$\frac{A_{meas} - A_{thres}}{A_{thres}} \cdot 100,$$

where A_{meas} is the current value of parameter being monitored and A_{thres} is the threshold setting, are displayed automatically on the screen in an appropriate color.

The operator can also call up manually on the same format the reserve up to the threshold level, defined according to the equation

$$\frac{A_{thres} - A_{meas}}{A_{thres}} \cdot 100,$$

Declassified and Approved For Release 2013/03/04 : CIA-RDP10-02196R000300010003-8

Declassified and Approved For Release 2013/03/04 : CIA-RDP10-02196R000300010003-8

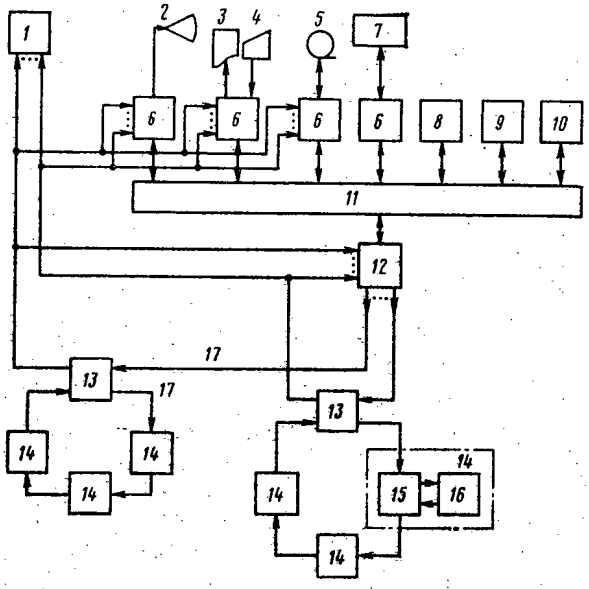

Fig. 5. Structure of the subsystem for monitoring radiation in the power block: 1, 2) digital and operational display, respectively; 3) printout of group data; 4) control panel; 5) data library storage; 6) input-output control; 7) central console for the radiation monitoring system; 8) central processor; 9, 10) operational and permanent system memory, respectively; 11) common bus; 12) input-output control for the sequential interface; 13) control module with microprocessor; 14) data collecting station; 15) base module with microprocessor; 16) detection blocks, alarms, control units; 17) sequential interface.

if the threshold has not been exceeded in this channel.

All of these formats and colored displays greatly improve the operation of the man-machine link. However, in order to maintain high reliability of the monitoring, it is useful to provide the traditional simple and reliable general alarm systems (indicating that the first or second threshold has been exceeded or a malfunction has occurred), signals from which can also be used to switch-on automatically the formats of the color displays above.

Subsystem Monitoring Radiation in the Power Block. All processing and preliminary information functions are transferred to the lower level of the system, while operational display, recording, and collecting data concerning the state of the object, and communication with the operator and the upper level of the complex are performed in the upper level. Figure 5 shows the organization of the upper subsystem level (operating station) based on the common bus of the Élektronika-60 microcomputer. The subsystem is constantly in the main state, in which sequential scanning of all monitored points and automatic output of information in analog form on a CRT (operational) display screen for all monitored points of the operator-chosen loop (channels, in which the threshold has been exceeded, are distinguished by color and blinking display), as well as in digital form for channels in which the threshold has been exceeded, and selectively for any monitored point in both displays, occur. The monitored parameters are periodically listed in red for those channels where a threshold has been exceeded and the procedure for introducing the operational records and processing queries from the upper level of the complex is performed automatically.

The operator interacts with the subsystem, forming with the help of a keyboard in the control panel over several steps of the dialogue on the CRT display screen a query for operational or recorded information in the form of charts, graphs, and tables, grouped according to the indicators of the monitored parameters, giving the type, logical and boundary conditions for data output. All control actions by the operator are recorded on the printer.

Declassified and Approved For Release 2013/03/04 : CIA-RDP10-02196R000300010003-8

Declassified and Approved For Release 2013/03/04 : CIA-RDP10-02196R000300010003-8

Let us examine the interaction of the components, levels of control, and organization of the given subsystems.

The lowest level of the subsystem contains up to five loops of the base modules. The loops operate in parallel and each of them is connected at the upper level of the subsystem to a digital display, controllers of the input-output operational display, printer, accumulator of record data on a magnetic tape, controller of input-output of the sequential interface, and is closed in the executive module of the loop. In the basic state (throughout scanning), the loop control functions are transferred to the upper level of the subsystem in the executive modules, which sequentially increment the number of the loop channels and translate the records of the channels on the output device in the upper level. The procedures for servicing the queries for data output from the operational records are performed at the upper subsystem level, independent of the lower subsystem level.

Queries for output of required operational information (for example, printing the technological monitoring channels, where a threshold has been exceeded) generate a sequence of control commands for the loops in the base modules. Each of them can be represented as a processor, which performs the current job, while the executive module acts as an interpreter of the commands from the upper level. It obtains commands from the controller of the sequential interface and executes them on the processor (loop). When the current command has been performed on the processor, the executive module returns control upwards outputting the results of performing the command, entering into the output devices of the upper level. In this state, the process of sorting and merging of channel records occurs in each loop and between loops. In the base modules, its records are selected according to qualifying indications (for example, according to type of parameter monitored), sorted according to a fixed sort key, and if the given relations between the trace transmitted through the interface and the upper record formed in the selection module are satisfied, they are outputted into the sequential interface of the loop. Analogous interaction processes occur between the executive modules of the loops. The termination of the regime is indicated by complete rotation of the same record through the loop.

The information collected, computed, and sorted by the subsystem forms the data base for operational radiation monitoring and on a logical level is represented in the form of files of actual data from the lower level and operational record data. The records contain data on each monitored point: its identifying number, type of monitored parameter, value, scale coefficient, two threshold settings, and state indication (passage through a threshold, equipment malfunction).

Structure of Base Module. The required productivity of the lower level of the radiation monitoring subsystem is achieved by separating it into a set of base modules. Each of them contains a complete collection of functions, transferred to the level, and is related to neighboring modules only by the transfer function.

The structure of the base module shown in Fig. 6 reflects two aspects of its operation: functions and logic. The functions form the external characteristic of the module, and most of them vary with the specific planning of the subsystem. Their designation depends on the types of connected detection blocks and stored processing algorithms. The logic of a module is reflected in the organization of the coupling of its components (structure). The multilevel structure of a module separates its permanent and variable functions. The permanent functions are the measuring and control procedures. Their realization is organized on separate microprocessor sections and is fixed in the permanent microprogrammed memory. The variable functions are separated into semipermanent, which are changed during the operation of the module, and fixed for a given module (but not necessarily the same for neighboring modules). These functions are realized on the upper level of a module (its central microprocessor) and differ according to the storing procedures, viz., in permanent, semipermanent, or operational memory.

The measuring procedures are fixed in the permanent microprogrammed memory of the multichannel average frequency meter (MAFM), realized on the microprocessor sections. The MAFM has up to 32 independent galvanically decoupled frequency inputs, in each of which the input frequency can vary over a range covering four orders of magnitude from 0.5 to $5 \cdot 10^3$ pulses per second. The model presented in [6] is chosen as one of the basic algorithms for realizing the MAFM program. The procedure for measuring in each channel is described by the following recurrence expression:

Declassified and Approved For Release 2013/03/04 : CIA-RDP10-02196R000300010003-8

Declassified and Approved For Release 2013/03/04 : CIA-RDP10-02196R000300010003-8

$$Y(mT) = \frac{X(mT)}{\tau} + Y[(m-1)T]\exp(-T/\tau), \quad (1)$$

where mT are the discrete time intervals fixed by the timer; m = 0, 1, 2, ...; X(mT), number of pulses from the detecting block over the interval mT; τ measuring time constant; Y[(m − 1)T], value of the average frequency calculated up to the time mT and stored as a result of the measurements; Y(mT), new value of the average frequency calculated at time mT.

Expression (1) describes the digital equivalent of the integrating RC circuit, which when measuring randomly distributed pulses gives a statistical error calculated from the equation

$$\delta = 1/\sqrt{2n\tau}, \quad (2)$$

where n is the average frequency of the pulses.

The condition for optimum measurements in the system operating in real time can be taken as

$$n\tau = \text{const}, \quad (3)$$

which ensures constant accuracy of the measurements over the entire range and minimum delay in the measurements. The operands in MAFM are represented in a floating point binary system, which permits measurements over a wide range with the required accuracy. The format of the fractional part is determined by the dynamic range of the input frequency and constitutes 16 binary digits and the integer part constitutes 8 binary digits.

The process of making measurements in each channel consists of periodic multiplication of the information accumulated in the channel by a coefficient, less than 1, and adding the result to that contained in the input buffer of the given channel, after which the buffer is tripped and accumulates the next portion of input pulses, while the final result is stored up to the next processing cycle. The quantization period is fixed by a timer with a quartz resonator; T and the capacity of the input buffer Bi are related by the relation

$$n_{i\max} T/I < B_i, \quad (4)$$

where $n_{i_{max}}$ is the upper limit of the average frequency with respect to the i-th channel; I is the number of channels.

Equation (1), including relation (3) and the floating point binary representation of operands, describes the measuring algorithm of the channel

$$Y(mT) = M_x 2^{c1} + 2^p M_{y-1} - 2^p M_{y-1} 2^{c2-p}, \quad (5)$$

where M_x is the number of input pulses accumulated in the buffer over the interval mT; C1, constant coefficient equal to the binary logarithm of the fraction BT/c; $2^p M_{y-1}$, binary representation of the result of the preceding measurement; c2, constant coefficient equal to the binary logarithm of Tτ.

Thus, for T and τ which are multiples of 2^k, where the modulus k is an integer, the multiplication is performed by a rapid series of shifts followed by subtraction. The number of cycles of shifts depends on the integer part of the operand of the result. For addition, the first operand in Eq. (5) is shifted by a constant number of digits and it is not necessary to adjust the orders.

When the measuring procedure is completed, the MAFM switches to comparing the result with fixed threshold levels, multiplies it by a scale factor, which takes into account the sensitivity of the detector and its dead time constant τ_d, as well as the scale of the monitored parameter, and transforms the final result into a binary-decimal number system. Next, the output record of the channel is formed and is sent into the output buffer of the MAFM. The next timer signal triggers an analogous measuring and processing process in the next channel.

Declassified and Approved For Release 2013/03/04 : CIA-RDP10-02196R000300010003-8

Declassified and Approved For Release 2013/03/04 : CIA-RDP10-02196R000300010003-8

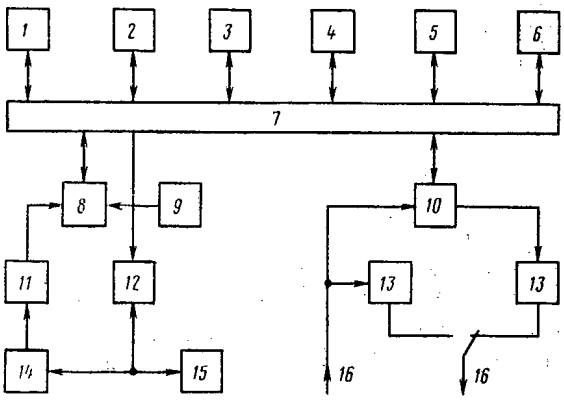

Fig. 6. Structure of the base module: 1) digital display; 2) central microprocessor; 3, 4, 5) operational, semipermanent, and permanent memory, respectively; 6) exchange buffer; 7) common bus; 8) multichannel average frequency meter; 9) timer; 10) input–output control unit; 11) input buffers; 12) output switches; 13) main amplifier; 14) detection blocks; 15) alarms and executive units; 16) sequential interface.

The computing and control procedures are performed on the central microprocessor of the module. Its specific actions depend on the current operational state of the module. Nevertheless, there is a permanent part of the functions, determined by the configuration of the module, composition and type of primary transducers connected to it, alarms, and executive systems. These include subtraction of the external background for the difference blocks for detecting and accumulating background at the monitoring points, calculating the ratios for monitoring leakage, calculations of the rate of growth of activity while working on a stopped strip of the aerosol sensors, identifying the malfunctioning detection blocks, outputting requested information on the local digital display, control of local alarms and executive systems for threshold penetration signals. The remaining procedures of the central microprocessor are performed by operator commands, given from the upper level of the subsystem or from the keyboard of the local digital display. The control procedures switch the reference sources built into the detection blocks on and off, as well as the detection blocks, and change the scale factors and the threshold settings in the channels. The computational procedures include creating and eliminating virtual (program-generated) channels. The measuring information generated in the module of the virtual channel is the value of the function, whose arguments consist of the data from the real channels of the module. The attributes of the trace of the virtual channel, the transformation function, the time of its creation and annihilation are set by the operator.

The input–output control unit of the base module participates in each transmission session of the sequential interface of the loop and its action in the established mode consists either of outputting on the interface the output trace of the channel, receiving commands from the control module, or retransmitting the current message.

The control unit interacts with the central microprocessor through the common separating resource, namely, the exchange buffer, into which it periodically retransmits the actual records of the measuring channels. In the scanning mode, the collection of traces in the buffer is sorted according to the identifying number of the channel, while in the output mode of the input channels, according to the key indicator.

The connection of the controller with the lines from the sequential interface of the loop has a galvanic decoupler. In order to ensure operation, two paraphase main amplifier blocks are situated on a twisted pair of telephone wires, up to a kilometer long, in the module. When the main of reserve coupling lines malfunction, the module switches into an automatic operating mode retaining the alarm and control functions. When the blocks in the base module break down, they are manually switched out of the sequential interface line, while the transmitted messages are retranslated by the second block of main amplifiers.

Declassified and Approved For Release 2013/03/04 : CIA-RDP10-02196R000300010003-8

Declassified and Approved For Release 2013/03/04 : CIA-RDP10-02196R000300010003-8

Thus, the creation of a system for monitoring radiation in a nuclear power plant is related to the overall program for development of nuclear power. The required radiation monitoring capacity can be effectively ensured by staged growth of the apparatus using systems with a distributed structure. The application of microcomputers and microprocessors increases the flexibility of the system, its adaptability to the properties of the object, ensures convenient coupling with the human operator, increases the intelligence level of its important link, namely, the lower level processing systems (data collection stations). The sequential transmission channel at the lower level greatly decreases the cable routes. The multilevel structure permits clearly separating and organizing the levels for solving the problem: primary processing, cumulation of measurements, display, and coupling with the operator. Introducing data records from dosimetric and radiation monitoring in the power plant ensures efficient operation of the system and automatic composition of the record documentation, including forecasting and timely identification of possible events.

LITERATURE CITED

1. V. S. Zhernov et al., in: Proc. IAEA Symp. on Nuclear Power Plant Control and Instrumentation, IAEA, Vienna (1978), Vol. 2, p. 161.
2. V. S. Zhernov et al., Proceedings of the Symposium of Specialists in Member Countries of the Council of Mutual Economic Assistance (USSR, Dubna, 1975), Moscow (1976), p. 5.
3. V. S. Zhernov et al., Problems of Atomic Science and Technology, Series on Nuclear Instrumentation Construction [in Russian], Atomizdat, Moscow (1977), No. 34-35, Vol. 1, p. 40.
4. D. Union, D. Holloway, and A. Hyde, IEEE Trans. on Nuclear Science, NS-24, No. 1, 771 (1977).
5. V. S. Zhernov et al., At. Energ., 20, No. 1, 82 (1966).
6. B. Soucek, Minicomputers in Data Processing and Simulation, Wiley-Interscience (1972).

Declassified and Approved For Release 2013/03/04 : CIA-RDP10-02196R000300010003-8

Declassified and Approved For Release 2013/03/04 : CIA-RDP10-02196R000300010003-8

MONITORING THE DISTRIBUTION OF RADIONUCLIDES THROUGHOUT THE TECHNOLOGICAL CIRCUITS OF A NUCLEAR POWER STATION*

V. L. Antonov, A. A. Gruzdeva,
V. S. Zhernov, S. K. Kozlov,
O. B. Lapshev, V. V. Matveev,
V. V. Pushkin, M. K. Romanichev,
A. E. Shermakov, E. P. Vargin,
and L. P. Drozdova

UDC 621.039.58

In recent years, the demands on the operating safety of nuclear power stations and the protection of the environment have been increased. Because of this, in modern radiation safety monitoring systems an important role is being assigned to the prediction of a possible deterioration of the radiation environment as a result of a breakdown of the normal functioning of the plant fulfilling the role of safety barriers in the path of the spread of radioactive substances.

For nuclear power stations with water-cooled-water-modulated power reactors (VVÉR), the most probable entry of radioactive substances into the outside medium is a result of breakdown of the turbogenerator hermetic sealing. Because of the large degree of branching of the pipeline system of the primary circuit and the considerable velocity of motion of the coolant through U-shaped pipes, considerable stresses are created at the sites of their bends, which leads to vibration, the formation and growth of microcracks at the bends, and the pipeline welds. Therefore, the probability of a small leakage of coolant from the primary to the secondary circuit has always been assumed. Usually it is equal to 20-50 grams/h, but may reach 2 and even 50 kg/h [1]. As a result of the rupture of one of the U-shaped pipelines, the leakage may amount to 10^5 kg/h.

The radionuclides contained in the coolant of the primary circuit, on entering the water of the secondary circuit, accumulate and attain an equilibrium concentration over 7-9 h. The time of attaining equilibrium concentration is determined by the flow rate of the water entering through the continuous purging line in the special water purification system, and by the half-life of the radionuclides. Gaseous and volatile radionuclides enter the steam pipelines of the secondary circuit, collect in the turbine condensers and then are ejected into the atmosphere through the ejectors [2]. Thus, by locating the radioactive radiation detector equipment in the steam generator purging line and the exhaust of the ejectors, an event of coolant leakage from the primary into the secondary circuit can be recorded. Additional detector equipment installed alongside the main live steam pipelines will allow loss of hermetic sealing of the steam generator to be recognized (Fig. 1).

The sensitivity of the monitoring equipment to leakage, measured in kg/h, depends on the radioactivity of the coolant of the primary circuit, determined first of all by the number and degree of depressurization of the fuel elements and the reactor power. In order to assess the leakage in units of the mass flow rate, it is necessary to know the radioactivity of the coolant at the instant of breakdown of hermetic sealing of the steam generators. A knowledge of the activity by volume of the gaseous fission products, determining the radioactivity of the live steam and the steam–air mixture at the ejector exhausts, is the most important, and also the activity by volume of the isotopes of iodine, from which the radioactivity of the steam generator purging water can be judged.

In the composition of the radiation safety monitoring apparatus, there are devices for detecting the volume activity of ^{132}I and ^{88}Kr in the primary circuit coolant. The informa-

*Journal version of a report at the Second Conference of the CMEA Member Countries, "Assurance of Radiation Safety in Connection with the Operation of Nuclear Power Stations" [in Russian], (Vil'nyus, May 18-21, 1982).

Translated from Atomnaya Énergiya, Vol. 53, No. 3, pp. 138-143, September, 1982.

0038-531X/82/5303-0587$07.50 © 1983 Plenum Publishing Corporation

Declassified and Approved For Release 2013/03/04 : CIA-RDP10-02196R000300010003-8

Declassified and Approved For Release 2013/03/04 : CIA-RDP10-02196R000300010003-8

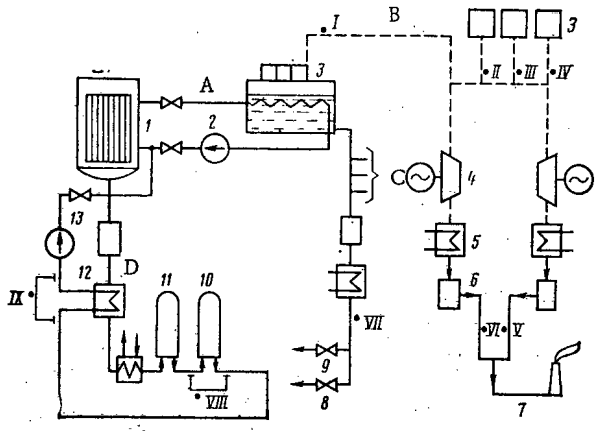

Fig. 1. Location of steam generator leakage monitoring points: 1) reactor; 2) main circulatory pump; 3) steam generator; 4) turbine; 5) condenser; 6) main ejectors; 7) ejector exhaust; 8) into the overflow tanks; 9) to water purification; 10, 11) anion and cation exchange filter, respectively; 12) heat exchanger; 13) expander; A — coolant of primary circuit; B — live steam of secondary circuit; C, D — steam generator and primary circuit purging line, respectively; I-IX — monitoring points.

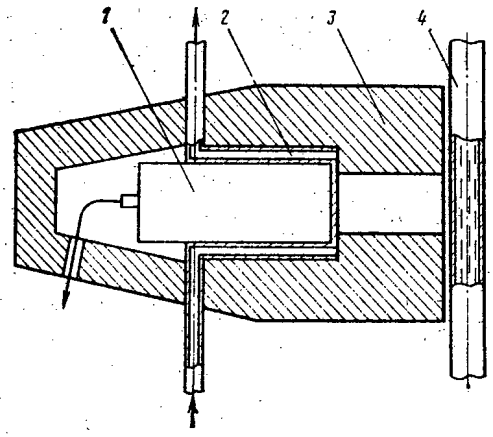

Fig. 2. Device for the detection of ^{88}Kr activity: 1) detector unit; 2) cooler; 3) shielding; 4) bypass line.

tion from these instruments, in addition, allows the state of the reactor core activity to be followed, and also the dynamics of the development of depressurization of the fuel element cans and the radiation safety at the nuclear power station.

Detection Devices for the Technological Monitoring of the Activity of the Primary Circuit. The volume activity of ^{88}Kr in the primary circuit coolant is measured by using a detection device (Fig. 2) consisting of a γ-quanta scintillation detector unit with a crystal of NaI(Tl) with a diameter of 63 × 63 mm, a lead shield, and a collimator, installed in the bypass line through which part of the coolant passes after the cation- and anion-exchange filters of the water purification system (see Fig. 1, VIII). This inclusion system allows the background from the γ-emission of the radionuclides to be reduced, found in the coolant in the form of cations and anions. A cooler built into the shielding provdes stable operating conditions for the equipment.

Electrical pulses from the detector unit are amplified and are fed to two differential discriminators. One of them is tuned to a γ-emission energy of 2.4 MeV and the other records

Declassified and Approved For Release 2013/03/04 : CIA-RDP10-02196R000300010003-8

Declassified and Approved For Release 2013/03/04 : CIA-RDP10-02196R000300010003-8

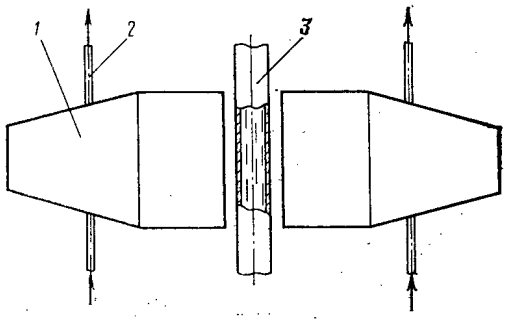

Fig. 3. Device for detecting the activity of ^{132}I: 1) detector unit shield; 2) coding water feeder pipe; 3) bypass line.

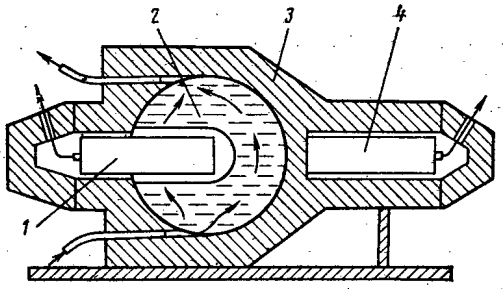

Fig. 4. Detector device for the total γ-activity of the liquid: 1) main detector unit; 2) measurement cell; 3) shielding; 4) detector compensation unit.

the γ-radiation of a higher energy. Thus, the background from external γ-radiation and the high-energy γ-radiation of the radionuclides located in the coolant, is partially compensated. The sensitivity of the equipment is $8 \cdot 10^{-10}$ pulses·m^3/sec·Bq, and the recording range is $5 \cdot 10^8$-$5 \cdot 10^{11}$ Bq/m^3 ($\sim 10^{-5}$-10^{-2} Ci/liter).

The volume activity of ^{132}I is measured by the cascade γ-emission, using the device shown in Fig. 3. The scintillation detector units are positioned on different sides of the bypass pipeline, sampling the coolant after passing through the cation-exchange filter of the water purification system (see Fig. 1, IX). As a result of this sampling scheme, the background is reduced, caused by the radionuclides which are located in the coolant in the form of cations. The electrical pulses from each of the detector units are fed to two differential discriminators. One of the pair of discriminators from different measurement channels is tuned to the cascade radiation energy of ^{132}I. After the discriminators, the pulses are fed to a coincidence circuit. The second of the pair, with the coincidence circuit, records the γ-radiation of higher energy, which makes it possible to partially reduce the background from the cascade radiation of the nuclides located in the coolant. In order to reduce the integrated loading of the detector units and the background of random coincidences, the devices have a lead shield. Stable operating conditions are ensured by coolers built into the shield. The recording range is $4 \cdot 10^8$-$4 \cdot 10^{11}$ Bq/m^3 (10^{-5}-10^{-2} Ci/liter). The recording range is divided into two subranges, with a sensitivity of $8 \cdot 10^{-6}$ and $2.2 \cdot 10^{-6}$ pulses·m^3/sec·Bq, respectively.

Detector Device for Monitoring the Hermetic Sealing of the Steam Generators. The total volume γ-activity of the water in the common steam generator purging collector (see Fig. 1, VII) is monitored by a device (Fig. 4) consisting of two scintillation detector units with NaI(Tl) crystals with a diameter of 63 × 63 mm. One of them, the main one, is located in a spherical sampling cell. The second is installed nearby, behind a lead insert, and serves to compensate the extraneous γ-background. The detector units and the measurement cell are surrounded by a lead shield with a thickness of 60 mm. The sensitivity of the device is 0.8 pulses/sec at $4 \cdot 10^3$ Bq/m^3 and the energy range is 0.1-3 MeV. The recording range is $3.7 \cdot 10^4$-$3.7 \cdot 10^7$ Bq/m^3 (10^{-9}-10^{-6} Ci/liter).

Declassified and Approved For Release 2013/03/04 : CIA-RDP10-02196R000300010003-8

Declassified and Approved For Release 2013/03/04 : CIA-RDP10-02196R000300010003-8

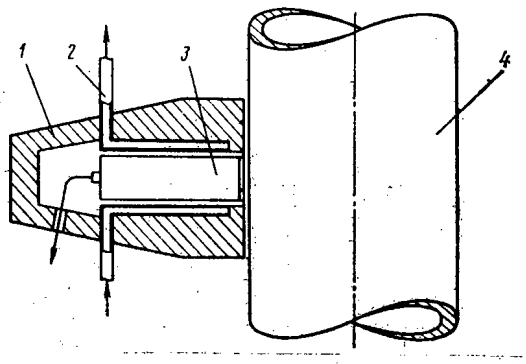

Fig. 5. Live steam activity detector device: 1) shield; 2) cooler; 3) detector unit; 4) secondary circuit steam pipeline.

The activity of the live steam in the main steam pipes of the secondary circuit (see Fig. 1, I-IV) is monitored with a scintillation detector unit with a NaI(Tl) crystal with a diameter of 63 × 63 mm, recording γ-quanta of energy 0.1-3 MeV. In order to shield the detector unit from the extraneous γ-background, it is surrounded from the sides by a lead shield with a thickness of 60 mm, as shown in Fig. 5. The sensitivity of the device is $8.8 \cdot 10^{-5}$ and 10^{-4} pulses·m³/sec·Bq for the steam pipelines of the secondary circuit of the VVÉR-440 and VVÉR-1000, respectively. The recording range is $5 \cdot 10^4$-$5 \cdot 10^7$ Bq/m³ ($1.3 \cdot 10^{-9}$ to $1.3 \cdot 10^{-6}$ Ci/liter).

The activity of the steam–gas mixture at the exhaust of the main ejectors (see Fig. 1, V-VI) is determined by the high-energy β-emission of the radioactive gases. In order to record them, a detector device with two high-temperature gas-discharge counters SBM-18 is installed inside the pipeline with the steam–gas mixture. The main counter is surrounded with a thin sheath of polyamide for shielding from the effect of moisture, and the compensation counter is installed in a steel casing with a thickness of 4 mm. The construction of the detector device and the scheme for its installation in the steam pipeline are shown in Fig. 6. The sensitivity is $1.6 \cdot 10^{-8}$ pulses·m³/sec·Bq when standardized on ^{85}Kr. The recording range is $3.7 \cdot 10^5$-$3.7 \cdot 10^8$ Bq/m³ (10^{-8}-10^{-5} Ci/liter).

In order to estimate the coolant leakage from the primary circuit, which can be recorded by the detector devices described, we shall calculate the volume activity of the medium at the monitoring points I-VII in Fig. 1.

Determination of the Volume Activity of the Secondary Circuit and the Lower Limits of Its Measurement in the Case of Leakage of the Steam Generator. The primary circuit coolant containing radioactive products of fission, corrosion and activation, in the case of breakdown of the hermetic sealing of the steam generator, together with the purging water and the steam, is conveyed along the communicating pipes of the secondary cicuit (Fig. 7). The readings of the monitoring devices, with constant values of the activity of the primary circuit coolant and the parameters of the secondary circuit, are proportional to the leakage of the steam generator.

The sensitivity of the equipment to leakage can be estimated from the data of the radionuclide activity calculation at the monitoring points of the VVÉR-440 and VVÉR-1000, with secondary circuit parameters which are characteristic for them, the coefficient of removal, and also the radionuclide composition of the primary circuit coolant [2-4]. We shall calculate the volume activity of individual radionuclides at the monitoring points for values which are characteristic in the first months of operation of the reactor, when the activity of certain radionuclides of the noble gases and of the iodine isotopes is close to $4 \cdot 10^5$ Bq/liter (10^{-5} Ci/liter). In the case of depressurization of the steam generator, nongaseous radionuclides are accumulated in the reactor water, as the radioactive noble gases escape directly from it into the steam. The buildup of activity of the nongaseous radionuclides in the reactor water can be calculated from the following system of equations:

$$\frac{da_{dp}(t)}{dt} = q_0 + \frac{K^r}{P}\beta_{sg}a_p(t) - \left[(1-K^r)\beta_{wp} + \frac{P-1}{P}K^r\beta_{sg} + \lambda\right]a_{dp}(t) \qquad (1)$$

Declassified and Approved For Release 2013/03/04 : CIA-RDP10-02196R000300010003-8

Declassified and Approved For Release 2013/03/04 : CIA-RDP10-02196R000300010003-8

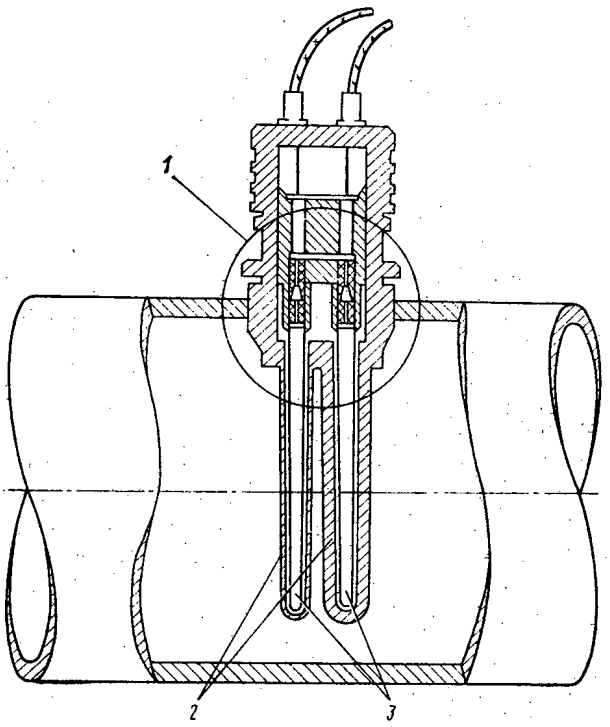

Fig. 6. Steam–gas mixture activity detector device:
1) setting in the steam pipeline; 2) shielding filter;
3) high-temperature counter.

$$\frac{da_{dp}(t)}{dt} = \frac{K^r}{P}\beta_{sg}a_{dp}(t) - \left[(1-K^r)\beta_{wp} + \frac{P-1}{P}K^r\beta_{sg} + \lambda\right]a_p(t), \quad (1)$$

where $a_{dp}(t)$ and $a_p(t)$ are the activity of the radionuclides accumulated in the reactor water of the depressurized (dp) and pressurized (p) steam generators respectively; q_o is the activity entering the depressurized steam generator from the primary circuit, and determined by the formula

$$q_0 = A_I Q_I / \rho_w^I,$$

where A_I is the volume activity of an individual radionuclide in the primary circuit coolant, Bq/m^3; Q_I, leakage of the primary circuit coolant into the steam generator; and ρ_w^I, density of the water in the primary circuit, t/m^3.

β_{sg} is the water exchange coefficient of the steam generator through the turbine condenser, which is found by the formula

$$\beta_{sg} = G_{sg}/\rho_w^{II} V_{sg},$$

where G_{sg} is the live steam flow rate in the main steam generator, t/h; ρ_w^{II} and V_{sg} are the density (t/m^3) and volume of reactor water in the steam generator (m^3);

β_{wp} is the water exchange coefficient through purging of the steam generator, calculated by the formula

$$\beta_{wp} = G_{wp}/\rho_w^{II} V_{sg},$$

where G_{wp} is the flow rate of the reactor water to purging the steam generator, t/h;

λ is the decay constant of the radionuclide, and K^r is the coefficient of removal of radionuclides from the steam, relative units.

Declassified and Approved For Release 2013/03/04 : CIA-RDP10-02196R000300010003-8

Declassified and Approved For Release 2013/03/04 : CIA-RDP10-02196R000300010003-8

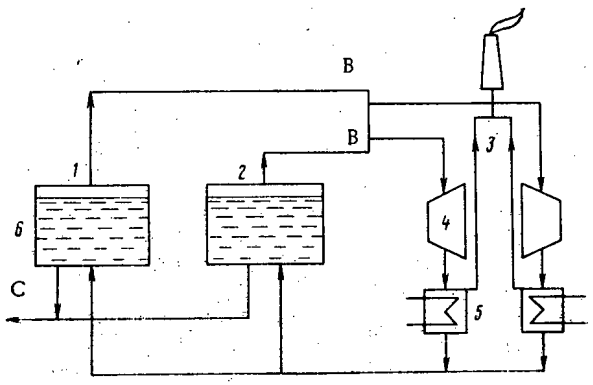

Fig. 7. Distribution of radionuclides contained in the coolant of the primary circuit, through the communicating pipelines of the secondary circuit: 1, 2) steam generators; 3) ejector exhausts; 4) turbine; 5) turbine condenser; 6) leakage of coolant into the reactor water of the steam generator. B — Live steam of secondary circuit; C — steam generator purging line.

In order to shorten further notation, we introduce the following symbols:

$$\alpha = (K^{r}/P)\,\beta_{sg};$$
$$\beta = (1-K^{r})\,\beta_{wp} + \frac{P-1}{P}K^{r}\beta_{sg} + \lambda,$$

where P is the number of steam generators. The volume activity of the nongaseous radionuclides over the time t can be found from expression (1)

$$\left.\begin{aligned} A^{dp}_{sg}(t) &= \frac{a_{dp}(t)}{V_{dp}} = A^{dp}_{sg}K_{dp}(t) \\ A^{p}_{sg}(t) &= \frac{a_{p}(t)}{V_{dp}} = A^{p}_{sg}K_{p}(t), \end{aligned}\right\} \qquad (2)$$

where A^{dp}_{sg} and A^{p}_{sg} are the equilibrium volume activity in the reactor water of the depressurized and pressurized steam generators respectively, in expanded form representing the following expressions:

$$\left.\begin{aligned} A^{dp}_{sg} &= \frac{q_0}{V_{sg}}\,\frac{\beta}{\beta^2-\alpha^2} \\ A^{p}_{sg} &= \frac{q_0}{V_{sg}}\,\frac{\alpha}{\beta^2-\alpha^2}, \end{aligned}\right\} \qquad (3)$$

where $K_{dp}(t)$ and $K_{p}(t)$ are time terms, characterizing the buildup of radionuclides which attain equilibrium value, equal to 1, when t tends to infinity and in expanded form are expressed as:

$$\left.\begin{aligned} K_{dp}(t) &= 1 - \frac{\beta^2-\alpha^2}{2\beta}\left[\frac{e^{-(\beta-\alpha)t}}{\beta-\alpha} + \frac{e^{-(\beta+\alpha)t}}{\beta+\alpha}\right] \\ K_{p}(t) &= 1 - \frac{\beta^2-\alpha^2}{2\alpha}\left[\frac{e^{-(\beta-\alpha)t}}{\beta-\alpha} - \frac{e^{-(\beta+\alpha)t}}{\beta+\alpha}\right]. \end{aligned}\right\} \qquad (4)$$

The ratio of the activity of a nongaseous radionuclide in the depressurized and pressurized steam generators is called the discrimination ratio. In this case it has the form

$$A^{dp}_{sg}/A^{p}_{sg} = \beta/\alpha = P\left[1 + \frac{(1-K^{r})\,\beta_{sg}+\lambda}{K^{r}\beta_{sg}} - \frac{1}{P}\right]. \qquad (5)$$

Declassified and Approved For Release 2013/03/04 : CIA-RDP10-02196R000300010003-8

Declassified and Approved For Release 2013/03/04 : CIA-RDP10-02196R000300010003-8

From the known volume activity in the reactor water, the volume activity in the water of the common steam generator purging collector can be determined:

$$A_{wp}(t)=\frac{A_{sg}^{dp}K_{dp}(t)+(P-1)A_{sg}^{p}K_{p}(t)}{P}(1-K^{r}), \tag{6}$$

which, over approximately 8 h from the start of the leakage is close to the equilibrium value

$$A_{wp}=\frac{A_{sg}^{dp}(1-K^{r})}{P}\left[1+(P-1)\frac{\alpha}{\beta}\right]. \tag{7}$$

The volume activity of individual nongaseous radionuclides in the live steam of the second circuit can be described by the equations

$$\left.\begin{aligned}A_{steam}^{dp}(t)&=\frac{A_{sg}^{dp}(t)K^{r}\rho_{s}}{\rho_{w}^{II}},\\ A_{steam}^{p}(t)&=\frac{A_{sg}^{p}(t)K^{r}\rho_{s}}{\rho_{w}^{II}},\end{aligned}\right\} \tag{8}$$

where ρ_s is the density of the live steam, t/m³. The equilibrium volume activity will be equal to

$$\left.\begin{aligned}A_{steam}^{dp}&=\frac{q_{0}K^{r}\rho_{s}}{\rho_{w}^{II}V_{sg}}\frac{\beta}{\beta^{2}-\alpha^{2}}\\ A_{steam}^{p}&=\frac{q_{0}K^{r}\rho_{s}}{\rho_{w}^{II}V_{sg}}\frac{\alpha}{\beta^{2}-\alpha^{2}}\end{aligned}\right\} \tag{9}$$

respectively. Because the radioactive noble gases almost immediately and completely escape from the reactor water of the depressurized steam generator into the steam, their volume activity in the case of constant leakage of coolant rapidly attains the equilibrium value, determined from the expression

$$A_{steam}^{dp}=q_{0}\rho_{s}/G_{sg}. \tag{10}$$

Separation of the radioactive noble gases, which enter the atmosphere through the ejectors and the effluent stack, from nonvolatile and slightly volatile radionuclides passing into the condensate and returned to the steam generators, takes place in the turbine condenser. The volume activity of the individual radioanuclides in the atmosphere at the ejector exhaust, can be determined by the formula

$$A_{ej}=q_{0}\rho_{ej}/2G_{ej}, \tag{11}$$

where ρ_{ej} is the density of the atmosphere at the ejector exhaust, t/m³; G_{ej} is the flow rate of steam at the ejector outlet, t/h. The figure 2 in the denominator takes account of the redistribution of the steam from the depressurized steam generator between the two turbines.

The calculations, performed by formulas (2)-(11) on the assumption of a constant value of the coolant leakage and nominal flow rates of the medium, allow certain conclusions to be drawn.

The volume activity of the steam generator purging water, determined by the detector devices at the monitoring point VII, is 70-80% due to iodine isotopes. The minimum recorded leakage of the primary circuit coolant, for the initial state of the reactor core, amounts of 0.5-1 kg/h. Its value was determined, starting from the minimum intensity (rate) of counting of the instruments, which for the expected level of the extraneous background of γ-radiation at the site of their installation, and for the primary circuit coolant activity assumed

Declassified and Approved For Release 2013/03/04 : CIA-RDP10-02196R000300010003-8

Declassified and Approved For Release 2013/03/04 : CIA-RDP10-02196R000300010003-8

in the calculation, can be reliably identified as the induced activity of the medium, and not statistical fluctuations of the extraneous γ-radiation background. The minimum counting intensity (rate) at points VII, I-IV and VIII, and IX amounts to 5, 2.5, and 0.5 pulses/sec, respectively.

The volume activity of the live steam of the depressurized steam generator is 15-30% due to the radioactive noble gases, 55-70% due to nitrogen isotopes, and 3-5% due to iodine isotopes. It increases rapidly during the few minutes from the start of the leakage because of the radioactive noble gases and ^{16}N, then during 8 h it still increases slightly, in consequence of iodine isotopes and other slightly volatile radionuclides entering the steam. The minimum recorded activity of the live steam amounts to 30-40 kg/h.

The readings of the detector instruments, measuring the volume activity of the live steam of the pressurized steam generators, will be a factor of 10-20 less than the readings of the similar instrument monitoring this parameter of the depressurized steam generator. The activity of the live steam of the pressurized steam generators, due to the nongaseous radionuclides which enter the reactor water through the makeup system, slowly increases up to the equilibrium value during approximately 8 h from the start of the leak.

The readings of the detector instruments installed at the ejector exhausts, are determined by the activity of the noble gases. The minimum recorded leakage is equal to 5-15 kg/h.

Estimates of the minimum detectable leakage which can be recorded, were carried out for the initial state of the core. In proportion with the increase of the volume activity of the primary circuit coolant during operation of the reactor, their sensitivity to leakages increases, and may be a factor of 3-5 better than was mentioned earlier.

As already mentioned, the volume activity of the medium at the monitoring point VII is determined mainly by isotopes of iodine, and at points I-VI by the radioactive noble gases. At the same time, it is proportional to the scaled volume activity of these groups of isotopes in the primary circuit coolant at the leakage value. Therefore, in order to estimate the leakage, the readings of the detector instruments at the monitoring points VII and I-IV, it will be necessary to normalize on the readings at the monitoring points VIII and IX respectively, where the volume activity of ^{132}I and ^{88}Kr is determined. A more accurate estimate can be obtained, if the detector instruments measuring the volume activity of the live steam at points I-IV, are tuned to recording ^{88}Kr with respect to the energy of the γ-quanta of 2.4 MeV. The information entering from the detector devices at the monitoring points VII and V, and VI allows depressurization of the steam generator to be revealed in the early stages, when the leakage is small. At the same time, it does not give information as to precisely which steam generator has developed the leak. The failed generator is determined from the readings of the detector devices at monitoring points I-IV but, as already mentioned, these devices are less sensitive. In consequence of this, two cases of localization of the depressurized steam generator are possible.

The detector devices at monitoring points VII, V, and VI have registered a leakage of a steam generator, but it is so small that it is at the sensitivity threshold at monitoring points I-IV. In this case, the servicing personnel have sufficient time to sample the reactor water from each steam generator and to determine in laboratory conditions in which of them the total activity has increased, to assess the degree of failure of the steam generator, and to take the necessary measures.

A large leakage, which can create an emergency situation or which can cause a dangerous radiation environment at the nuclear power station, is determined from the readings of the detector devices measuring the volume activity of the live steam at points I-IV. In this case, the failed steam generator can be localized within 100-200 sec from the start of the leakage.

Further ways for improving the monitoring equipment are possible because of:

a) increase of the operating stability and sensitivity of the detection equipment, measuring the volume activity of the live steam at point I-IV, which allows a leakage at earlier stages to be detected. By tuning the discrimination thresholds to record such datum radionuclides as ^{88}Kr and ^{16}N, it becomes possible to estimate the leakage directly in kg/h;

b) locating the detector devices determining the volume activity of the purging water, directly in the purging line of each steam generator, as these devices have quite a high

Declassified and Approved For Release 2013/03/04 : CIA-RDP10-02196R000300010003-8

Declassified and Approved For Release 2013/03/04 : CIA-RDP10-02196R000300010003-8

sensitivity, and will allow the failed steam generator to be located in the case of a leakage of 0.5-1 kg/h.

The method of monitoring a steam generator leakage by measuring the volume activity of the live steam condensate, sampled from the main steam pipelines, in our opinion is less promising by comparison with determining the volume activity of the water in the steam generator purging lines. This is because the coefficient of removal of nongaseous radionuclides from the steam $K^r \ll 1$ and, consequently, the volume activity of the live steam condensate is many times less than the volume activity of the water in the purging lines.

The authors express their thanks to L. M. Luzanova for useful discussion of the results of the present paper, advice, and valuable comments.

LITERATURE CITED

1. L. M. Voronin et al., At. Energ., 41, 4, 235 (1976).
2. É. Gladki et al., Yad. Energ., 22, 11, 412 (1976).
3. T. Kh. Margulova, Nuclear Power Stations [in Russian], Vysshaya Shkola, Moscow (1969).
4. V. L. Antonov et al., Scientific-Technical Conference of the CMEA Member-Countries on "Monitoring and Control of Reactors and Nuclear Power Stations [in Russian], Warsaw, Vol. 3 (1974).

Declassified and Approved For Release 2013/03/04 : CIA-RDP10-02196R000300010003-8

Declassified and Approved For Release 2013/03/04 : CIA-RDP10-02196R000300010003-8

DISTRIBUTION OF THE FLUX DENSITY AND HARDNESS OF THE NEUTRON SPECTRUM WITH HEIGHT AND OVER THE CROSS SECTION OF THE HEAT-GENERATING ASSEMBLIES OF VVÉR-365 AND VVÉR-440 REACTORS

B. A. Bibichev, V. P. Maiorov,
V. D. Sidorenko, and P. I. Fedotov

UDC 621.039.512.45

One can measure the flux density and spectrum of the neutrons in the active zones of VVÉR-365 and VVÉR-440 reactors (water-cooled-water-modulated power reactors) only in special channels located in the central tubes of the heat-generating assemblies (HGA) [1]. One can measure the distribution of the flux density and spectrum of the neutrons with the HGA height with the help of activation detectors in these channels. Experimental data on the distribution of these quantities over the HGA cross section are also necessary for checking and correcting the computational programs. One can obtain such information from the concentration of certain fission products in the fuel after the HGA are unloaded from the reactor.

Those fission products are most favorable for these purposes whose accumulation depends differently on the thermal neutron flux and hardness of the neutron spectrum and whose concentration one can measure by the γ-spectrometric method without destroying the fuel elements [2, 3]. The method of γ-spectrometry of fission products has been used previously [4] to measure the depletion and isotopic composition of uranium and plutonium in samples of the fuel elements from VVÉR-365 and VVÉR-440 reactors. This same method is employed in this paper to measure the distribution of the flux density of thermal neutrons Φ_{th} and the hardness of the neutron spectrum γ with respect to the cross section and height of several HGA of these reactors.

The value of γ is determined by the relationship [5] $\gamma = \Sigma_{th}^{a}/\xi\Sigma^{s}$, where Σ_{th}^{a} is the total macroscopic cross section of a cell of the active zone and $\xi\Sigma^{s}$ is the moderating power of the medium. In this case one can write the effective fission, capture, or absorption cross section for a given nuclide in the form $\hat{\sigma} = \sigma_{th} + \gamma I$, where σ_{th} is the cross section for neutrons of the thermal group and I is the resonance integral.

The method for measuring of Φ_{th} and γ is based on the significantly different dependence of the accumulation of ^{137}Cs and ^{134}Cs in the fuel on γ and Φ_{th}. The ^{137}Cs concentration depends weakly on γ and is proportional to $\Phi_{th}t$ in the first approximation, and the ^{134}Cs concentration is proportional to $\gamma(\Phi_{th}t)^2$ [4], where t is the irradiation time of the HGA. The sequence for the calculation of γ and Φ_{th} from the measured values of the concentration of these nuclides is shown in Fig. 1. It is evident from Fig. 1 that γ and Φ_{th} are calculated by fitting the calculated values of the ^{134}Cs and ^{137}Cs concentrations to the measured values. The calculated concentrations N_{134} and N_{137} are found from the solution of the system of depletion equations for the isotopes of uranium, plutonium, and their fragment nuclides. The depletion equations are solved by numerical integration in the two-group approximation for the neutron spectrum with an irradiation time step of 1 day. The fission of ^{238}U and the variation of γ and Φ_{th} as a function of the variation of the concentration of fissile nuclides [6] is taken into account in the calculations.

Data on the initial enrichment of the fuel, the irradiation time, and the specific power of the fuel in the investigated HGA are used in calculating γ and Φ_{th}. The specific power of the fuel in the last irradiation cycle is corrected on the basis of the measured concentration of ^{106}Ru [7].

One should note that the values of γ and Φ_{th} obtained in this way depend on the choice of the effective thermal cross sections and the resonance integrals of the capture and fission of heavy and fragment nuclides. The choice of the resonance integral of neutron capture for ^{133}Cs (I_c^{133}) has the most important meaning for the calculation of γ, since the partial over-

Translated from Atomnaya Énergiya, Vol. 53, No. 3, pp. 143-147, September, 1982. Original article submitted August 17, 1981.

 0038-531X/82/5303-0596$07.50 © 1983 Plenum Publishing Corporation

Declassified and Approved For Release 2013/03/04 : CIA-RDP10-02196R000300010003-8

Declassified and Approved For Release 2013/03/04 : CIA-RDP10-02196R000300010003-8

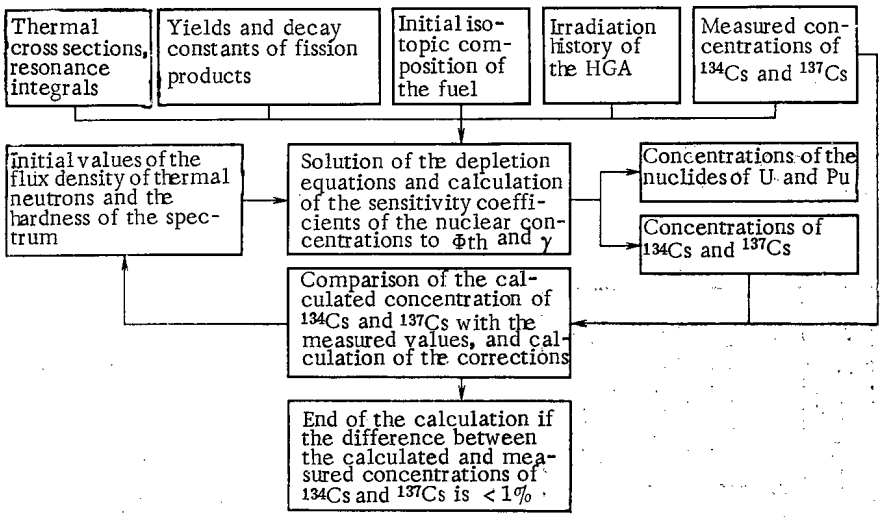

Fig. 1. Sequence for the calculation of γ and Φ_{th} from the measured concentrations of ^{134}Cs and ^{137}Cs.

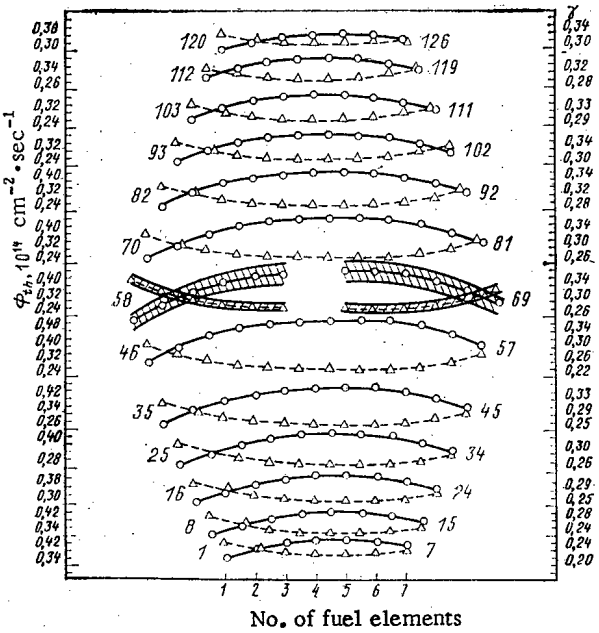

Fig. 2. Distributions of γ and Φ_{th} over the cross section of HGA R-3.6 No. 213 at a distance of 87.5 cm from the bottom of the active zone: Δ) Φ_{th}, ○) γ; the hatched regions denote the errors in the experimental values of γ and Φ_{th}.

lapping of the principal resonances of the (n, γ)-reaction by ^{133}Cs and ^{238}U and the decrease of the neutron flux density at the energy of the principal resonances of ^{133}Cs due to the capture of resonant neutrons by ^{238}U lead to a blocking of I_c^{133}.

The values of the thermal cross sections and resonance integrals for the uranium and plutonium isotopes used in this paper were taken from calculations by the POP program [8]. The thermal cross sections (σ_f^{235}, σ_c^{235}, σ_c^{239}, σ_c^{241}) and I_c^{133}, which are most important to the calculation of the isotopic composition of the fuel, have been corrected on the basis of the measurement results for the concentration of nuclides of heavy elements and fission products in the fuel for various depletions. The concentrations of ^{106}Ru, ^{134}Cs, ^{137}Cs, $^{235,236,238}U$, and $^{239,240,241,242}Pu$ have been measured for this reason with a 1-2% error by destructive

Declassified and Approved For Release 2013/03/04 : CIA-RDP10-02196R000300010003-8

TABLE 1. Basic Operational Data of the Investigated HGA

HGA No.	Initial enrichment in ^{235}U, %	Reactor	Number of irradiation cycles	Average depletion, kg/ton U	$\bar{\gamma}_{exp}$	$\bar{\gamma}_{POP}$	Φ_{th}, 10^{14} cm^{-2} · sec^{-1}
DR-3 No. 80	3	VVER-365, Unit II	1	11,9±0,5	0,262±0,018	0,226	0,332±0,017
RP-3 No. 223	3	"	3	26,7±1,0	0,246±0,027	0,220	0,272±0,022
OI-3M-5 No. 12	3	"	3	33,1±1,3	0,220±0,024	0,220	0,397±0,032
RI-2.4 No. 03	2,4	"	4	36,1±1,4	0,186±0,020	0,198	0,398±0,032
RP-3.3 No. 71A	3,3	VVER-440 Unit III	1	16,0±0,6	0,248±0,017	0,235	0,367±0,018
R-3,6 No. 213	3,6	VVER-440, Unit IV	3	31,1±1,0	0,306±0,034	0,254	0,236±0,019
R-3,6 No. 216	3,6	"	3	32,9±1,1	0,321±0,035	0,254	0,251±0,020

TABLE 2. Errors of the Experimental Values of the Concentrations of ^{137}Cs, ^{134}Cs, and ^{106}Ru and the Values of γ and Φ_{th} at a Given Point along the Height of a Fuel Element and of an HGA, %

Measurement error	Meas. of object	$\frac{\Delta N_{137}}{N_{137}}$	$\frac{\Delta N_{134}}{N_{134}}$	$\frac{\Delta N_{106}}{N_{106}}$	$\frac{\Delta\gamma}{\gamma}$	$\frac{\Delta\Phi_{th}}{\Phi_{th}}$
Random component of the total error	Fuel element	1,1	1,1	2,1	8,4	5,1
	HGA	0,5	0,5	0,9	3,8	2,3
Total error	Fuel element	2,8	3,1	3,8	13,6	9,3
	HGA	2,6	2,9	3,7	11,3	8,0

Declassified and Approved For Release 2013/03/04 : CIA-RDP10-02196R000300010003-8

Declassified and Approved For Release 2013/03/04 : CIA-RDP10-02196R000300010003-8

Declassified and Approved For Release 2013/03/04 : CIA-RDP10-02196R000300010003-8

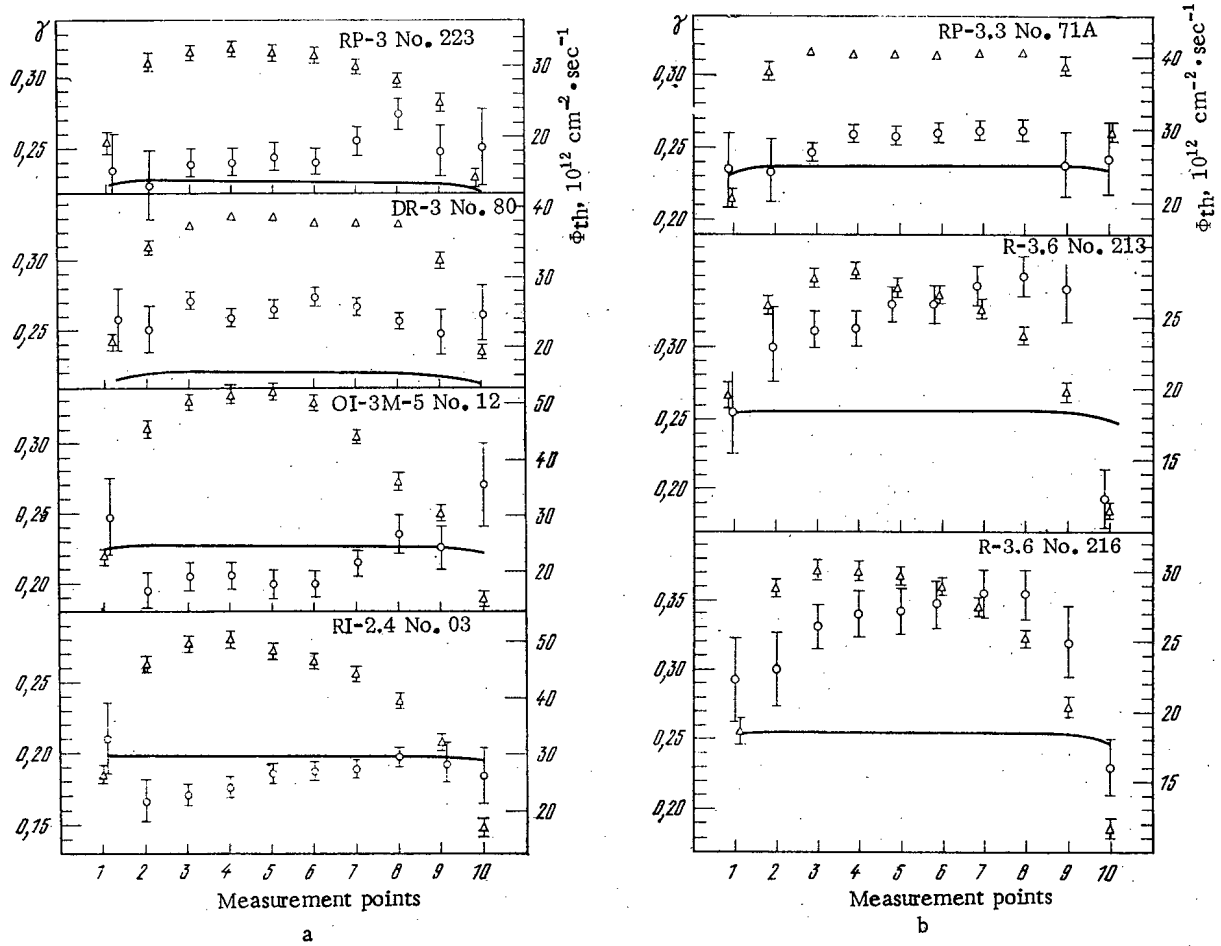

Fig. 3. Distributions of γ and Φ_{th} with height for (a) four VVÉR-365 HGA and (b) three VVÉR-440 HGA: ———) calculation of γ by the POP program; Δ) Φ_{th}; ○) γ.

methods in samples of the VVÉR-365 and VVÉR-440 fuel elements [9]. The correction method is based on minimization of the sum of the squares of the deviations between the calculated and experimental values of the concentrations of uranium, plutonium, and cesium isotopes in all the samples [10].

The set of effective cross sections obtained in this way was used to investigate the distribution of γ and Φ_{th} with height and over the cross section of four HGA of a VVÉR-365 reactor and three HGA of a VVÉR-440 reactor of the Novovoronezh nuclear power plant (Table 1). HGA DR-3 No. 80, RP-3 No. 223, RI-2.4 No. 03, and RP-3.3 No. 71A were not mounted on the edge of the active zone or next to the HGA for operational regulation of the reactor power in even a single irradiation cycle. HGA R-3.6 No. 213 and R-3.6 No. 216 were mounted on the edge of the active zone in the first irradiation cycle, and HGA OI-3M-5 No. 12 was located next to the HGA for operational regulation of the reactor power during all three runs.

The measurements were performed in the protective chamber of the Novovoronezh nuclear power plant. Prior to the measurements all the HGA were disassembled into individual fuel elements. A total of 24-26 fuel elements were investigated in each HGA comprised of 126 fuel elements. Several fuel elements were selected from each series for the measurements in order to obtain information on the distribution of the fission products with respect to the HGA cross section. The γ-spectra of the fission products were measured at ten points along the height of these fuel elements. The measurements were made every 25 cm along the height of the fuel elements, and the first measurement was made at a distance of 12.5 cm from the lower end of each fuel element (the bottom of the active zone). The spectra of all 126 fuel elements were measured in HGA R-3.6 No. 213 and R-3.6 No. 216 for a more detailed investigation of the distribution of fission products over the cross section of HGA located 87.5 cm away from the bottom of the active zone. The function $n_i(x, y) = a_{0i} + a_{1i}r + a_{2i}r^2 + a_{3i}x + a_{4i}y$, where n_i is the concentration of the i-th fission product in the fuel element with coordinates x, y and $r = \sqrt{x^2 + y^2}$ (the origin of coordinates coincides with the axis of the central tube of the HGA), has been used to approximate the distribution of the concentrations of ^{137}Cs,

Declassified and Approved For Release 2013/03/04 : CIA-RDP10-02196R000300010003-8

Declassified and Approved For Release 2013/03/04 : CIA-RDP10-02196R000300010003-8

^{134}Cs, and ^{106}Ru over HGA cross section and to calculate the average values of the concentrations of these nuclides. The coefficients $a_{0i}a_{1i}...a_{4i}$ were calculated by the method of least squares from the measured concentrations of the i-th nuclide in 24-26 fuel elements.

As an example, the errors in the measurement of the ^{137}Cs, ^{134}Cs, and ^{106}Ru concentrations at a given point along the height of a fuel element of HGA R-3.6 No. 213 and the average concentrations of these nuclides over the cross section of this HGA are given in Table 2. The sensitivity coefficient of γ and Φ_{th} to the concentrations of these nuclides in the fuel are used in calculating the errors of the experimental values of these quantities, which are also given in Table 2.

The distribution of γ and Φ_{th} over the cross section of HGA R-3.6 No. 213 at a distance of 87.5 cm from the bottom of the active zone are given in Fig. 2. Since γ and Φ_{th} vary in time in proportion to the depletion of the fuel, the average values of γ and Φ_{th} during the irradiation time of the HGA are given in Fig. 2. It is evident from Fig. 2 that the values of γ for the fuel elements of the outer series is approximately 1.5 times less than that for the fuel elements of the inner series, and the values of Φ_{th} are on the contrary larger than for the fuel elements of the outer series. This peculiarity of the distribution of γ and Φ_{th} over cross section is explained by the influence of the water gap of the HGA on the neutron spectrum in the fuel elements of the outer series.

The smallest values of γ, and consequently the largest values of Φ_{th}, are observed in fuel elements 1-7, 1-58, and 58-120. This is possibly associated with the fact that HGA R-3.6 No. 213 was mounted on the edge of the active zone in the first run and with these elements was turned towards the water reflector. The nonuniformity coefficients of the distribution of γ and Φ_{th} over the cross section of HGA R-3.6 No. 213 are 1.18 and 1.35, respectively. The difference between these coefficients indicates an appreciable nonuniformity in the distribution of epithermal neutrons over the cross section of HGA R-3.6 No. 213. Similar distributions of γ and Φ_{th} over cross section were observed for the remaining HGA. One can also note that a similar distribution of γ over HGA cross section is observed in the HGA of VVÉR-70 reactors [11].

The experimental values of γ and Φ_{th} at ten points along the HGA height and the calculated distributions of γ along HGA height, calculated with the help of the POP program for an asymptotic neutron spectrum, are given in Fig. 3. It is evident from Fig. 3 that the experimental values of γ vary significantly with height in HGA R-3.6 No. 213, R-3.6 No. 216, and OI-3M-5 No. 12, and that the calculated values of γ are almost constant for all the HGA.

The decrease of γ in the end sections of HGA R-3.6 No. 213 and R-3.6 No. 216 is explained by the influence of the water reflector on the neutron spectrum in these HGA. The increase of γ in the upper part of HGA OI-3M-5 No. 12 can be explained by the influence of the HGA for operational regulation of the reactor power on the neutron spectrum in this HGA (the fuel—absorber boundary of the HGA of the safety and control rods of the 12th group is located between the sixth and seventh measurement points). The leveling off of the distributions of γ with height for the remaining HGA is possibly associated with the use of depleted absorbers in the HGA of the reactors of the second and third units of the Novovoronezh nuclear power plant. The distributions of Φ_{th} with HGA height repeat the depletion distributions in these HGA.

It is also evident from Fig. 3 that a discrepancy between the calculated and experimental values of γ in absolute value is also observed for some HGA. The experimental average values of $\bar{\gamma}$ and $\bar{\Phi}_{th}$ in the HGA and the average calculated values of $\bar{\gamma}$ calculated by the POP program are given in Table 1. It is evident from Table 1 that the deviations between the experimental and calculated values of $\bar{\gamma}$ in HGA DR-3 No. 80, R-3.6 No. 213, and R-3.6 No. 216 exceed the errors in the experimental values of $\bar{\gamma}$. The largest deviation is observed for HGA R-3.6 No. 216, and it amounts to $\sim$30%.

Thus, the possibility has been shown in this paper of applying the method of γ-spectrometry of fission products to obtain information about the distribution of γ and Φ_{th} with height and over the cross section of the HGA of VVÉR reactors. Measurements of γ and Φ_{th} in the HGA of VVÉR-365 and VVÉR-440 reactors by this method have shown that the neutron spectrum can vary significantly over the cross section and height of HGA and that is is advisable to take these variations into account in calculations of the nuclide composition of spent fuel.

Declassified and Approved For Release 2013/03/04 : CIA-RDP10-02196R000300010003-8

Declassified and Approved For Release 2013/03/04 : CIA-RDP10-02196R000300010003-8

LITERATURE CITED

1. S. S. Lomakin, V. P. Petrov, and P. S. Samoilov, Radiometry of Neutrons by the Activation Method [in Russian], Atomizdat, Moscow (1975).
2. J. Krtil et al., in: Proc. IAEA Symp. on Analytical Methods in the Nuclear Fuel Cycle, Vienna (1972), p. 491.
3. O. Eder and M. Lammer, in: Proc. IAEA Symp. on Nuclear Data in Science and Technology, Vienna (1974), Vol. 1, p. 233.
4. B. A. Bibichev, et al., At. Energ., 48, No. 5, 294 (1980).
5. S. M. Feinberg et al., in: Transactions of the 2nd Geneva Conference, Lectures of Soviet Scientists [in Russian], Vol. 2, Atomizdat, Moscow (1959), p. 411.
6. T. S. Zaritskaya, A. K. Kruglov, and A. P. Rudik, At. Energ., 41, No. 5, 321 (1976).
7. K. Tasaka, Nucl. Technol., 29, No. 2, 239 (1976).
8. V. D. Sidorenko and E. D. Belyaeva, Preprint IAE-1171, Moscow (1966).
9. A. V. Stepanov et al., At. Energ., 49, No. 4, 225 (1980).
10. I. Luffin, Z. Szatmary, and I. Vanuxeem, J. Nucl. Energ., 26, No. 12, 627 (1972).
11. H. Mehner, Kernenergie, 22, No. 11, 382 (1979).

CONTROL OF THE NEUTRON DISTRIBUTION IN A REACTOR BY A LIQUID ABSORBER

P. T. Potapenko

UDC 621.039.515

The use of a liquid absorber of neutrons for control is one of the trends in the improvement of channel power reactors [1, 2]. Liquid regulation has been applied effectively on the reactors of Canadian nuclear power plants [3]. An extensive program of the application of a liquid absorber on an RBMK has been carried out by Soviet scientists [4, 5]. Liquid regulating units (RU) for the three-dimensional control of the neutron distribution are discussed in this article.

Technical Requirements for RU. It is advisable on the whole for effective utilization of reactor fuel to equalize the energy distribution and temperature of the materials limiting the power of the reactor [6]. To this end an absorber which compensates the operational reactivity reserve must be placed in the central part of the active zone, which is called the control zone [7, 8]. With such a placement of the absorber (Fig. 1a) the neutron distribution within the confines of the control zone is equalized. Based on a calculation, the height of the equalized zone for an RBMK is about 50% of the reactor height, and the nonuniformity coefficient of the neutron distribution with height $k_z = 1.1$. With the traditional arrangement of the RU rods adopted for RBMK (Fig. 1b) $k_z = 1.2$-1.3. The height of the equalized control zone is evaluated from the formula [6, 7]

$$h = H - \pi M / \sqrt{K' - 1}, \quad (1)$$

where

$$K' = K - \gamma \cdot 2.405^2 M^2 / R^2;$$

H and R are the effective height and radius of the reactor; M, migration length; K, neutron multiplication factor outside the control zone; and γ, correction coefficient ($\gamma \approx 0$ for large dimensions of the control zone, and $\gamma = 1$ in the absence of such a zone when the reactor has no reactivity reserve). The multiplication factor in the control zone should be compensated with the help of the RU under the optimal regime up to a value K = 1.

Translated from Atomnaya Énergiya, Vol. 53, No. 3, pp. 147-151, September, 1982. Original article submitted July 6, 1981.

0038-531X/82/5303-0601$07.50 © 1983 Plenum Publishing Corporation

Declassified and Approved For Release 2013/03/04 : CIA-RDP10-02196R000300010003-8

Declassified and Approved For Release 2013/03/04 : CIA-RDP10-02196R000300010003-8

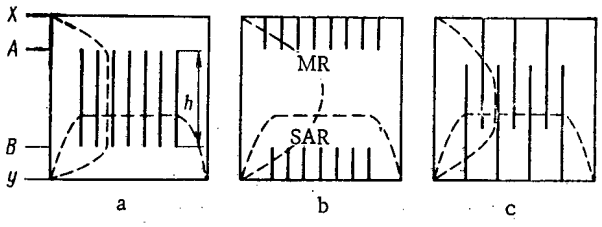

Fig. 1. Distribution of absorbers (——) and neutrons (---) in a diametrical cross section of the reactor: a) optimal placement; b) in operating high-powered water-cooled channel reactors (RBMK); and c) with "soft" control; X and Y are the boundaries of the active zone, and A and B are the boundaries of the control zone.

One can significantly equalize with safety control rods (SCR) the neutron distribution with height in the case of deep insertion of the rods into the active zone from above and below [for RBMK these are the manual regulation rods (MR) and the shortened absorber rods (SAR)]. However, such placement of the absorbers (see Fig. 1c) is not used due to a deterioration in the radial distribution of neutrons produced by deep insertion of the SCR rods. One can avoid this by the use of less effective soft RU, which with a nominal reactivity reserve would in practice fill all the existing SCR channels in the reactor.

The proposed liquid RU are alternative upper (MR) and lower (SAR) rods for RBMK. Therefore, besides optimal location in height, such RU should have acceptable dynamic properties. The dynamical characteristics of the neutron distribution of RBMK are characterized by a constant development time of the first azimuthal harmonic T_{01} of the order of 10 min [2].

Thus, one can formulate the following basic technical requirements on the regulating unit and a system of units.

1. In order to equalize the neutron distribution with height, the absorber should be concentrated in the central part of the reactor with respect to height — in the control zone.

2. The height of the absorber should be regulated upon a variation in the reactivity reserve.

3. In order to equalize the radial distribution of neutrons, the effectiveness of unit length of absorber should be three to four times less than the effectiveness of an emergency protection rod. (The requirement of "soft" control).

4. The density of the absorber in unit volume of the control zone should be regulated upon variation of the reactivity reserve so that K = 1. Upon satisfaction of the third requirement this can be achieved, for example, by varying the number of RU in unit volume of the control zone.

5. The RU system should provide independent control of the radial-azimuthal and height energy distributions.

6. The position of the RU with height should be regulated for control of the first harmonic of the height distribution of neutrons.

7. The time constant for variation of the RU length should be no longer than 2-3 min for operational stabilization of the neutron distribution, and no longer than 1 h (for suppression of perturbations associated with xenon poisoning) for a variation in its position with respect to height.

8. According to economic considerations, the RU absorber should be placed in those same channels as are the solid SCR.

The development of RU satisfying the listed requirements is a nontrivial problem and requires resourceful creativity. The best liquid absorber for channel reactors is water [2, 3]. The effectiveness of a column of water in the SCR channel of an RBMK is approximately one-third of the effectiveness of an MR rod [2].

Construction of the RU. Combination RU (Fig. 2) are proposed to satisfy the formulated requirements: a solid rod intended mainly for emergency protection is mounted in the SCR

Declassified and Approved For Release 2013/03/04 : CIA-RDP10-02196R000300010003-8

Declassified and Approved For Release 2013/03/04 : CIA-RDP10-02196R000300010003-8

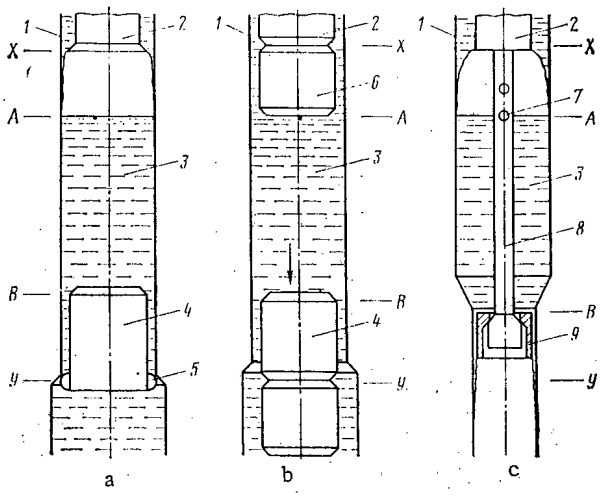

Fig. 2. Designs of liquid RU with (a) a lower expeller, (b) lower and upper expellers, and (c) a throttle on a rod: 1) channel, 2) rod, 3) water column, 4) lower expeller, 5) stroke limiter, 6) upper expeller, 7) aperture, 8) tubular rod, and 9) throttle.

channel in the upper part, and control of the reactor is accomplished with columns of water of variable height which are situated in the control zone. The water above and below the control zone is removed from the active zone by means of its expulsion by a gas void or expellers.

An RU with a floating lower expeller located in the lower part of the channel is presented in Fig. 2a [9]. Sections of the expeller are hollow. Their mass and dimensions are such that with a nominal flow of water through the channel (2-3 m^3/h) the expeller floats up in the channel to the detents (stroke limiter) and submerges at the maximum flow rate. The material of the expeller sections is an alloy of aluminum or zirconium. They are fabricated in the in the form of thin-walled tubes tightly welded at the ends. Water flows in a thin wetting film over the channel walls in the upper part of the channel above the level.

The water level in the channel, and this means the reactivity, is controlled in a given construction either by varying the hydraulic drag of the line carrying water out of the channel at a constant nominal flow rate with a valve or by varying the flow rate of water through the SCR channel at constant hydraulic drag of the loop by regulating it on top at the inlet.

An RU is presented in Fig. 2b [10] in which one can regulate the lower boundary of the water column by controlling the position of the floating expeller by varying the water flow rate. This is achieved by the fact that the channel is widened in the lower part. With a nominal water flow rate the expeller submerges if one places it in the upper part of the channel, and it floats up if it is located in the lower widened part of the channel. Thus, it occupies an intermediate average position which varies upon regulation of the flow rate. Due to the effective feedback on position by virtue of the widened section of the channel such a "suspended" state is stable. When the expeller moves, the lower boundary of the liquid absorber and the amount of it in the active zone changes, and this means the reactivity associated with control changes. In order to remove water from the upper part of the active zone, another upper expeller (see Fig. 2b) is attached to the end of the rod which can be shifted together with the rod. However, it is impossible in this case to use such an RU for emergency shutdown of the reactor, since when the rod is submerged in the initial section of its stroke some positive reactivity is introduced by virtue of the removal of water by the expeller at the boundary of the control zone.

It is advisable to use the regulating units presented in Figs. 2a and b for emergency protection and for manual regulation, respectively. Such RU provide for soft control of the radial and height energy distributions by replacing rods introduced from above and below (see Figs. 1b and c).

Declassified and Approved For Release 2013/03/04 : CIA-RDP10-02196R000300010003-8

Declassified and Approved For Release 2013/03/04 : CIA-RDP10-02196R000300010003-8

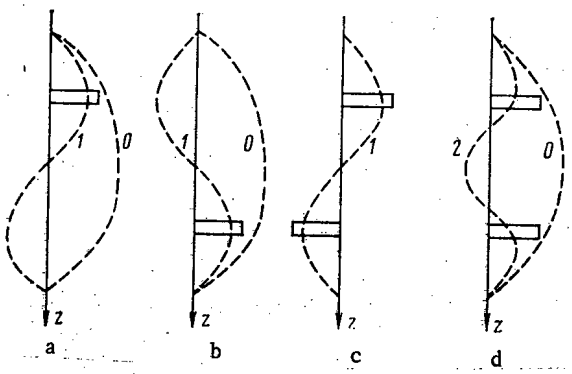

Fig. 3. Diagrams of the control actions of liquid RU upon a change in (a) the water level, (b) the position of the lower expeller, (c) upon displacement of the throttle and (d) a simultaneous change in the level: ——) diagram of the variation of the neutron multiplication factor; ---) excited harmonics: (0) fundamental, (1) first, and (2) second.

A design of an RU [11] in which a water column of the necessary height is contained by a throttle suspended on a tubular rod by the emergency protection rod is presented in Fig. 2c. The throttle forms an annular gap with the channel walls (the difference in diameters is about 1 mm), whose hydraulic drag is sufficient to form a water column with a height of 3-5 m water flows through the channel as rapidly as 3 m^3/h. The water flows in a thin wetting film above and below the water column outside the control zone. Gaseous cavities above and below the water column freely communicate with each other through the tubular rod and apertures. The lower apertures serve to fix and stabilize the maximum column height (∿5 m).

Variation of the reactivity and control of the radial energy distribution with the help of such RU is accomplished by varying the height of the water column and the flow rate. The height distribution of the energy is controlled by shifting the water column up or down with a servodrive rod. In the extreme upper position of the rod and throttle the channel is emptied, since the throttle enters into the wide part of the channel. The channel is cooled over its entire length by a wetting film.

Characteristics of the RU. The rate of change in the height h of the water column is (for the RU in Fig. 2c)

$$dh/dt = (Q - Q_1)/S, \tag{2}$$

where Q and Q_1 are the flow rates at the entrance and exit from the control zone, respectively, and S is the cross-sectional area of the water column. The flow regime of the water in the channel is turbulent; therefore,

$$h = \xi Q_1^2, \tag{3}$$

where ξ is the throttling coefficient. Thus the dynamical equation for the water column is

$$dh/dt = \left(Q - \sqrt{h/\xi}\right) S. \tag{4}$$

The level-flow rate static calibration characteristic is the parabola (3), since in the static situation $Q = Q_1$.

In the case of a step-by-step variation of the flow rate from Q_0 to Q_2, Eq. (4) has an analytic solution in implicit form:

$$t = \frac{2S\sqrt{h_2}}{Q_2}\left[\sqrt{h_0} - \sqrt{h(t)} + \sqrt{h_2}\ln\frac{\sqrt{h_0} - \sqrt{h_2}}{\sqrt{h(t)} - \sqrt{h_2}}\right]. \tag{5}$$

Declassified and Approved For Release 2013/03/04 : CIA-RDP10-02196R000300010003-8

Declassified and Approved For Release 2013/03/04 : CIA-RDP10-02196R000300010003-8

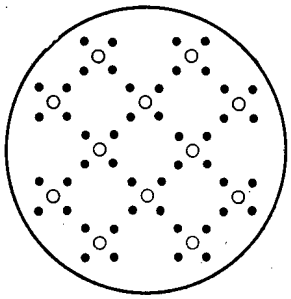

Fig. 4. Arrangement of the detectors (○) and liquid RU (●) in the regulation system.

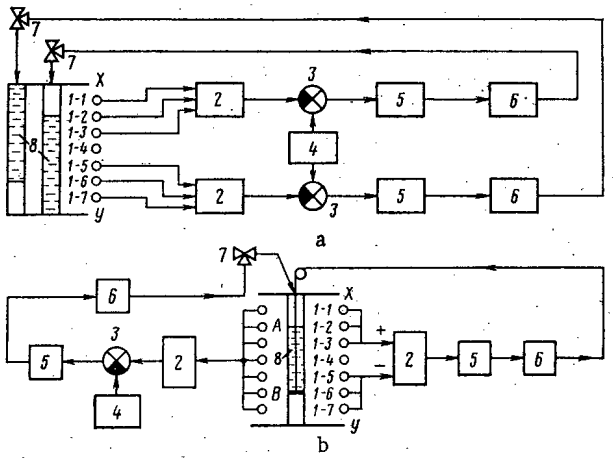

Fig. 5. (a) Layout of one of the 12 identical channels of a system of double-level zone regulation; (b) the same with separate loops for regulation of the radial-azimuthal and height distributions of energy: 1) detectors; 2) integrators; 3) comparison elements; 4) controller; 5) amplifiers; 6) servodrives; 7) valves; and 8) water columns.

Here the level h(t) at any time after the change of the flow rate to Q_2 is determined in terms of the steady-state value of the level h_2 corresponding to the flow rate Q_2 and the initial value of the level h_0.

For small changes in the level relative to the steady value the transfer function of the RU

$$W(p) = \delta h(p)/\delta Q(p) = K_{RU} e^{-\tau p}/(Tp+1), \tag{6}$$

where

$$T = 2Sh/Q; \quad K_{RU} = 2h/Q;$$

where p is the Laplace operator, derived by linearizing Eq. (3) in the neighborhood of the base functions h and Q.

For RBMK [2] S = 50 cm^2, h = 400 cm, and Q = 3.6 m^3/h, we obtain from the expression (5) T = 40 sec and K ≈ 2.2 m of height per 1 m^3/h of flow rate; the transport delay is τ = 2-3 sec.

One can show that the dynamical characteristics of a floating expeller (see Fig. 2b) when its position is controlled by varying the flow rate of the water are described by the transfer function of a stable second-order element. For the dimensions of the expeller and the SCR channel of an RBMK the transfer time of the expeller from one level to another upon a change in the flow rate does not exceed 1 min. As is evident from the diagrams given in Fig. 3, the described RU provide for indpendent control of the zeroth and first height harmonics of the neutron distribution. These RU satisfy the requirements listed above.

Declassified and Approved For Release 2013/03/04 : CIA-RDP10-02196R000300010003-8

Declassified and Approved For Release 2013/03/04 : CIA-RDP10-02196R000300010003-8

The arrangement of the detectors and RU is presented in Fig. 4, and two versions of systems of three-dimensional automatic regulation using the described RU* are presented in Fig. 5. The system presented in Fig. 5a is preferable for use with the RU in Figs. 2a and b. It contains 24 zone regulators with detectors and liquid RU mounted on the upper and lower levels. Three intrareactor upper detectors and two liquid RU as shown in Fig. 2a are used in each of the 12 upper zone regulators. Three lower detectors and two liquid RU as shown in Fig. 2b (it is shown for a single RU in Fig. 5a) are used in each of the 12 lower zone regulators.

The system in Fig. 5b is preferable when RU as shown in Fig. 2c are used in it. It contains 12 zone regulators, which provide for stabilization of the radial–azimuthal energy distribution. All seven sections of the intrareactor height control detector or the radial control detectors with four liquid RU each of the design shown in Fig. 2c are used in each regulator. The power of each of the 12 zones is regulated by varying the water level in the four liquid RU of a given zone. In addition the system contains 12 zonal harmonic regulators, which provide for the regulation (suppression) of the first height harmonic in each of the 12 zones (see Fig. 3). The signal of the three upper detectors in each such regulator is compared with the signal of the three lower detectors, and when a mismatch occurs in the water column in the same four RU, the rods are shifted by a servodrive through the throttle and its rod until the mismatch is removed. During operation this subsystem has practically no effect on the zonal regulators of the radial-azimuthal energy distribution, notwithstanding the RU in common with them. For simplicity's sake one of the four RU is shown in Fig. 5b, to which two regulating actions are simultaneously fed from the two subsystems: variation of the water column height by regulation of the flow rate with a valve, and variation of the position of the water column by the servodrive of the rod.

In the regulation systems presented the power controller should be consistent with the controller of a standard power regulator or be a common one for all the regulators. An integrator of the signals of all the detectors (a "floating" regulator) can be used as the power controller in the systems described, since these systems should only operate together with a standard fast-acting power regulator.

Analysis and synthesis of the multiply connected regulation systems has been performed by well-known [8] methods. The object of regulation – the neutron distribution – is described by a transfer matrix, which relates the variation of the signals from the 24 integrators to changes in the position of the RU, i.e., the positions of the valves controlling the lower and upper water levels in the RU, and the servodrives which move the water columns. This matrix is determined by physical calculation or by direct experiments on a reactor [11]. One should note that in the systems presented only a redistribution of the flow rates through the RU occurs in the regulation process (due to the presence of a fast-acting power regulator responsible for maintaining criticality of the reactor). Therefore hydraulic coupling of the RU through common supply and discharge collectors is absent in practice. Nevertheless it is advisable to specify measures for stabilization of the presence in the supply and discharge collectors of the SCR in order to avoid variations in the characteristics of the RU upon variations in the reactivity reserve being compensated for by them.

Automatic control by RU is also effective when the harmonic regulation method [12-15] is used. In this case the amplitudes of the most weighted first subharmonics (the two first, the two second azimuthal, the first radial and height) are measured to high accuracy with the help of all the detectors existing on the reactor. These harmonics are suppressed "softly" by many liquid RU uniformly distributed throughout the volume of the active zone. Such algorithms have also been presented in [8]. As simulation shows, the role of inoperative detectors and RU is reduced in this method, and a higher accuracy of regulation is achieved with smaller displacements of the RU in comparison with the algorithms of zonal regulation. Of course, optimization algorithms [8, 15] can be used to control the neutron distribution with the help of liquid RU. The cited characteristics and possibilities of liquid RU are confirmed by physical calculations, bench tests, and reactor tests.

LITERATURE CITED

1. N. A. Dollezhal' and I. Ya. Emel'yanov, At. Energ., 40, No. 2, 117 (1976).

*Of course, these same systems can be implemented with standard SCR of an RBMK introduced from below and above.

Declassified and Approved For Release 2013/03/04 : CIA-RDP10-02196R000300010003-8

Declassified and Approved For Release 2013/03/04 : CIA-RDP10-02196R000300010003-8

2. N. A. Dollezhal' and I. Ya. Emel'yanov, A Channel Nuclear Power Reactor [in Russian], Atomizdat, Moscow (1980).
3. P. T. Potapenko, V. G. Dunaev, and N. A. Kuznetsov, At. Tekh. Za Rubezhom, No. 12, 3 (1977).
4. I. Ya. Emel'yanov, R. R. Ionaitis, and V. V. Chernyaev, in: Trudy MVTU "An Investigation of Processes in Power Facilities," Vol. 207, No. 2, 32 (1975).
5. I. Ya. Emel'yanov, R. R. Ionaitis, and I. I. Kryuchkov, ibid., No. 4, 10 (1979).
6. A. Ya. Kramerov and Ya. V. Shevelev, Engineering Calculations of Nuclear Reactors [in Russian], Atomizdat, Moscow (1964).
7. P. T. Potapenko, in: The Control of Nuclear Power Reactors [in Russian], Atomizdat, Moscow (1970), No. 4, p. 5.
8. E. V. Filipchuk, P. T. Potapenko, and V. V. Postnikov, Control of the Neutron Field of a Nuclear Reactor [in Russian], Atomizdat, Moscow (1981).
9. I. Ya. Emel'yanov et al., Inventors' Certificate No. 476825, Byull. Izobret., No. 48, 246 (1978).
10. I. Ya. Emel'yanov, E. V. Filipchuk, and P. T. Potapenko, Inventors' Certificate No. 502031, ibid., 246.
11. S. A. Goloviznin et al., Inventors' Certificate No. 705902, ibid., No. 41, 289 (1980).
12. P. T. Potapenko, Inventors' Certificate No. 701360, ibid., No. 41, 90 (1980).
13. P. T. Potapenko, Inventors' Certificate No. 695379, ibid., No. 23, 28 (1981).
14. P. T. Potapenko, At. Energ., 50, No. 1, 8 (1981).
15. A. A. Anikin and Ya. V. Shevelev, in: Vopr. At. Nauki Tekh., Ser. Fiz. Tekh. Yad. Reactor., No. 3 (12), 35 (1980).

Declassified and Approved For Release 2013/03/04 : CIA-RDP10-02196R000300010003-8

Declassified and Approved For Release 2013/03/04 : CIA-RDP10-02196R000300010003-8

HARMONIC SIMULATION OF A POWER REACTOR

P. T. Potapenko

UDC 621.039.515

The design of the control systems of contemporary power reactors is based on the distributed mathematical model of a reactor. A matrix description of a reactor as a multidimensional control object has been introduced in [1].

The transfer matrix of a reactor relates the vector of the variation of the neutron distribution (ND) in individuals zones or channels to the vector of the variation of the position of the regulating rods (the reactivity), and it is actually adopted as the mathematical model of a reactor [1-5]. The difficulties in the experimental computational determination of the static transfer matrix are associated with the nonunique activation of a reactor to the critical, but more accurately, a steady state [2]. For example, there is no static transfer matrix in a high-powered water-cooled channel reactor (RBMK) even when the automatic power regulator is switched on due to instability of the ND. Isolation of the individual contributions of the first most important harmonics in the reaction of the ND [4, 5] is a nontrivial problem.

The proposed method for construction of the transfer matrix permits eliminating these difficulties by separating the deviations of the ND into a practically instantaneous part and an inertial component caused by the action of delayed neutrons and feedbacks.

With this approach the transfer matrix $\mathcal{H}(p)$ is represented in the form

$$\mathcal{H}(p) \approx \mathbf{M} + \sum_{j=0}^{\nu} J_j(p)\,\mathbf{A}_j. \tag{1}$$

Here **M** is the numerical matrix of the instantaneous component of the ND which describes its reaction during tenths of a second after a change in the position of the rods; ν, number of harmonics of the ND, which is determined by the necessary accuracy of the simulation; $J_j(p)$, transfer function of the j-th harmonic with feedbacks [4-6] taken into account after subtraction of the instantaneous component, which is taken into account by the matrix **M**; p, Laplace operator; and A_j, numerical matrix of the j-th harmonic, whose elements are equal to the relative value of the j-th harmonic excited by the m-th rod in the n-th channel [4, 5]:

$$a^j_{im} = f_{ji} f_{jm} / f_{0i} f_{0m}, \tag{2}$$

where f_{ji} is the value of the j-th harmonic in the i-th channel.

An expression is obtained for $J_j(p)$ from the well-knwon [4-6] transfer function of the harmonic $W_j(p)$ with the instantaneous component taken into account:

$$J_j(p) = W_j(p) - \frac{K_j}{1+K_j}, \tag{3}$$

where $K_j = \beta/\alpha_j^2 M^2$ (β is the fraction of delayed neutrons), α_j^2 is the eigenvalue of the j-th harmonic, and M^2 is the migration are of the neutrons. For example, if $K_{01} = 1$ for the first azimuthal harmonic of an RBMK [4] and

$$W_{01}(p) = \frac{T_0 p + 1}{2T_0 p},$$

Translated from Atomnaya Énergiya, Vol. 53, No. 3, pp. 151-155, September, 1982. Original article submitted November 16, 1981.

 0038-531X/82/5303-0608$07.50 © 1983 Plenum Publishing Corporation

Declassified and Approved For Release 2013/03/04 : CIA-RDP10-02196R000300010003-8

Declassified and Approved For Release 2013/03/04 : CIA-RDP10-02196R000300010003-8

then

$$J_{01}(p) = \frac{1}{2T_0 p}. \tag{4}$$

Here $T_0 = 1/\lambda$, where λ is the average disintegration constant of the sources of delayed neutrons.

One can obtain an equation for calculation of the instantaneous component of the ND deviation φ^*, for example, from the linearized reactor equations [5, 6] in which the power of the delayed neutron sources is taken as constant and appropriate for a steady ND:

$$M^2\nabla^2\varphi^* + (K - 1 - K\beta)\varphi^* + k(1-\beta)\Phi = \tau\frac{\partial\varphi^*}{\partial t}, \tag{5}$$

where Φ and K are the steady ND and neutron multiplication factor, φ and k are their deviations, and τ is the lifetime of the neutrons. If one takes $\tau = 0$, then for a zone with an equalized ND, where $K = 1$ and $\Phi = \text{const}$, we have

$$\nabla^2\varphi^* - \frac{\beta}{M^2}\varphi^* = -\frac{\Phi(1-\beta)}{M^2}k. \tag{6}$$

Equations (5) and (6) are a model of a subcritical reactor (the subcriticality is equal to β) with a neutron source [see the right-hand side of Eq. (6)]. Its solution by a computer presents no difficulty and can be obtained with the help of any reactor program. For a neutron source mounted at the center of an infinite or very large reactor (whose radius $R \gg M$) Eq. (9) has the analytic solution [7]:

$$\varphi^*(r) = BK_0\left(\frac{r\sqrt{\beta}}{M}\right), \tag{7}$$

where K_0 is the zero-order Bessel function of the second kind and B is a normalization factor; upon introduction of a reactivity of 0.01β the change in the average integrated neutron flux $\bar{\Phi}(r)$ should be 1% of the nominal value.

The steady-state static influence function of a critical reactor with a negative power reactivity coefficient $K_p = dk/d\varphi$ is determined for a zone with an equalized ND from the equation

$$\nabla^2\varphi - \frac{K_p\Phi}{M^2}\varphi = -\frac{\Phi}{M^2}k, \tag{8}$$

whose solution in cylindrical geometry is analogous to the solution of Eq. (7):

$$\varphi(r) = DK_0\left(\frac{r\sqrt{K_p\Phi}}{M}\right), \tag{9}$$

the coefficient D is determined by the following condition: upon introduction of a reactivity ρ the average neutron flux Φ should increase by ρ/K_p.

The necessary accuracy of the simulation depends on the type of equations being solved. Thus when analyzing the stability of a system of local automatic regulators (LAR) in an RBMK models with accurate simulation of two-three harmonics of the ND prove to be satisfactory [4]. It is sufficient to model deviations of the ND in the range ±10%. Larger deviations are not permitted by the emergency protection.

Let us estimate the systematic error of the model (1), taking into account that the first ν harmonics in it are simulated without systematic error. Let the values of the amplitudes of the first ν harmonics be equal to Φ_j in the case of a unit local perturbation of the reactivity ($\rho = \beta$). With such a perturbation the instantaneous components of the remaining harmonics do not exceed $K_j/(1 + K_j)$, and their steady-state values with the power reactivity

Declassified and Approved For Release 2013/03/04 : CIA-RDP10-02196R000300010003-8

Declassified and Approved For Release 2013/03/04 : CIA-RDP10-02196R000300010003-8

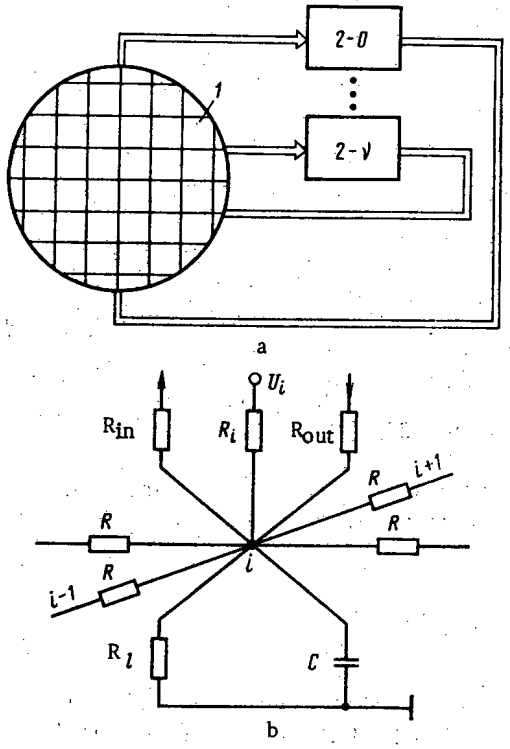

Fig. 1. (a) Structural layout of the analog model and (b) the basic layout of the i-th node of the grid: 1) resistive grid; 2) units for simulation of the harmonics.

coefficient taken into account are $(K_j/(1+K_jK_p\bar{\Phi}/\beta)$ [4-6]. Since $K_j > K_{j+1}$, the relative simulation error does not exceed

$$\varepsilon = \frac{\sum_{\nu+1}^{\infty}\left(\frac{K_j}{1-K_jK_p\bar{\Phi}/\beta}-\frac{K_j}{1+K_j}\right)}{\sum_{j=0}^{\nu}\Phi_j+\sum_{j=\nu+1}^{\infty}\frac{K_j}{1-K_jK_p\bar{\Phi}/\beta}} < \frac{K_{\nu+1}(1+K_p\bar{\Phi}/\beta)\sum_{\nu+1}^{\infty}\frac{K_j}{(1+K_j)(1-K\bar{\Phi}/\beta)}}{\sum_{\nu+1}^{\infty}\frac{K_j}{1-K_jK_p\bar{\Phi}/\beta}}.$$

Strengthening the inequality, we obtain

$$\varepsilon < K_{\nu+1}(1+K_p\bar{\Phi}/\beta) = 100\beta(1+K_p\bar{\Phi}/\beta)/\alpha_j^2M^2, \%. \quad (10)$$

Thus, if the entire simulation range is ±10% of the nominal ND and a simulation accuracy of ε is specified, then in the model (1) one selects the ν first harmonics which satisfy the condition

$$1/\alpha_\nu^2M^2 > \varepsilon/10\beta(1+K_p\bar{\Phi}/\beta). \quad (11)$$

In accordance with this, taking the eigenvalues of the first most important harmonics into account [4, 8, 9], the accuracy of the model (1) for an RBMK is no worse than 3% if one includes the fundamental, first, and second azimuthal harmonics in the number ν. When simulating slow variations of the radial energy distribution of the VVÉR-1000, the equations of subcritical reactor of the type (8) can be adopted as the model.

Digital modeling of the ND of a specific reactor requires satisfaction of the following preparatory operations: 1) calculation of the matrix M and writing it into the memory device (MD) of the computer; 2) calculation of the ν first eigenfunctions of the steady reactor and writing the corresponding elements α_{im}^j [see Eq. (2)] of the numerical matrices A_j for these

Declassified and Approved For Release 2013/03/04 : CIA-RDP10-02196R000300010003-8

Declassified and Approved For Release 2013/03/04 : CIA-RDP10-02196R000300010003-8

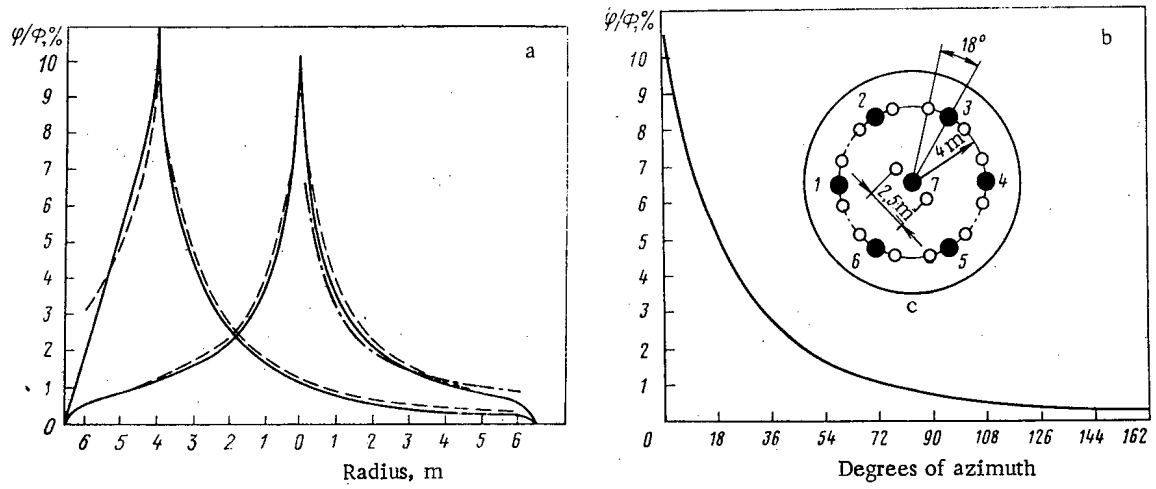

Fig. 2. Instantaneous influence functions of the LAR rods of an RBMK in the (a) radial and (b) azimuthal directions and (c) a chart of the placement of the detectors (○) and the seven LAR rods (●): ——) digital simulation; ---) analog grid model; -·-·-) experiment in a reactor.

harmonics into the MD; and 3) calculation of the transfer functions $J_j(p)$ or formulation of the differential (difference) equations corresponding to them. Naturally, computer simulation consists of multiplication of the transfer matrix $\mathcal{H}(p)$ and the reactivity vector:

$$\varphi(p) = [\mathbf{M} + \sum_{j=0}^{\nu} J_j(p)\,\mathbf{A}_j]\,\rho(p). \tag{12}$$

The operations written here in terms of the Laplace transformation are conveniently carried out on a computer with the help of the apparatus of state space [10]. In order to obtain the matrix M, for example, from Eq. (5) [we set $\partial y/\partial t = 0$], the operator $\nabla^2\varphi^*$ is written in difference form, as a result of which the matrix equation

$$(\mathbf{D} - K\beta\mathbf{I})\,\varphi^* = -\Phi(1-\beta)\,\mathbf{k} \tag{13}$$

is obtained, where I is the unit matrix, D is the difference matrix, and Φ is the diagonal matrix of the nominal ND. Since for model (5) the reactor is subcritical, then the matrix $(D - K\beta I)^{-1}$ is not singular, and

$$\mathbf{M} = -(\mathbf{D} - K\beta\mathbf{I})^{-1}\,\Phi(1-\beta). \tag{14}$$

Effective programs exist for the inversion of sparse matrixes in a multiplicative formula and for storing them in an MD using packing in the form of a coherent copy [11].

An analog model [12] implementing the proposed simulation method consists of a resistive grid and ν operational amplifier units connected to it also through resistors (Fig. 1a). One operational amplifier each is provided for each node of the grid in a traditional analog simulation.

One of the nodes of the resistive grid is presented in Fig. 1b, which simulates, in accordance with the outlined procedure, a subcritical reactor; more accurately, its equalized control zone, where the detectors and rods are mounted. The equation for the i-th node of the resistive grid (see Fig. 1b) is

$$\sum_{n=1}^{4}(U_n - U_i) - \frac{R}{R_{eq}}U_i + \frac{R}{R_i}E_i = RC\frac{dU_i}{dt}, \tag{15}$$

where U_i is the voltage at the i-th node, which simulates the deviation of the ND; n, number of the four nodes adjacent to the i-th one; E_i, source voltage, which simulates the deviation of the safety and control rod (SCR) from its base value (reactivity); R, resistance of the grid resistors; and R_{eq}, resistance of all the resistors connected in parallel to the i-th node:

Declassified and Approved For Release 2013/03/04 : CIA-RDP10-02196R000300010003-8

Declassified and Approved For Release 2013/03/04 : CIA-RDP10-02196R000300010003-8

$$R_{eq}^{-1} = R_i^{-1} + R_{in}^{-1} + R_{out}^{-1} + R_l^{-1}, \tag{16}$$

where R_{in} and R_{out} are the resistances of the resistors which connect the node to the inputs and outputs of the amplifier units, and R_l are the resistances of the load, for example, a detector model. Of course, not all the nodes of the grid are equipped with all the elements presented in Fig. 1b; only the resistors R of the grid are naturally obligatory.

If one writes the operator ∇^2 in Eq. (5) in finite-difference form, then for a zone with a balanced ND it is transformed to the form

$$\sum_{n=1}^{4} (\varphi_n^* - \varphi_i^*) - h^2\beta\varphi_i^* + h^2 k_i (1-\beta)\Phi_i = \tau h^2 \frac{\partial \varphi}{\partial t}, \tag{17}$$

where h is the partition step expressed in migration units. The computational relationships for the grid parameters follow from a comparison of Eqs. (15) and (17) and the adopted scales for k and φ^* :

$$\begin{aligned} &U_i = M_\varphi \varphi_i^*; \; E_i = M_k \Phi_i k_i; \\ &RC = \tau h^2; \; R/R_{eq} = h^2\beta; \\ &RM_k/R_i M_\varphi = h^2(1-\beta). \end{aligned} \tag{18}$$

As has been shown by Ya. V. Shevelev [8], a reactor with a large equalized zone can be replaced with good accuracy by a reactor with a completely equalized ND and a boundary which passes halfway between the reactor boundaries and its equalized zone. In this case the boundary nodes of the resistive grid should be "grounded" through the resistors R_{eq} but not through R. The test for regulation of the boundary "grounded" resistors is: the variation in the neutron flux averaged over the reactor due to an introduced reactivity of $\rho = 0.01\beta$ should amount to 1%.

The transfer functions of the amplifier units are selected so that together with the resistive grid they reproduce the transfer functions of the appropriate harmonics. For example, the appropriate unit to reproduce $W_{01}(p)$ [see Eq. (4)] should have a transfer function for the voltage of $2/(T_0 p + 1)$. For each of the two azimuthal harmonics ($\sin j\varphi$, $\cos j\varphi$) one unit each is provided; the conductivities of the resistors R_{in} and R_{out} are chosen to be proportional to the value of the harmonic being simulated for the reactor cell corresponding to the i-th node.

Examples of the Results. The procedure described has been implemented with digital and analog models of a reactor, the main purpose of which is the investigation of systems for ND Regulation. For example, a program† has been written for digital simulation of the instantaneous component of the ND in an RBMK with a spatial grid spacing of 25 cm, and a grid analog model with a spacing of 50 cm is produced. For illustration the instantaneous influence functions are given in Fig. 2 for the central and peripheral LAR rods of an RBMK [13] when they are withdrawn by 0.01β as obtained with these models and experimentally on an RBMK.‡

The matrix of the instantaneous discontinuity, supplemented by a factor which takes into account the prompt neutrons, which is needed to calculate the LAR within the framework of the first adiabatic model [4], follows from the data and chart of the placement of the LAR rods and detectors which have been given (Fig. 2c):

$$\mathbf{M} = \begin{Vmatrix} 5.0 & 1.3 & 0.4 & 0.2 & 0.4 & 1.3 & 1.0 \\ 1.3 & 5.0 & 1.3 & 0.4 & 0.2 & 0.4 & 1.0 \\ 0.4 & 1.3 & 5.0 & 1.3 & 0.4 & 0.2 & 1.0 \\ 0.2 & 0.4 & 1.3 & 5.0 & 1.3 & 0.4 & 1.0 \\ 0.4 & 0.2 & 0.4 & 1.3 & 5.0 & 1.3 & 1.0 \\ 1.3 & 0.4 & 0.2 & 0.4 & 1.3 & 5.0 & 1.0 \\ 1.0 & 1.0 & 1.0 & 1.0 & 1.0 & 1.0 & 3.0 \end{Vmatrix} \frac{1}{\frac{\tau}{\beta}p + 1} \quad \% \; .$$

†The program and calculation are the work of O. L. Bozhenkov.
‡According to the data of V. V. Postnikov [4].

Declassified and Approved For Release 2013/03/04 : CIA-RDP10-02196R000300010003-8

Declassified and Approved For Release 2013/03/04 : CIA-RDP10-02196R000300010003-8

As has been shown [4], when the LAR of the correcting inverse matrix M^{-1} is incorporated into the system (between the mismatch amplifiers and the comparison elements), autonomy of the local regulators is achieved.

It is important to emphasize that the matrix M of the instantaneous discontinuity does not depend on inertial feedbacks (temperature, vapor, poisoning). Therefore simulation of ND deviations at different power levels requires appropriate fine adjustment of the parameters of model (1) only for the ν harmonics being taken into account. The described harmonic model has been effectively used in connection with the development of algorithms for ND control in a reactor of the Beloyarskaya nuclear power plant [14] and trainers for instruction in the control of RBMK reactors.

Thus, the simulation procedure consists of calculating the steady ND of subcritical reactor and simulating the behavior of its first ν harmonics. It permits shortening the machine time for digital simulation and reducing the amount of equipment needed for analog simulation in comparison with direct programming of the nonsteady equations describing the behavior of the ND.

LITERATURE CITED

1. P. T. Potapenko, At. Energ., 27, No. 3, 189 (1969).
2. A. A. Anikin and Ya. V. Shevelev, Vopr. At. Nauki Tekh., Ser. Fiz. Tekh. Yad. Reaktor., No. 3 (12), 35 (1980).
3. I. Ya. Emel'yanov, P. A. Gavrilov, and B. N. Seliverstov, Control and the Danger of Nuclear Reactors [in Russian], Atomizdat, Moscow (1975).
4. E. V. Filipchuk, P. T. Potapenko, and V. V. Postnikov, Control of the Neutron Field of a Nuclear Reactor [in Russian], Energoizdat, Moscow (1981).
5. P. T. Potapenko, At. Energ., 41, No. 1, 25 (1976).
6. P. T. Potapenko, At. Energ., 50, No. 1, 8 (1981).
7. R. Megreblian and D. Holmes, Reactor Theory [Russian translation], Atomizdat, Moscow (1962).
8. Ya. V. Shevelev, Vopr. At. Nauki Tekh., Ser. Fiz. Tekh. Yad. Reaktor., No. 3, 23 (1980).
9. L. P. Plekhanov, At. Energ., 42, No. 4, 268 (1977).
10. Yu. Tu, Contemporary Control Theory [in Russian], Mashinostroenie, Moscow (1971).
11. R. P. Tewarson, Sparse Matrices, Academic Press (1973).
12. P. T. Potapenko, Inventor's Certificate No. 711879, Byull. Izobret., No. 26, 309 (1981).
13. I. Ya. Emel'yanov et al., At. Energ., 49, No. 6, 357 (1980).
14. O. L. Bozhenkov et al., At. Energ., 51, No. 2, 91 (1981).

Declassified and Approved For Release 2013/03/04 : CIA-RDP10-02196R000300010003-8

Declassified and Approved For Release 2013/03/04 : CIA-RDP10-02196R000300010003-8

REFINEMENT OF BOUNDARY CONDITIONS IN THE CALCULATION OF CLOSE-PACKED LATTICES BY THE SURFACE PSEUDOSOURCES METHOD

N. V. Sultanov and I. A. Zhokina

UDC 539.125.533.348

In reactor calculations it is frequently necessary to solve the kinetic equations in square and hexahedral cells. As a rule these calculations are made in the Wigner–Seitz approximation, replacing the actual cell by a cylindricalized cell with an equal area. In close-packed lattices where the optical thickness of the moderator is less than one neutron mean free path, the details of the boundary conditions at the outside boundary of the cell begin to have a substantial effect on the integral characteristics of cells [1, 2]. By assuming isotropic reflection of neutrons at the outside boundary of a cell, the Wigner–Seitz approximation can be extended to the calculation of cells in close-packed lattices [1, 2]. But even this condition has limited application, particularly if the materials of the inner regions of the cell are strongly absorbing (Table 1). By using the first collision probability method the outer region of the actual cell can be divided into small subregions, and the problem can be solved in two-dimensional geometry [2]. This procedure complicates the calculation and requires increased machine time. Within the framework of the surface pseudosources method [3] we propose boundary conditions which extend the range of application of the Wigner–Seitz approximation for calculating close-packed lattices with practically no increase in machine time.

Using the surface pseudosources method we solve the one-velocity transport equation in a multiregion cylindrical cell. Each region is characterized by constant scattering (Σ_s) and absorption (Σ_a) cross-sections. Neutron scattering is assumed isotropic. A constant neutron source density q is specified in each region. Within the framework of the surface pseudosources method Laletin [3] used a "sink at infinity" condition on the outside boundary of the cell to calculate cells with optically thick outer moderator regions, but this method leads to relatively large errors in calculating close-packed lattices (see Table 1). Calculations showed that the "isotropic sink" condition at the outside boundary of a cell formulated in the present article gives results close to those obtained with the isotropic reflection condition (see Table 1), and the "combined sink" condition leads to results close to those obtained with the reflection condition in actual cells (Tables 1 and 2).

To formulate the neutron reflection condition at the outside boundary of a cell we write the neutron distribution function in the outer region in the form

$$\Psi(\rho, \Omega)=q/\sum_a+\sum_{n,m} Y_n^m(\Omega)\sum_{n',m'} g_{n'm'}G_{n'm'}^{n,m}(\rho/\rho'_{H-1}) + A\Psi_{si}(\rho, \Omega), \quad (1)$$

where the $Y_n^m(\Omega)$ are spherical harmonics normalized in the usual way [4]; the $G_{n',m'}^{n,m}(\rho/\rho_{H-1})$ are the angular moments of the Green's function [3] for an infinite homogeneous on a surface of radius ρ from a source on a surface of radius ρ_{H-1}; the $g_{n',m'}$ are the angular moments of the surface pseudosource on the inside surface of region H: $\Psi_{si}(\rho, \Omega)$ is the contribution to $\Psi(\rho, \Omega)$ from the external neutron sink; A is a constant which is chosen from the condition that there is no net neutron current at the outside boundary of the cell.

In the surface pseudosources method a subsidiary problem is considered for each region, which leads to a problem in an infinite homogeneous medium with the material of the chosen region, and the effect of adjacent regions is taken into account by introducing neutron pseudosources on the boundaries or at some other place. A "sink at infinity" means that the neutron sink is much farther away than one neutron mean free path.

An "isotropic sink" is represented by placing a sink with an isotropic angular distribution of neutrons (Ωn) on the outside boundary of the cell, where n is the normal to the out-

Translated from Atomnaya Énergiya, Vol. 53, No. 3, pp. 155-158, September, 1982. Original article submitted November 3, 1981.

 0038-531X/82/5303-0614$07.50 © 1983 Plenum Publishing Corporation

Declassified and Approved For Release 2013/03/04 : CIA-RDP10-02196R000300010003-8

Declassified and Approved For Release 2013/03/04 : CIA-RDP10-02196R000300010003-8

TABLE 1. Disadvantage Factors

Method	Boundary condition and approximation	Number of cell			
		r_1	r_2	r_3	r_4
Monte Carlo	Specular reflection, hexahedral cell	$1{,}145\times(1\pm0{,}4\cdot10^{-2})$	$1{,}297\times(1\pm0{,}5\cdot10^{-2})$	$1{,}651\times(1\pm0{,}4\cdot10^{-2})$	$2{,}453\times(1\pm0{,}4\cdot10^{-2})$
	Isotropic reflection, cylindricalized cell	$1{,}130\times(1\pm0{,}4\cdot10^{-2})$ (−1,3)*	$1{,}264\times(1\pm0{,}5\cdot10^{-2})$ (−2,5)*	$1{,}600\times(1\pm0{,}4\cdot10^{-2})$ (−3,1)*	$2{,}326\times(1\pm0{,}4\cdot10^{-2})$ (−5,2)*
Surface pseudo-sources method	Sink at infinity				
	G_1*	1,195 (4,4)	1,388 (7,0)	1,818 (10,1)	2,785 (13,5)
	G_3*	1,165 (1,7)	1,340 (3,3)	1,731 (4,8)	2,616 (6,6)
	Isotropic sink				
	G_1†	1,146 (0,1)	1,288 (0,8)	1,620 (1,9)	2,390 (2,7)
	G_3†	1,131 (0,1)	1,273 (0,7)	1,589 (−0,7)	2,318 (−0,3)
	Combination sink				
	G_1*	1,164 (1,7)	1,325 (2,2)	1,694 (2,6)	2,539 (3,5)
	G_3*	1,143 (−0,2)	1,300 (−0,2)	1,644 (−0,4)	2,434 (−0,8)

*Numbers in parentheses are percentage deviations from results for a hexahedral cell calculated by the Monte Carlo Method.

†Numbers in parentheses are approximate percentage deviations from results for a cylindricalized cell with isotropic reflection calculated by the Monte Carlo method.

Declassified and Approved For Release 2013/03/04 : CIA-RDP10-02196R000300010003-8

Declassified and Approved For Release 2013/03/04 : CIA-RDP10-02196R000300010003-8

TABLE 2. Disadvantage Factors

Method or program	Boundary condition and approximation	Number of cell			
		K1	K2	K3	K4
Monte Carlo	Specular reflection, square cell	1,62 (1±0,8××10⁻²)	1,156 (1±0,5××10⁻²	1,147 (1±0,5××10⁻²)	1,157 (1±0,3××10⁻²)
CELTIC [2]	"	1,170 (0,7) *	1,160 (0,4)	1,155 (0,7)	1,152 (—0,4)
PNF-2 [7]	"	1,160 (—0,2)	—	—	—
Surface pseudo-sources method	Skin at infinity				
	G_1	1,192 (2,6)	1,179 (2,0)	1,183 (3,1)	1,199 (3,6)
	G_3	1,176 (1,2)	1,167 (1,0)	1,161 (1,2)	1,168 (1,0)
	Combination sink				
	G_1	1,164 (0,2)	1,174 (1,6)	1,154 (0,7)	1,188 (2,7)
	G_3	1,163 (—0,1)	1,161 (0,4)	1,145 (0,2)	1,155 (0,2)

*Numbers in parentheses are percentage deviations from results calculated by the Monte Carlo method.

Declassified and Approved For Release 2013/03/04 : CIA-RDP10-02196R000300010003-8

Declassified and Approved For Release 2013/03/04 : CIA-RDP10-02196R000300010003-8

side boundary of the cell. Then, using the Green's function for an infinite homogeneous medium, we can write the function $\Psi_{si}(\rho, \Omega)$ in the form

$$\Psi_{si}(\rho, \Omega) = \sum_{n, m} Y_n^m(\Omega)\, G_{1,0}^{n,m}(\rho/\rho_H), \tag{2}$$

and the constant A as

$$A = \sum_{n', m'} g_{n', m'} G_{n', m'}^{1,0}(\rho_H/\rho_{H-1}) / G_{1,0}^{1,0}(\rho_H/\rho_H). \tag{3}$$

To represent a "combination sink" we use the fact that the angular distribution of neutrons entering the cell is shaped in its immediate vicinity at a distance of approximately one neutron mean free path. Since we are considering an infinite uniform lattice, surface pseudosources corresponding exactly to the surface pseudosource of the selected block are distributed over the surfaces of the nearest set of fuel elements.

We note that the component of the neutron flux at the cell boundary arising from the pseudosources of the adjacent fuel elements K contains axial spatial harmonics. Because of symmetry, axial harmonics which are multiples of K remain. In the approximation under consideration we retain only the harmonic with K = 0. The effect of the remaining sets of fuel elements is replaced by a "sink at infinity." Then the function $\Psi_{si}(\rho, \Omega)$ takes the form

$$\Psi_{si}(\rho, \Omega) = \sum_{n, m} Y_n^m(\Omega) \left[\frac{k}{A} \sum_{n', m'} g_{n', m'} G_{n', m', 0}^{n, m, 0}(\rho/\rho_{H-1} r) + G_{as}^{n, m}(\rho/\rho_\infty) \right], \tag{4}$$

where the $G_{n', m', o}^{n, m, o}(\rho/\rho_{H-1})$ are the angular moments of the Green's function from the adjacent block in the coordinate system of the chosen block [5]; the $G_{as}^{n,m}(\rho/\rho_\infty)$ are the angular moments of the Green's function from the "sink at infinity"; k is equal to 4 and 6 for square and hexahedral cells respectively; r is the distance between the centers of symmetry of the chosen fuel element and the fuel elements surrounding it.

Then

$$A = \sum_{n', m'} g_{n', m'} \left[G_{n', m'}^{1,0}(\rho_H/\rho_{H-1}) + k G_{n', m'}^{1,0}(\rho_H/\rho_{H-1} r) \right] / G_{as}^{1,0}(\rho_H/\rho_\infty). \tag{5}$$

Thus, the "combination sink" condition reduces the two-dimensional problem to that of calculating a one-dimensional cylindrical cell.

The modified boundary conditions were introduced into the PRAKTINETs-3 program [6], which was used to calculate two-region hexahedral and square cells. The results were compared with those calculated earlier by the Monte Carlo method for hexahedral and equivalent cylindricalized cells and for square cells [2]. The specular reflection condition was used in calculating actual cells by the Monte Carlo method, i.e., the axial dependence of the neutron distribution was taken into account.

The following initial prameters were assumed for all hexahedral cells: $\rho_1 = 0.3$ cm, $\rho_2 = 0.42$ cm, $\Sigma_a^2 = 0.02$ cm^{-1}, $\Sigma_s^2 = 2$ cm^{-1}, $\Sigma_s^1 = 0.3$ cm^{-1}, $q^1 = 0$, and $q^2 = 1$. For cells numbered Г1-Г4 $\Sigma_a^1 = 0.5$, 1, 2, and 4 cm^{-1}, respectively. Table 1 lists the values calculated for these four cells. It is clear that the values obtained by the surface pseudosources method for an "isotropic sink" are close to those found for isotropic neutron reflection (less than 1% error in the G_3 approximation). The results calculated for isotropic reflection differ by 1-5% from data obtained in calculating actual cells. By using the "combination sink" condition the disadvantage factors are calculated with less than 1% error.

The following initial parameters were taken for all the square cells; $\rho_1 = 0.381$ cm, $\Sigma_a^1 = 0.387$ cm^{-1}, $\Sigma_{tot}^1 = 0.78$ cm^{-1}, $q_1 = 0$, $q_2 = 1$. For cells K1 and K_2 $\rho_2 = 0.86$ cm; for K3 and K4 $\rho_2 = 0.645$ cm; for K1 and K3 $\Sigma_a^2 = 0.0088$ cm^{-1}; $\Sigma_{tot}^2 = 1.0618$ cm^{-1}; for K2 and K4

Declassified and Approved For Release 2013/03/04 : CIA-RDP10-02196R000300010003-8

Declassified and Approved For Release 2013/03/04 : CIA-RDP10-02196R000300010003-8

$\Sigma_a^2 = 0.00587$ cm^{-1}, and $\Sigma_{tot}^2 = 0.70787$ cm^{-1} (see Table 2). For the cells treated by the surface pseudosources method a "sink at infinity" can also be used; by changing to a "combination sink" the disadvantage factors can be calculated with less than a 1% error. Taking account of the fact that the machine time required under these conditions is practically the same (the computation time on a BÉSM-6 computer was increased by 0.005 sec), the "combination sink" is the better choice. In the G_1 and G_3 approximations the calculation of a single region requires 0.15 and 0.27 sec, respectively, on a BÉSM-6 computer.

We have used the isotropic and "combination sink" conditions within the framework of the surface pseudosources method. By using these conditions the Wigner–Seitz approximation can be extended to the domain of close-packed lattices, and the disadvantage factors in the cells considered can be calculated with an error of less than 1% for isotropic reflection in cylindricalized cells and for specular reflection in actual cells. We propose to use the reflection conditions in a multigroup calculation of cells in the MG PRAKTINETs programs [8], which employ the method of decomposition of the operator, with the spatial-angular part of the problem solved by the surface pseudosources method [9, 10].

In conclusion the authors thank N. I. Laletin for his interest in the work and for valuable comments. The results of the calculations of hexahedral and cylindricalized cells by the Monte Carlo method were kindly supplied by the late A. D. Frank-Kamenetskii.

LITERATURE CITED

1. H. Honeck, Nucl. Sci. Eng., 18, 49 (1964).
2. J. Wood and M. Williams, J. Nucl. Energ., 27, 377 (1973).
3. N. I. Laletin, Preprint IAÉ-1374, Moscow (1967); in: Methods of Calculating Thermal Neutron Distributions in Reactor Lattices [in Russian], Atomizdat, Moscow (1974), p. 187; At. Energ., 28, No. 3, 242 (1970).
4. I. S. Gradshtein and I. M. Ryzhik, Tables of Integrals, Series, and Products, Academic Press, New York (1965).
5. N. I. Laletin and N. V. Sultanov, At. Energ., 46, No. 3, 148 (1979); N. V. Sultanov, Preprint IAÉ-3005, Moscow (1978).
6. N. V. Sultanov, Preprint IAÉ-2144, Moscow (1971).
7. V. Yu. Plyashkevich, Preprint IAÉ-2549, Moscow (1975).
8. N. V. Sultanov, Preprint IAÉ-3376/5, Moscow (1981).
9. N. I. Laletin, Vopr. At. Nauki Tekh., Ser. Fiz. Tekh. Yad. Reaktor., No. 5 (18), 63 (1981).
10. N. V. Sultanov, ibid., 69.

Declassified and Approved For Release 2013/03/04 : CIA-RDP10-02196R000300010003-8

Declassified and Approved For Release 2013/03/04 : CIA-RDP10-02196R000300010003-8

GAS RELEASE FROM URANIUM DIOXIDE

V. Sh. Sulaberidze and A. V. Pershin

UDC 621.039.524.44:621.039.542.342

The working parameters of nuclear reactor fuel elements are such that an appreciable part of the fuel doses not reach the temperature at which columnar grains are formed (1900-2000°K). Under such conditions the level of gas release is not determined by the volume diffusion of gaseous fission products (GFP) in the fuel, but by other mechanisms. This is manifested in the change of the temperature dependence of gas release, a complication of the dependence of the relative yield of GFP radionuclides from the fuel on the radioactive decay constant.

The experimental value of the GFP diffusion coefficient is a certain effective parameter reflecting the combined effect of several gas-release mechanisms. It depends also on a number of factors characterizing both the fuel (oxygen content, microstructure) and the experimental conditions (fuel burnup, GFP concentration in the fuel, fission density) [1]. Therefore, in calculating the GFP yield from uranium dioxide in specific fuel elements it is necessary to employ diffusion coefficients obtained for fuel with similar characteristics.

We have determined the temperature dependence of gas release from compact uranium dioxide in the range 770-1700°K for a burnup of up to 1% of the uranium atoms. The GFP yield from a fuel sample was studied by an in-pile method. The experimental arrangement consisted of an irradiation device with the sample and an open helium loop. Gas samples were analyzed with standard spectrometric apparatus using a (Ge)Li detector. Gamma spectra of ^{87}Kr, ^{88}Kr, ^{85m}Kr, ^{133}Xe, ^{135}Xe, and ^{138}Xe were identified.

The fuel was 10% enriched in ^{235}U, had a density of 10.45 g/cm^3, an O/U ratio of 2.006, a mean nominal grain diameter of 6.9 μm, a ratio of volumes of bare and clad surfaces 0.19, and a calculated specific pore surface equal to 460 cm^2/cm^3. The temperature at the center of the sample and on its surface was measured with thermoelectric thermometers. The relative changes of the neutron flux at the sample location were determined from readings of a direct charge transducer with a ^{103}Rh emitter. The absolute value of the thermal neutron flux density in the central cross section of the channel was found from the results of neutron-physical measurements. The error in the measurement of the temperature in the device was ±1%, in the relative change of the neutron flux at the sample location, taking account of the uncertainty of its position in the channel ±1%, in the average fission density in the sample ±15%, and in the release rate of GFP radionuclides from the fuel ±20%.

Changes in the irradiation conditions of the sample were produced by changing its height in the channel, the power of the electric heater, the gaseous medium, and the evacuation of the channel cavity. Three identical samples were irradiated. Sample No. 2, for which the most detailed investigation of the temperature dependence of gas release was made, was irradiated to a dose of $2.4 \cdot 10^{20}$ fissions/cm^3, with a maximum fission density $f_{max} = 8.9 \cdot 10^{12}$ fissions/cm^3·sec.

The dependence of gas release on the fuel temperature was similar for all nuclides investigated. Figure 1 shows the relative yield of ^{85m}Kr(F) from samples as a function of the mean bulk temperature of the fuel T_v. In the temperature range 770-1200°K gas release is independent of the temperature, in good agreement with results in [2] obtained by a similar method.

It should be noted that in investigations by the method of postirradiation annealing the temperature dependence of gas release appears at a lower temperature. Calculations using relations obtained by such a method underestimate the low-temperature yield of GFP, since under in-pile irradiation surface mechanisms ensure a level of gas release appreciably higher than these relations give.

Translated from Atomnaya Énergiya, Vol. 53, No. 3, pp. 158-160, September, 1982. Original article submitted January 19, 1981; revision submitted February 23, 1982.

0038-531X/82/5303-0619$07.50 © 1983 Plenum Publishing Corporation

Declassified and Approved For Release 2013/03/04 : CIA-RDP10-02196R000300010003-8

Declassified and Approved For Release 2013/03/04 : CIA-RDP10-02196R000300010003-8

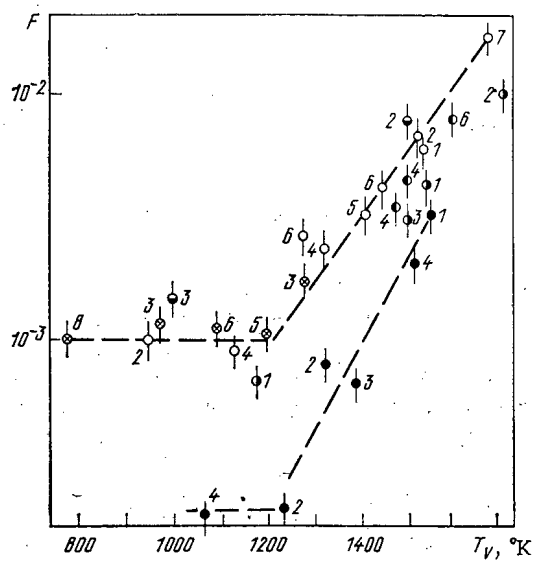

Fig. 1. Relative yield of ^{85m}Kr as a function of the mean bulk temperature: ●) sample No. 1; ○, ◑, ◐, ◒) sample No. 2 (burnup equal to 0, 0.3-0.22, 0.22-0.46, 0.83-1.0, and 1.04%, respectively); ⊗) sample No. 3; the experimental points over which the averaging was performed are numbered.

At a higher temperature the relative yield of GFP increased with increasing temperature. The spread of points corresponding to a different fission density lies mainly within the limits of error of the determination of F; i.e., in the range $(2.7\text{-}8.9)\cdot10^{12}$ fissions/cm^3·sec the GFP release rate is proportional to the fission density.

The observed dependence of the gas release rate on the fission density for a mean bulk fuel temperature $T_V \geqslant 1200$°K is consistent with the diffusion of GFP uranium dioxide.

Table 1 lists values of the activation energy for the diffusion of GFP in the range 1200-1700°K for a burnup of 0.03-0.22% (results of processing data on the GFP yield for sample No. 2 by using the Booth model), kJ/mole.

For a fuel burnup of 0.22-0.46 and 0.83-1.0% the activation energy does not differ appreciably from the values presented (see Fig. 1). Similar values of the activation energy for the diffusion of nuclides of a single element indicate that thermally stimulated diffusion is the predominant mechanism for the release of GFP from uranium dioxide for $T_V \geqslant 1200$°K and $f = (2.7\text{-}8.9)\cdot10^{12}$ fissions/cm^3·sec. However, the activation energy in this case turns out to be lower than the activation energy for volume diffusion, and is essentially an effective parameter taking account of the effect of several gas-release mechanisms.

Figure 2 shows the relative yield of GFP having various radioactive decay constants for three values of the temperature. The experimental results were normalized to the relative yield of ^{133}Xe. The figure also shows the theoretical dependence for a temperature of ∿1700°K predicted by the Booth model, based on the volume diffusion of GFP in fuel. The difference between the experimental and theoretical values, noted in a number of papers, is accounted for by the more effective trapping of short-lived nuclides in fuel [3], the effect of grain-boundary diffusion [4], the trapping of GFP in closed porosity [2], and the diffusion of GFP precursors [5].

Calculations showed that no one mechanism describes the observed dependence of the relative GFP yield on the decay constant (see Fig. 2). The variation of the relative yield of Xe and Kr with the decay constant in the range 10^{-6}-10^{-3} sec^{-1} is better described by a model which takes account of volume diffusion, grain-boundary diffusion, and the diffusion of GFP precursors (curve 5 of Fig. 2). A similar conclusion was drawn by Turnbull and Friskney [6]. At a low temperature the general level of gas release and its dependence on fission density and the radioactive decay constant indicate the action of a mechanism of the "knockout" type. Thus, for in-pile irradiation low-temperature gas release from fuel contained in a shell with

Declassified and Approved For Release 2013/03/04 : CIA-RDP10-02196R000300010003-8

Declassified and Approved For Release 2013/03/04 : CIA-RDP10-02196R000300010003-8

TABLE 1. Estimates of the Spread of the Regression Coefficients and the Mean-Square Deviation of the Average Values

^{85m}Kr	275 ± 16
^{88}Kr	279 ± 19
^{87}Kr	258 ± 19
Average	270 ± 11
^{135}Xe	249 ± 14
^{133}Xe	226 ± 14
Average	237 ± 16

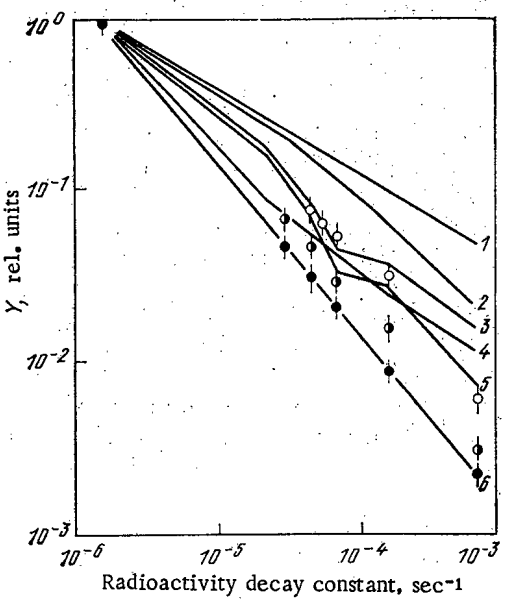

Fig. 2. Reduced relative yield of GFP (Y) as a function of radioactive decay constant. Experiment: ●) T_V = 1000°K; ◑) T_V = 1300°K; ○) T_V = 1700°K. Calculation: 1) volume diffusion; 2) grain-boundary diffusion; 3) diffusion of GFP precursors; 4) trapping of GFP in closed porosity; 5) grain-boundary diffusion (2) and diffusion of precursors (3); 6) "knockout."

a small gap is due to the mechanisms of the type indicated. The temperature dependence of gas release from uranium dioxide directly in the irradiation process appears at a temperature above ∿1200°K, and this temperature limit varies slowly for fission densities from $3 \cdot 10^{12}$ to 10^{13} fissions/cm^3·sec. Between 1200 and 1700°K the GFP yield from compact uranium dioxide is determined by volume and grain-boundary diffusion of GFP and their precursors.

The activation energy for the diffusion of krypton and xenon in the fuel element samples investigated was 270 ± 11 and 237 ± 16 kJ/mole respectively, and did not change for a burnup of up to 1% of the uranium atoms.

LITERATURE CITED

1. G. Lawrence, J. Nucl. Mater., 71, 195 (1978).
2. C. Friskney and J. Turnbull, J. Nucl. Mater., 79, 184 (1979).
3. A. A. Khrulev et al., Vopr. At. Nauk Tekh., Ser. Energ. Tekhnol., No. 2(7), 55 (1977).
4. J. Turnbull and C. Friskney, J. Nucl. Mater., 58, 31 (1975).
5. J. Turnbull et al., ibid., 67, 301 (1977).
6. J. Turnbull and C. Friskney, ibid., 71, 238 (1978).

Declassified and Approved For Release 2013/03/04 : CIA-RDP10-02196R000300010003-8

Declassified and Approved For Release 2013/03/04 : CIA-RDP10-02196R000300010003-8

NEUTRON YIELD OF THE (α, n) REACTION FOR MULTICOMPONENT MEDIA

V. I. Bulanenko, V. V. Frolov,
and E. M. Tsenter

UDC 550.35:357.591

There has been a steady rise in the production and use of α-active nuclides in nuclear engineering, and it is necessary to know the accurate neutron yield Q for the solution of many practical problems, a detailed and reasoned list of which is given in the review [1]. The components of Q are spontaneous nuclear fission and (α, n) reactions in light elements with $Z \leqslant 20$. The importance of taking (α, n) reactions accurately into account is illustrated, e.g., by the result of [2], in which a sharp increase in yield and hardening of the energy spectrum of neutrons when light elements are present in the compounds is demonstrated.

In view of the difference in composition of the set of materials and components actually used, it is preferable to obtain accurate information by calculational means. Whereas the calculation of the neutron yield of spontaneous fission with known nuclear data is not difficult, the calculation of the neutron yield of the (α, n) reaction $Q^{\alpha n}$ is far from obvious. Individual aspects of determining $Q^{\alpha n}$ and its dependence on the α-particle energy and composition of the medium have been considered in a series of works [3-21], but nevertheless there are no published data on the systematic and critical analysis of these calculations, and also on the analysis of sources of error and the possibility of reducing them.

Calculation of the Neutron Yield $Q^{\alpha n}$. Theoretical Formula

It is known that chemical compounds and solutions may be regarded as homogeneous media. Suppose that this medium contains a single radioactive nuclide, emitting r groups of α-particles with initial energy E_{0i} and intensity I_i, and the number of components at whose nuclei (α, n) reactions occur is l. Then, for a homogeneous medium, the neutron yield of (α, n) reactions at nuclei of type j will be

$$Q_j^{\alpha n} = An_j \sum_{i=1}^{r} I_i \int_{B_j}^{E_{0i}} \frac{\sigma_j(E)}{(-dE/dx)}\, dE, \tag{1}$$

where A is the activity of the α emitter; n_j, number of nuclei of type j in unit mass of compound; $\sigma_j(E)$, cross section of the (α, n) reaction at elements of type j; $(-dE/dx)$, energy loss of the α particles in the ionization and excitation of atoms in the medium; B_j, threshold of (α, n) reaction for the j-th nuclide.

Using the Bragg–Kleman sum rule for the stopping power, the neutron yield for a multicomponent medium is obtained

$$Q^{\alpha n} = AN_{\mathrm{Av}} \sum_{i=1}^{r} I_i \sum_{j=1}^{l} \int_{B_j}^{E_{0i}} \frac{\sigma_j(E)}{M_j(-dE/d\rho x)_j} f_j(E)\, dE. \tag{2}$$

Here N_{Av} is Avogadro's number; M_j, mass number of atoms of type j; $f_j(E)$, weighting factor determined by the composition of the medium and expressed in terms of the ionizational α-particle losses in an element of type j in mass units $(-dE/d\rho x)_j$ and the gravimetric fraction of the atoms μ_j:

$$f_j(E) = \mu_j(-dE/d\rho x)_j / \sum_{k=1}^{g} \mu_k(-dE/d\rho x)_k. \tag{3}$$

Translated from Atomnaya Énergiya, Vol. 53, No. 3, pp. 160-164, September, 1982. Original article submitted November 28, 1980; revision submitted February 22, 1982.

 0038-531X/82/5303-0622$07.50 © 1983 Plenum Publishing Corporation

Declassified and Approved For Release 2013/03/04 : CIA-RDP10-02196R000300010003-8

Declassified and Approved For Release 2013/03/04 : CIA-RDP10-02196R000300010003-8

A similar expression for $f_j(E)$, expressed in terms of the mass range ρR, was obtained in [11].

Equation (3) for f_j is valid for any compounds, including aqueous solutions and finely disperse mixtures. For chemical compounds, a weighting factor expressed in terms of the relative atomic stopping power S_j is more expedient, as follows:

$$f_j(E) = N_j S_j(E) / \sum_{k=1}^{g} N_k S_k(E), \tag{4}$$

where N_j is the relative proportion of atoms of type j. Using Eq. (3) or (4), Eq. (2) allows $Q^{\alpha n}$ to be calculated, in principle, for any arbitrary composition. However, such calculations are found to be difficult.

Approximate Formula [3]

It is quickly evident that, when the weighting factor f_j is independent of the α-particle energy, Eq. (2) transforms to the formula proposed in [3] and distinguished by its significant simplicity in practical applications:

$$Q^{\alpha n} = A \sum_{i=1}^{r} I_i \sum_{j=1}^{l} q_j(E_{0i}) f_j(E_{0i}). \tag{5}$$

Here $q_j(E_{oi})$ is the maximum specific neutron yield from a thick target at an energy E_{oi}, and is

$$q_j(E_{0i}) = \frac{N_{Av}}{M_j} \int_{B_j}^{E_{0i}} \frac{\sigma_j(E)}{(-dE/d\rho x)_j} dE. \tag{6}$$

Essentially, q_j is calculated under the condition that the neutron yield is referred to the pure material of type j of the target in which (α, n) reaction is possible, i.e., with $f_j \equiv 1$.

The basis of this approximation is that the relative stopping power does not change much as a function of the energy. In fact, the dependence S(E) is steepest in the low-energy region. At the same time, the cross section $\sigma(E)$ is small at these energies. Therefore, the real contribution to the neutron yield from low-energy α particles is slight. Calculations of $Q^{\alpha n}$ for binary compounds of type $PuBe_{13}$, PuO_2, etc., according to Eqs. (2) and (5) show that Eq. (5) overestimates $Q^{\alpha n}$ by no more than 3%. If values of S averaged over the energy range from B to E_o are used, the accuracy of calculations based on Eq. (5) is increased. According to [20], the energy dependence of f may be neglected in calculating $Q^{\alpha n}$ from Eq. (5) if the value of the ionizational losses is taken at E_o = 5 MeV. For natural α emitters, this gives an additional error of less than ±5%, which is considerably less than the indeterminacy existing in $(-dE/d\rho x)$.

Of course, the limited dimensions of the medium reduce the neutron yield, since some of the α particles of the surface layer do not lead to neutron formation. Since the α-particle path is very small (1-25 mg/cm^2) [11], this effect appears for compounds of small mass ($\sim$0.15 g and less).

Hence, Eq. (5) gives a sufficiently good approximation in calculating the neutron yield for multicomponent media. At the same time, the semiempirical Eq. (5) is markedly preferable to the theoretical Eq. (2), since it is based on q, which may be determined not only by calculation but also by experiment, and may be tabulated. This allows $Q^{\alpha n}$ to be calculated in a considerably shorter time for any chemical compound. Thus, calculating $Q^{\alpha n}$ from Eq. (5) reduces to the separate determination of q, f, A, and I. The components of the error in calculating $Q^{\alpha n}$ are also considered in accordance with this division.

The Error δ_q

The maximum specific neutron yield for the α-particle energy q may be calculated from Eq. (6). Such calculations for several nuclides [5, 9, 10, 13-15] have shown that the dependence of q on the energy is complex.

Declassified and Approved For Release 2013/03/04 : CIA-RDP10-02196R000300010003-8

Declassified and Approved For Release 2013/03/04 : CIA-RDP10-02196R000300010003-8

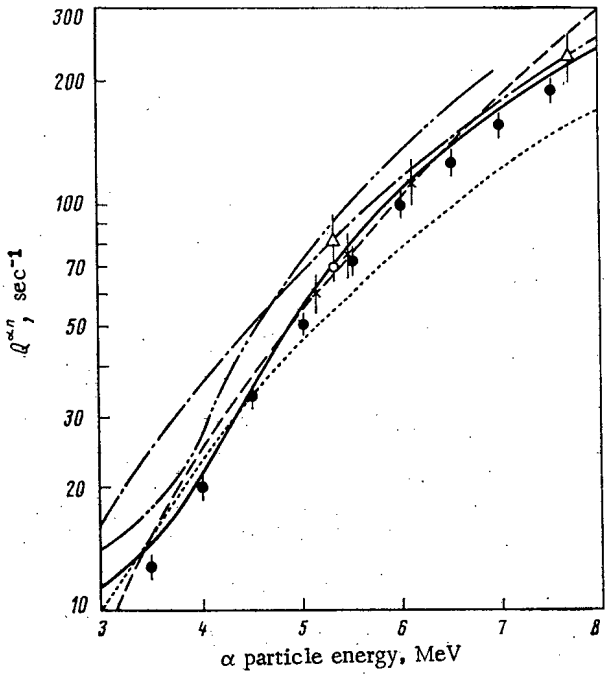

Fig. 1. Dependence of the maximum neutron yield per 10^6 α-particles for a thick beryllium target on the α-particle energy, according to the data of [13] (——), [12] (---), [6] (-·-·-), [7] (....), and [15] (-··-) and the experimental data of [13] (○), [12] (×), [4, 6] (Δ), and [18] (●).

The use of Eq. (6) has certain limitations. First, the detailed structure of the cross section σ(E) is measured for a restricted number of nuclides, mainly at an energy of $\leqslant$5.3 MeV. Second, the ionizational α-particle losses in the energy range below 10 MeV have not been well calculated, and experimental material is inadequate as yet. Third, the absolute values of σ(E) obtained in the measurements have a large indeterminacy (∿15-30%), while these measurements are all that exist for many nuclides.

As a result, the values of q obtained in calculations by Eq. (6) are significantly different from the experimental values. Therefore, it is expedient to normalize the calculated values, which, as is evident, reflect the trend in the curve of the neutron yield as a function of the energy sufficiently well, with respect to reference points obtained in measurements for individual values of the α-particle energy, with an accuracy markedly exceeding the calculated values. Such normalization with respect to reference points is presented in [5, 10, 13]. However, this normalization is not absolute, since the values of q measured by different authors are markedly different. Thus, for the element which has been most studied — beryllium — the reference points chosen were values of q expressed by the number of neutrons per 10^6 α-particles: 84 ± 6 [6] and 69 ± 2 [13], at an energy E_0 = 5.304 MeV. It is evident that more accurate information on the dependence $q(E_0)$ may only be obtained in direct measurements with a thick target in accelerators with a tunable energy. More precise results have been obtained recently in exactly this way [14, 16, 18, 19].

The values of q obtained by different methods are in poor agreement. As an example, the neutron yield for beryllium according to the data of various workers is shown in Fig. 1. This comparison shows that the power-law approximation for $q(E_0)$ [6, 12], which has been widely used, is correct only at the large values of the energy at which it is derived. The semiempirical formula of [7] gives large deviations at both large and small energies. The calculated dpeendence $q(E_0)$ normalized to the most accurate value with an error of 3% [13] gives a value of q 8% larger than the experimental data of [18] and 15% smaller than the calculated data of [15].

Taken together, this indicates that a sufficiently well-founded estimation of the significant data is necessary for each element. Since the recently measured values are known

Declassified and Approved For Release 2013/03/04 : CIA-RDP10-02196R000300010003-8

Declassified and Approved For Release 2013/03/04 : CIA-RDP10-02196R000300010003-8

TABLE 1. Neutron Flux of (α, n) Reactions per Gram of α Emitter for Various Compounds, sec^{-1}

Compound	Error, %				Calculation	Experiment		Calculation/experiment
	δ_q	δ_f	δ_Λ	δ_I				
$^{234}UF_6$	5	10	0,2	0,5	421±50	576±20	[32]	0,73±0,09
$^{238}UF_6$	5	10	0,3	0,5	8,9±1,1	15,0±1,5	[32]	0,59±0,09
$^{239}PuF_3$	5	10	0,2	0,3	$(4,76\pm0,55)\cdot10^3$	$(5,3\pm0,4)\cdot10^3$	[33]	0,90±0,12
$^{239}PuF_4$	5	10	0,2	0,3	$(5,53\pm0,65)\cdot10^3$	$(6,1\pm0,5)\cdot10^3$	[33]	0,91±0,13
						$(7,1\pm0,7)\cdot10^3$	[31]	0,79±0,12
$^{238}PuO_2$	3	5	0,1	0,2	$(1,45\pm0,09)\cdot10^4$	$(1,45\pm0,02)\cdot10^4$	[30]	1±0,06
$^{241}AmO_2$	3	5	0,2	0,3	$(2,88\pm0,17)\cdot10^3$	$(2,78\pm0,41)\cdot10^3$	[17]	1,03±0,16
$^{239}PuBe_{13}$	5	8	0,2	0,3	$(8,09\pm0,77)\cdot10^4$	$(8,43\pm0,44)\cdot10^4$	[12, 36]	0,96±0,10
$^{226}RaBeF_4$ *†	5	8	0,5	0,5	$(2,17\pm0,19)\cdot10^6$	$(2,8\pm0,3)\cdot10^6$	[34]	0,78±0,10
$UO_2(NO_3)_2$ †	3	6	25	1	4,0±1,0	5,2±0,9	[35]	0,77±0,23

*At the stage of radioactive equilibrium.
†Values of $Q^{\alpha n}$ are given for a volume of 1 liter, uranium concentration of 53 g/liter, and 93% enrichment with respect to ^{235}U.

Declassified and Approved For Release 2013/03/04 : CIA-RDP10-02196R000300010003-8

Declassified and Approved For Release 2013/03/04 : CIA-RDP10-02196R000300010003-8

with an error of ∿3-5% and their reestimation in subsequent measurements is possible, a value δ_q 10% should be adopted for most nuclides.

The Error δ_f

The weighting factor takes account of the ratio of the elements in the medium and their ionizational losses, and is determined solely by calculational means from Eq. (3) or (4). The ionizational losses are tabulated in [22-24], on the basis of Bethe—Block theory, the phenomenological approach, and the Lindhard—Sharf theory, respectively. Comparison of theoretical and experimental values of $(-dE/d\rho x)$ show that theory gives reliable results only for elements of moderate Z(Al, Cu). This unsatisfactory situation is associated with inadequate description of the recharging process and with the influence of the electron shells at low α-particle energies. Therefore, the theoretical ionizational losses in [24] were renormalized with respect to known experimental results. These data are regarded as more reliable. Nevertheless, these too require certain corrections, since recently published values of $(-dE/d\rho x)$ differ by 3-20% [25].

Direct measurements of $(-dE/d\rho x)$ or S(E) for U and Pu and their compounds are practically nonexistent. Only two works [26, 27] are known in which the ionizational losses and mass ranges of α particles were measured for carbide and oxide nuclear fuel. The results obtained agree with the results of [24] in the limits 5-15%. The lack of reliable data on $(-dE/d\rho x)$ led in the past to a search for various empirical dependence for S as a monotonic function of Z [4, 21]. However, according to current ideas [24], the dependence S(Z) must be irregular, which is a consequence of individual features in the structure of the electron shells.

Comparison of the weighting factors calculated for a series of compounds from different data shows that the use of $(-dE/d\rho x)$ from [22, 23] leads to values of f 10-40% higher than those of [24]. The use of mass ranges overestimates f by a factor of 1.5-2. Empirical dependences of S [4, 21] give deviations of from −10 to +25%. Taking account of this, and also of the still-inadequate experimental material on $(-dE/d\rho x)$ in heavy elements, it may be concluded that our present level of knowledge does not permit f to be calculated with an error δ_f < 5-8%.

The Error δ_A

The error in the activity value, if it is calculated from the half-life $T_{1/2}$, is evidently due to indeterminacy in the latter. The current state of data on $T_{1/2}$ was considered in detail in [1]. For most nuclides, a value δ_A < 1% has been reached [1, 28]. The only exceptions are individual nuclides for which $\delta_A \geqslant 3\%$.

The Error δ_I

For practically all nuclides, α decay is associated with the emission of several groups of α-particles of different intensity; the energy of the individual groups is sufficiently accurately determined. However, the intensity of individual groups for many nuclides is known with an indeterminacy of 2-5% and higher [29]. Calculations show that for practically all nuclides the mean value of the α-particle energy $\bar{E}_\alpha$ may be used. The calculation error δ_Q for a small substitution does not exceed 1%.

Comparison of the Calculated and Experimental Values of $Q^{\alpha n}$

Most measurements of the neutron yield Q that have been made are relative, and have been performed for neutron sources that are mechanically inhomogeneous mixtures and not chemical compounds. Further, the values of Q obtained have not been normalized to unit mass or to the activity of the α emitter.

Reliable experimental data on $Q_E^{\alpha n}$ which may be compared with the calculated yield $Q_C^{\alpha n}$ are plainly inadequate. To a certain extent this is associated with the need to take correct account of corrections for self-absorption and multiplication of neutrons, absorption by the outer shell of the sample, differences in the energy spectra of the standard and the sample, etc. Typical values of some corrections are given in [30]. The correction for the presence of light-element impurities should be particularly noted. Thus, its neglect in the widely used compound $^{238}PuO_2$ was the cause of contradictory results for the measurement of Q obtained by a series of physicists over the last few years. Only by the use of high-purity samples could the error in measuring Q_E be reduced to 1% [30].

Considerable indeterminacy may also be introduced by the isotopic composition of the heavy element when its mass is reduced to the equivalent number of basic α emitters, taking

Declassified and Approved For Release 2013/03/04 : CIA-RDP10-02196R000300010003-8

Declassified and Approved For Release 2013/03/04 : CIA-RDP10-02196R000300010003-8

account of the difference in α-particle energy and specific α activity. In particular, it is the difference in isotopic composition of plutonium which explains the marked discrepancy in the results for $Q_E^{\alpha n}$ for $^{239}PuF_4$ according to the data of various authors [31]. The difficulties in interpreting such values may be judged from the results of [32], in which, despite measurements with several samples of UF_6 with different isotopic compositions of the uranium, only rough values of $Q_E^{\alpha n}$ were obtained, with an indeterminacy of as much as a factor of 3-4 for $^{235,236}UF_6$.

The yields $Q^{\alpha n}$ for several compounds and the components of the calculational error are shown in Table 1. In estimating $Q_E^{\alpha n}$ from the experimental Q_E, the contribution of spontaneous-fission neutrons was taken into account in accordance with [1]. Furthermore additional corrections were made to the measurements results for some compounds. Thus, for the compound $RaBeF_4$ [34], the contribution of neutrons from (γ, n) reactions was taken to be (5 ± 2)%, while that for (n, 2n) reactions was taken to be (2 ± 1)%. For uranyl nitrate solution [35], the rough corrections for multiplication and absorption was (8 ± 3)%. The value of $Q_E^{\alpha n}$ [12] for the source $^{239}PuBe_{13}$ was 5% too low according to later measurements [36].

In calculating $Q^{\alpha n}$ from Eq. (5), the most reliable data for q [10, 13, 18] and f [24] were used. The errors δ_q and δ_f were chosen on the basis of an analysis of a set of data. As is evident from Table 1, the errors δ_A and δ_I have practically no influence on the total indeterminacy in the yield $Q^{\alpha n}$. The only exception is δ_A for an aqueous solution of uranyl nitrate, in which the ^{234}U content may differ from that adopted in the calculation (1%). Comparison of the yields $Q^{\alpha n}$ shows that the calculated and experimental results are considerably different. This difference is mainly due to imprecise knowledge of the specific and weighting factors.

The following may be said regarding means of further reduction in the calculational error for the neutron yield. Equation (5), proposed in [3], gives a sufficiently good approximation for multicomponent media. Its applicability is mainly justified in that calculations of $Q^{\alpha n}$ prove less troublesome than by Eq. (2). To obtain more accurate results for $Q^{\alpha n}$, a more unambiguous dependence $q(E_0)$ is required, as well as an increase in the number of light elements investigated. It may be suggested that the recent marked rise in interest in the study of charged-particle stopping powers in matter will also facilitate a reduction in the indeterminacy of theoretical values of the neutron yield. A decisive role in reducing the existing indeterminacy in $Q^{\alpha n}$ will undoubtedly be played by direct measurements of the neutron yield for different compositions of high-purity α-emitting nuclides with light elements; the efforts of researchers must be directed toward the execution of such measurements.

LITERATURE CITED

1. N. S. Shimanskaya, Preprint RI-70 [in Russian], Leningrad (1978).
2. T. Gillett, R. Denning, and R. Ridihalgh, Nucl. Technol., 31, 244 (1976).
3. É. M. Tsenter, Izv. Akad. Nauk SSSR, Otd. Tekh. Nauk, No. 1, 159 (1961).
4. G. V. Gorshkov et al., Natural Neutron Background of the Atmosphere and the Earth's Core [in Russian], Atomizdat, Moscow (1965).
5. É. M. Tsenter and A. B. Silin, At. Energ., 19, No. 1, 48 (1965).
6. G. V. Gorshkov and O. S. Tsvetkov, At. Energ., 14, No. 6, 550 (1963).
7. L. N. Korzhov, in: Problems of Dosimetry and Radiation Protection [in Russian], Atomizdat, Moscow (1969), No. 9, p. 44.
8. M. A. Bak and N. S. Shimanskaya, Neutron Sources [in Russian], Atomizdat, Moscow (1969).
9. Experimental Nuclear Physics [Russian translation], Vol. 2, IL, Moscow (1955).
10. V. I. Bulanenko, At. Energ., 47, No. 1, 28 (1979).
11. V. V. Frolov, Nuclear-Physics Methods of Monitoring Fissionable Material [in Russian], Atomizdat, Moscow (1976).
12. O. Runnalls and R. Boucher, Can. J. Phys., 34, 949 (1956).
13. M. Anderson and M. Hertz, Nucl. Sci. Eng., 44, 437 (1971).
14. J. Bair, Nucl. Sci. Eng., 51, 83 (1973).
15. H. Liskien and A. Paulsen, Atomkernenergie, 30, 59 (1977).
16. D. West and A. Sherwood, in: Proceedings of an International Conference on Neutron Physics and Nuclear Data for Reactors and Applied Purposes, Harwell—Paris (1978), p. 610.
17. E. Lees and D. Lindley, Ann. Nucl. Energ., 5, 133 (1978).
18. J. Bair and J. Campo, Nucl. Sic. Eng., 71, 18 (1979).
19. R. Macklin and J. Gibbons, Nucl. Sci. Eng., 31, 337 (1968).

Declassified and Approved For Release 2013/03/04 : CIA-RDP10-02196R000300010003-8

Declassified and Approved For Release 2013/03/04 : CIA-RDP10-02196R000300010003-8

20. D. West, Ann. Nucl. Energ., 6, 549 (1979).
21. M. Taherzadeh and P. Gingo, Nucl. Technol., 15, 396 (1972).
22. C. Williamson, J. Boujot, and J. Picard, Rapp. CEA-R-3042, France (1966).
23. L. Northcliffe and R. Schilling, Nucl. Data Tables, A7, No. 3-4, 233 (1970).
24. J. Ziegler and W. Chu, Nucl. Data Tables, 13, 463 (1974).
25. D. Santry and R. Werner, Nucl. Instrum. Methods, 178, 523, 531 (1980).
26. H. Hirch and H. Matzke, J. Nucl. Mater., 45, 29 (1972).
27. U. Nitzki and H. Matzke, Phys. Rev. B, 8, 1894 (1973).
28. W. Ewbank, Y. Ellis, and M. Schmorak, Nucl. Data Sheets, 26, 1 (1979).
29. A. Rytz, At. Data Nucl. Data Tables, 23, 507 (1979).
30. J. Bair and H. Butler, Nucl. Technol., 19, 202 (1973).
31. É. M. Tsenter et al., in: Proceedings of Third Comecon Symposium on Investigations in the Field of Nuclear-Fuel Reprocessing [in Russian], Vol. 3, Izd. KAÉ ChSSR, Prague (1974), p. 202.
32. T. Sampson, Nucl. Sci. Eng., 54, 470 (1974).
33. V. V. Ovechkin, At. Energ., 48, No. 1, 48 (1980).
34. E. Bretscher et al., Proc. R. Soc., 196, 436 (1949).
35. D. Hankins, Nucl. Sci. Eng., 26, 110 (1966).
36. G. Michaud and R. Boucher, Can. J. Phys., 38, 555 (1960).

Declassified and Approved For Release 2013/03/04 : CIA-RDP10-02196R000300010003-8

Declassified and Approved For Release 2013/03/04 : CIA-RDP10-02196R000300010003-8

YIELDS OF THE PHOTOFISSION PRODUCTS OF ^{237}Np

M. Ya. Kondrat'ko, A. V. Mosesov,
K. A. Petrzhak, and O. A. Teodorovich

UDC 539.173.8:546.799.3

The yields of the photofission products of ^{237}Np by the action of betatron bremsstrahlung have been studied previously by radiochemical [1, 2] and mass-spectrometric [3] methods. In [2], a curve is given for the distribution of the products for a maximum bremsstrahlung energy of E_0 = 14 MeV, constructed from the experimental values of the yields of 24 chains. In [1, 2], the variation of the relative probability of the symmetrical and asymmetrical fission of ^{237}Np with a variation of E_0 from 10 to 24 MeV is traced. The results also are published for the determination of the relative yields of xenon isotopes formed by the fission of ^{237}Np by bremsstrahlung with e_0 = 15 and 20 MeV [3]. There are no data in the literature about the independent yields of the photofission productions of ^{237}Np. Because interest in the systematics of fission product yields and the possible application of these data for the nondestructive determination of fissile substances does not decline, the present paper continued the investigations of the mass and charge distributions of the photofission products of ^{237}Np in the region of the maximum bremsstrahlung energy of 22-28 MeV, using γ-spectrometric and radiochemical methods.

During irradiation, the technique of sampling the recoil fragments from thin layers (200 $\mu g/cm^2$) of fissile material was used. The samples for irradiation contained a few tens of layers of neptunium dioxide (99.9% in ^{237}Np), deposited on a metal backing and adjacent to the collector layers of aluminum foil. The assembly of samples was wrapped up in cadmium foil and irradiated in a linear accelerator with an electron energy of 22-28 MeV and a current of 5-6 μA. The tungsten bremsstrahlung emitter had a thickness of 2.5 mm. The bremsstrahlung incident on the samples was filtered from electrons with a layer of aluminum. The duration of individual irradiations was 5-35 h. The irradiated samples were disassembled by separating the collector foils from the layers of neptunium dioxide.

The procedures for the analysis and determination of the radioactive fission products, and also the system of using the literature data on the decay schemes, were similar to those used for determining the yields of the photofission products of ^{239}Pu [4]. The overall scheme of analysis included: γ-spectrometry of unseparated mixtures of fragments absorbed in the collector foils; γ-spectrometry of the samples obtained after radiochemical separation with carriers; determination of the β-activity of the products, separated and purified as the result of radiochemical analysis, in 4π-counters. The γ-spectrometer with a Ge(Li)-detector with a volume of 40 cm^3 had an energy resolution of about 4 keV for the 1333-keV line. When analyzing the γ-spectra of the unseparated products, the dependence of the area of the total absorption peaks on the time during 5 h to 120 d after irradiation was taken into account.

Table 1 shows the values of the cumulative yields of the photofission products of ^{237}Np, obtained for a maximum bremsstrahlung energy of 22, 25 and 28 MeV. For E_0 = 28 MeV, estimates are also given of the total yields of the chains (last column), obtained by taking account of the corrections, based on experimental data on the independent yields in $^{237}Np(\gamma, f)$ and $^{239}Pu(\gamma, f)$ reactions, and also the systematics of the charge distribution of the products of neutron fission [5]. The absolute values of the yields are estimated by the method of normalization to 200% of the area below the mass distribution curve constructed from the values of the total yields. The yields of the photofission products of ^{237}Np, obtained by the radiochemical method for E_0 = 24 MeV in [2], coincide satisfactorily with the results of the present paper for ^{103}Ru (4.47 ± 0.35%), ^{105}Ru—^{105}Rh (2.65 ± 0.18%), ^{111}Ag (0.74 ± 0.06%), and ^{112}Ag (0.55 ± 0.05%). Appreciable differences are observed for the yields of ^{115}Cd and ^{117}Cd. It should be noted here, that in [2], an obsolete decay scheme was used for the mass number 117 [6]. In the present paper, the yields of the isomers of ^{117}Cd were determined from one of the latest summaries of systemmatized data [7].

Translated from Atomnaya Énergiya, Vol. 53, No. 3, pp. 164-167, September, 1982. Original article submitted November 3, 1981.

0038-531X/82/5303-0629$07.50 © 1983 Plenum Publishing Corporation

Declassified and Approved For Release 2013/03/04 : CIA-RDP10-02196R000300010003-8

Declassified and Approved For Release 2013/03/04 : CIA-RDP10-02196R000300010003-8

TABLE 1. Yields of Photofission Products of ^{237}Np, %

Nuclide	Method of determination*	Maximum bremsstrahlung energy, MeV			
		22	25	28	
^{85m}Kr	a	—	1,02±0,06	1,15±0,11	1,30±0,13
^{88}Kr	a	—	2,41±0,25	2,20±0,24	2,45±0,26
^{91}Sr	a	—	4,07±0,22	4,02±0,21	4,04±0,21
^{92}Y	a	—	4,45±0,18	4,03±0,32	4,03±0,32
^{93}Y	a	—	4,81±0,17	4,59±0,21	4,60±0,21
$^{95}Zr-^{95}Nb$	a	—	5,31±0,21	5,26±0,15	5,26±0,15
^{97}Zr	a	—	5,45±0,16	5,54±0,16	5,69±0,17
^{99}Mo	a	—	5,89±0,21	5,90±0,23	5,91±0,23
^{103}Ru	a	—	4,47±0,28	4,39±0,17	4,39±0,17
^{105}Rh	a	—	2,39±0,21	2,66±0,12	2,66±0,12
^{106}Ru	a	—	—	2,56±0,23	2,56±0,23
^{109}Pd	b	—	0,91±0,06	—	—
^{111}Ag	b	0,594±0,036	0,701±0,056	0,665±0,040	0,665±0,040
^{112}Ag	b	0,492±0,019	0,492±0,042	0,575±0,033	0,575±0,033
^{115}Cd	b	0,319±0,017	—	0,460±0,028	0,467±0,028
^{117m}Cd	b	0,096±0,005	—	0,124±0,007	0,412±0,029
^{117g}Cd	b	0,211±0,018	—	0,271±0,021	
^{127}Sb	a	—	1,44±0,10	1,49±0,06	1,50±0,06
^{129}Sb	a	—	1,95±1,14	1,97±0,12	2,15±0,13
^{131}I	a	—	4,41±0,15	4,53±0,14	4,54±0,14
^{132m}I	a	—	—	0,20±0,13	4,88±0,21
^{132g}I	a	—	4,72±0,13	4,66±0,12	
^{133}I	a	—	5,57±0,25	5,49±0,20	5,61±0,21
^{135}Xe	a	—	6,57±0,19	6,28±0,18	6,34±0,18
^{136}Cs	a	—	0,507±0,065	0,538±0,021	—
^{140}La	a, b, c	4,90±0,18	4,88±0,17	4,87±0,14	4,87±0,14
^{141}Ce	a, b	—	—	4,59±0,26	4,59±0,26
^{143}Ce	b	—	3,66±0,14	3,73±0,13	3,73±0,13
^{144}Ce	b	—	—	3,31±0,19	3,32±0,19
^{145}Pr	c	—	—	2,87±0,17	2,87±0,17
^{147}Nd	a, b	—	—	1,864±0,059	1,864±0,059
^{149}Pm	b	—	—	1,496±0,096	1,496±0,096
^{151}Pm	b	—	—	0,722±0,045	0,723±0,045
^{153}Sm	b	—	—	0,380±0,022	0,380±0,022
^{156}Sm	b	—	—	0,115±0,013	0,121±0,015
^{157}Eu	c	—	—	0,068±0,010	0,068±0,010

*a) γ-spectrometry of unseparated fission product mixtures; b) γ-spectrometry of samples of Pd, Ag, Cd, and total rare-earth fission products; c) determination of the β-activity of the products of radiochemical analysis.

Declassified and Approved For Release 2013/03/04 : CIA-RDP10-02196R000300010003-8

Declassified and Approved For Release 2013/03/04 : CIA-RDP10-02196R000300010003-8

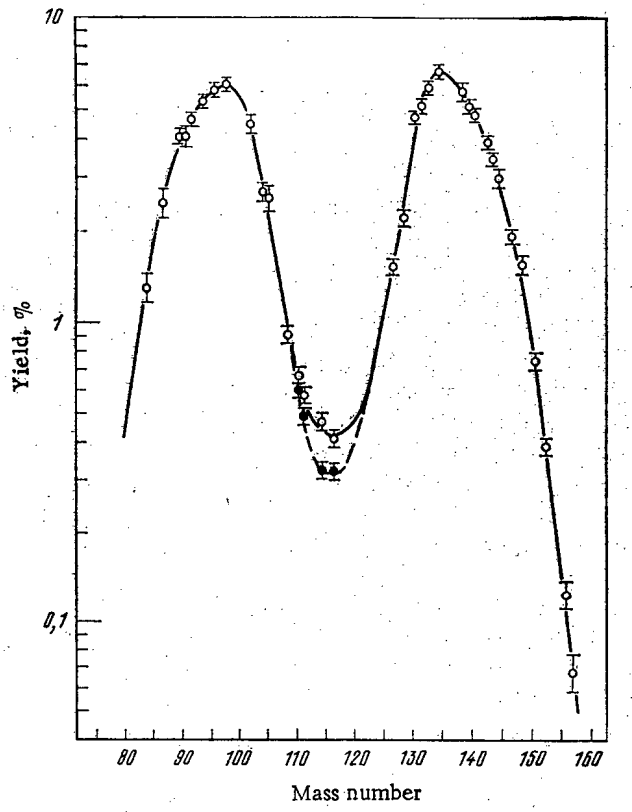

Fig. 1. Curve of mass distribution of the photofission of ^{237}Np for an initial energy of 22 (●) and 28 (○) MeV.

The mass-spectrometric data about the relative yields of xenon isotopes [3], normalized to the yield of ^{131}I, taking account of the correction for the independent yield of ^{130}Cs according to the data of the present paper, coincide with the smooth yield curve.

Normalization of the mass distribution integral to 200% has been given in the present paper to the total yield for A = 140, amounting to 4.88 ± 0.17% with E_0 = 25 MeV and 4.87 ± 0.17% with E_0 = 28 MeV. This coincides with the previously obtained values of 4.83 ± 0.13% with E_0 = 24 MeV [2], which was estimated directly by the method of comparison of the absolute activity of ^{140}Ba + ^{140}La from the total number of fissions in the sample, determined by means of mica detectors.

Table 2 shows the fractional independent yields, obtained by the analysis of the γ-spectra of the unseparated fission products, and also from the ratios of ^{140}Ba and ^{140}La after radiochemical analysis. For E_0 = 25 and 28 MeV, the results coincide within the limits of the errors of the determination, and therefore the averaged values are shown. The most probable values of the charge Z_p also are estimated, calculated on the assumption that the broadening parameter of the charge distribution is identical (σ = 0.59). The values of Z_p, obtained for the photofission of ^{237}Np, are displaced on the average by −0.19 charge units relative to the similar values of Z_p in the reaction ^{239}Pu(γ, f) for E_0 = 28 MeV [4].

Figure 1 shows the curve of the mass distribution of the photofission products of ^{237}Np, constructed from the estimates of the total yields for E_0 = 28 MeV. The distribution corresponds to a predominantly asymmetrical division of the masses from fission. The medium positions of the peaks at the half-height level amount to 96.8 ± 0.2 and 136.9 ± 0.2 amu., respectively, for light and heavy products. An inherent asymmetry is observed in each peak individually, for which a shift of the maxima relative to the medium positions in the direction of the trough in the distribution, is characteristic. The anomalies of the form of the mass distribution can be interpreted as the appearance of a smoothed fine structure. Preliminary analysis showed that in the peaks of the asymmetric fission, on the background of the main approximating Gaussian curves, mutually complementary groups of products are distinguished, with centers at approximately A = 100 and 134.

Declassified and Approved For Release 2013/03/04 : CIA-RDP10-02196R000300010003-8

Declassified and Approved For Release 2013/03/04 : CIA-RDP10-02196R000300010003-8

TABLE 2. Fractional Independent Yields f_i and the Most Probable Charges Z_p in the Photofission of ^{237}Np (E_0 = 25-28 MeV)

Nuclide	f_i	Z_p (σ = 0,59)	Nuclide	f_i	Z_p (σ = 0,59)
^{132m}I	0,041±0,027	—	^{135}Xe	0,249±0,025	53,12
^{132g}I	0,142±0,018	—	^{136}Cs	0,085±0,008	53,69
$^{132}I_{tot}$	0,183±0,032	51,98	^{140}La	0,016±0,004	55,24

One should also mention such anomaly of the mass distribution curve as certain differences in the shape of the peaks of the light and heavy products. The peaks, approximately coinciding in area, differ in the values of the width at half-height: 15.4 ± 0.4 and 14.2 ± 0.4 amu, respectively, for light and heavy products. This difference can be interpreted, by taking into consideration the competition of emission fission at a relatively high energy of excitation of the component nucleus. It follows from the systemmatics of the mass distribution of the fission products, that a change of mass of the fissile nucleus is accompanied by a shift of the peak of the light products, whereas the peak of the heavy products is almost unchanged. In the case of the joint course of the reactions $^{237}Np(\gamma, f)$, $^{237}Np(\gamma, nf)$ and, possibly $^{237}Np(\gamma, 2nf)$, the shift of the peak of the light products leads to its effective broadening in the total distribution.

The weighted mean position of the axis of symmetry of the distribution amounts to 116.96 ± 0.15 amu, which corresponds to an average number of fission neutrons of 3.1 ± 0.2. The averaged ratio of the peak to the trough for E_0 = 28 MeV, is equal to 13.1 ± 0.1.

LITERATURE CITED

1. M. Ya. Kondrat'ko, V. N. Korihets and K. A. Petrzhak, At. Energ., 34, No. 1, 52 (1973).
2. M. Ya. Kondrat'ko et al., At. Energ., 35, No. 3, 211 (1973).
3. K. A. Petrzhak et al., Problems of Nuclear Science and Technology. Series Nuclear Constants [in Russian], No. 24 (1977), p. 15.
4. M. Ya. Kondrat'ko et al., At. Energ., 50, No. 1, 34 (1981).
5. E. Crouch, At. Data Nucl. Data Tables, 19, No. 5, 417 (1977).
6. B. S. Dzhelepov, L. K. Peker and V. O. Sergeev, Decay Schemes of Radioactive Nuclei. A ⩾ 100 [in Russian], Akad. Nauk SSSR, Moscow (1963).
7. R. Auble, Nucl. Data Sheets, 25, No. 2, 315 (1978).

Declassified and Approved For Release 2013/03/04 : CIA-RDP10-02196R000300010003-8

Declassified and Approved For Release 2013/03/04 : CIA-RDP10-02196R000300010003-8

SWELLING IN COLD-DEFORMED OKh16N15M3B STEEL ON IRRADIATION IN A HIGH-VOLTAGE ELECTRON MICROSCOPE

M. M. Kantor, V. N. Kolotinskii,
I. I. Novikov, A. G. Ioltukhovskii,
V. K. Vasil'ev, and N. Yu. Zav'yalova

UDC 621.039.53+537.533.35

Previous cold deformation greatly reduces the swelling of austenitic steel on neutron irradiation at 400-650°C. Conflicting results have come from research on the mechanism of this. For example, it has been found that the reduced swelling in cold-deformed steels of types 316 [1, 2] and OKh16N15M3B [3] is due to reduction in the growth rates of the pores, whose mean size decreases as the degree of deformation rises. However, cold deformation of type 304 steel reduces the rate of pore generation, which reduces the pore concentration and therefore the swelling [4]. The effects of cold deformation on the swelling of type 316 steel indicates [5] that the reduced swelling is due to reduction in the size and concentration of the pores, and the extent of the fall is dependent on the irradiation temperature.

These data indicate that there are several factors influencing the development of radiation porosity in austenitic steels. The contribution from each of the factors is dependent on the structural state and the irradiation conditions. Also, experiments within reactors are complicated and time-consuming.

In a high-voltage electron microscope, the electron energy exceeds the threshold needed to produce the radiation damage in the form of displaced atoms, and this enables one to perform the experiments much more quickly under strictly controlled conditions with continuous recording of the structure changes.

We have examined the effects of previous cold deformation on the development of radiation porosity in an austenitic steel of type OKh16N15M3B by exposing the steel to 1000 keV electrons in a JEM 1000 high-voltage electron microscope fitted with a heating attachment.

The specimens were prepared by jet electrolytic polishing [6]. The electrolyte was a mixture of 23% perchloric acid and 77% glacial acetic acid. The cell voltage was 200 V at 160-180 mA, while the electrolyte temperature was 20°C.

In neutron irradiation, the temperature dependence of the swelling of OKh16N15M3B steel is bell-shaped, with its maximum around 500°C [7], so the specimens were heated to this temperature, which was measured from the calibration curve with an error of not more than ±25°C (±5%). The electron flux density was determined with correction for the beam divergence by means of a Faraday cylinder as about 10^{19} electrons/cm^2·sec. The diameter of the irradiated part was about 3 μm. The vacuum in the microscope column during the experiment was about $3 \cdot 10^{-4}$ Pa. The threshold displacement energy and, therefore, the displacement cross section are very much dependent on the crystallographic orienteation of the specimen with respect to the beam, so the specimen was placed in such a way that the beam passed along the ⟨110⟩ direction. The maximum dose attained in 12 h was $4 \cdot 10^{23}$ electrons/cm^2, which corresponded to about 20 displacements per atom if one assumes tha the overall displacement cross section for iron at 1000 kV is about 50 b [8]. During the experiment, the irradiated part was photographed every 30 min during the first 4 h of irradiation and then every hour.

The usual method [9] was used to determine the quantitative parameters characterizing the porosity, but the local thickness of the irradiated parts of the foil was found from the change in length of projections of dislocations on stereoscopic photographs with differences in angle of 5-10°. The distribution of the pores is distorted by the effects of the free surfaces in very thin parts of the foil [10], so we chose parts of thickness not less than 0.7 μm. We determined the total volume of the pores $\Delta V(V - \Delta V)$, which was taken as equal to the swelling of the steel, as well as the pore concentration. We also examined the pore size distribution and calculated the mean size.

Translated from Atomnaya Énergiya, Vol. 53, No. 3, pp. 167-171, September 1982. Original article submitted November 25, 1981.

0038-531X/82/5303-0633$07.50 © 1983 Plenum Publishing Corporation

Declassified and Approved For Release 2013/03/04 : CIA-RDP10-02196R000300010003-8

Declassified and Approved For Release 2013/03/04 : CIA-RDP10-02196R000300010003-8

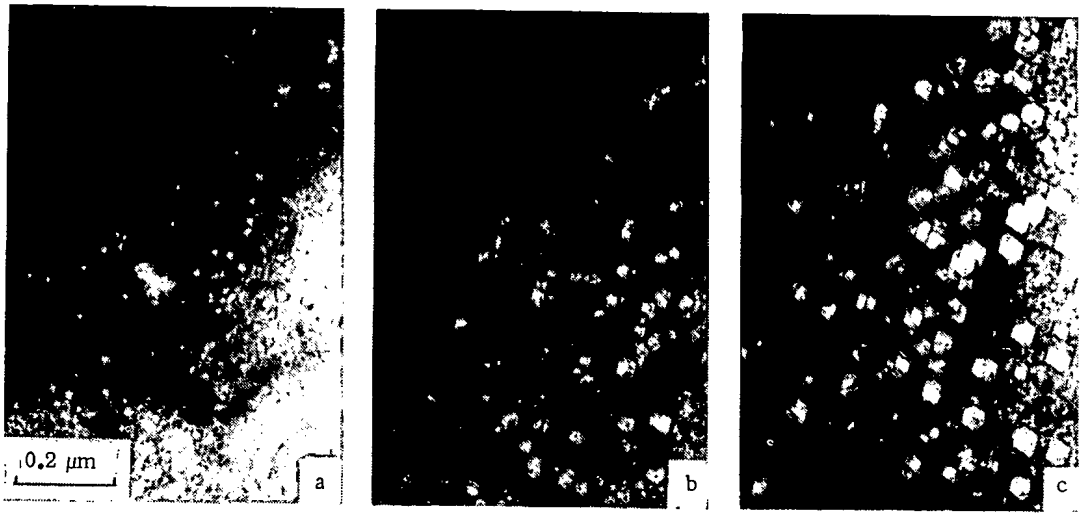

Fig. 1. Electron micrographs of a specimen with 5% cold deformation after 1 (a), 7 (b), and 12 (c) hours of irradiation.

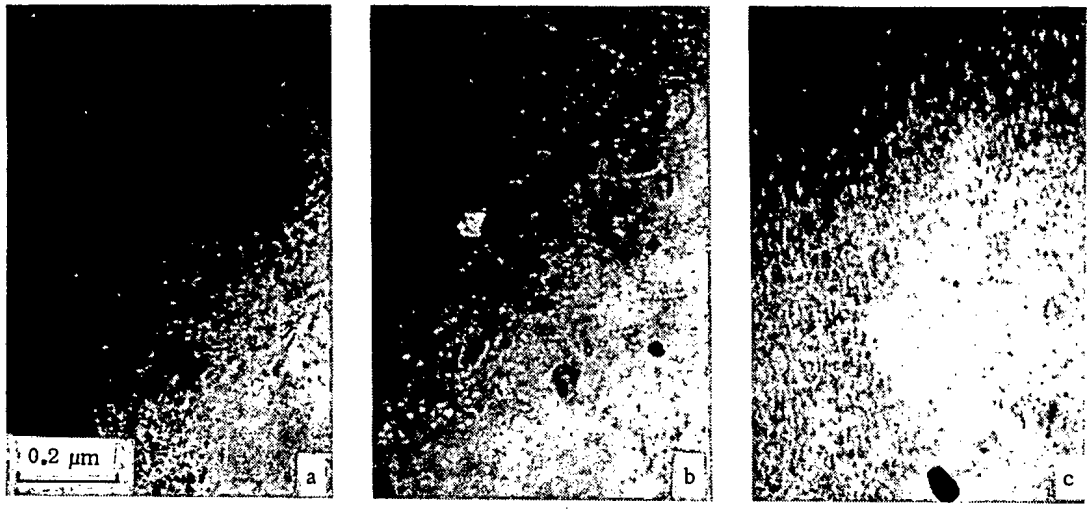

Fig. 2. Electron micrographs of a specimen with 15% cold deformation after 1 (a), 7 (b), and 12 (c) hours of irradiation.

Figure 1 shows electron micrographs for a specimen that had undergone previous 5% cold deformation after 1, 7, and 12 h or irradiation. It is clear that even after 1 h (Fig. 1a) there are distinguishable pores with clear-cut facets. The pore distribution is nonuniform in size and in disposition within the metal. The size and concentration increase with the irradiation time. After 12 h of irradiation (Fig. 1c) it is clear that the pores have the form of slightly truncated or even perfect polyhedra.

The length of the incubation period increases with the degree of cold deformation, this being the time for extinguishable pores to appear. Figure 2 shows that steel previously deformed by 15% even after 7 h produces pores that are smaller (Fig. 2a) than those in steel deformed by 5% after 1 h. As in the case described, the size and concentration of the pores increase with the irradiation time (dose). However, the distribution remains uneven. The concentration is maximal in steel previously cold deformed by 10%. This can be seen by comparing Fig. 3, which shows the distribution in such a specimen after 12 h of irradiation, with Figs. 1c and 2c.

The size distribution is symmetrical with a single peak (Fig. 4) in specimens with various degrees of preliminary cold deformation irradiated to a maximum dose of 20 displacements per atom. One obtains more complicated curves for specimens of steel of this type irradiated in a reactor [7], evidently because there are various additional factors. The centers of the distribution shifts to smaller sizes as the degree of cold deformation in-

Declassified and Approved For Release 2013/03/04 : CIA-RDP10-02196R000300010003-8

Declassified and Approved For Release 2013/03/04 : CIA-RDP10-02196R000300010003-8

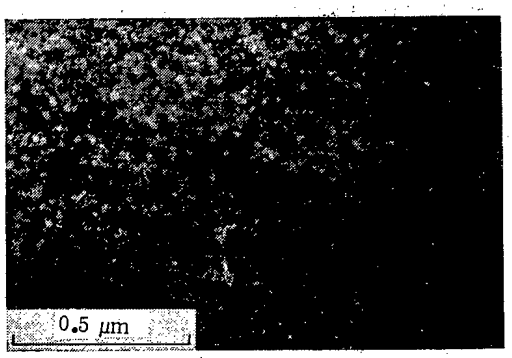

Fig. 3. Electron micrographs of a specimen with 10% cold deformation after 12 h of irradiation.

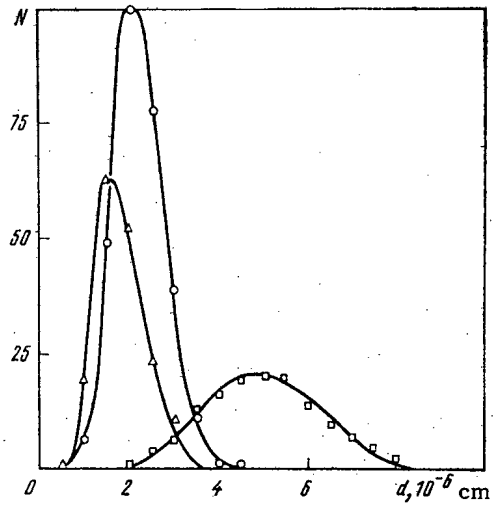

Fig. 4. Size distributions of pores after 12 h of irradiation for 5 (□), 10 (○), and 15% (Δ) cold deformation.

creases, and the spread diminishes. However, the largest pores are observed in specimens given 5% cold deformation.

Figure 5 shows the dependence of the swelling $\Delta V/(V - \Delta V)$, the mean size d, and the concentration ρ on F for three structural states. The linear dependence of $\Delta V/(V - \Delta V)$ on the dose applies only for a steel deformed by 15%. In the other two structural states, this dependence is more complicated: after the linear part up to 13-15 displacements per atom there is a reduction in the swelling rate. This slowing has been observed previously [11], but there are reasons for believing that it is due to the free surfaces. When thicker specimens of austenitic steel type 316 were irradiated under similar conditions, the dependence of the swelling on the dose remained linear to about 70 displacements per atom [12]. The swelling decreases as the initial cold deformation rises.

From $\Delta V/(V - \Delta V) = f(F)$ and $d = f(F)$ one can see that the length of the incubation period increases with the degree of cold deformation (Fig. 5a, b). The end of the incubation period is judged on the occurrence of visible pores, and an increase in the period means that the dose required to produce pores of visible size increases with the degree of cold deformation. Consequently, the incubation period and the corresponding dose characterize the pore growth rate in the initial irradiation period, where the growth kinetics must differ from that observed subsequently (Fig. 5b).

Figure 5b shows that the mean pore size is linearly dependent on the irradiation dose no matter what the degree of deformation. The growth rate determined from the slope of the $d = f(F)$ curve for a specimen with 5% cold deformation is substantially higher than that for one deformed by 10 or 15%.

With a given radiation dose, the pore size is the smaller the higher the degree of preliminary cold deformation.

Declassified and Approved For Release 2013/03/04 : CIA-RDP10-02196R000300010003-8

Declassified and Approved For Release 2013/03/04 : CIA-RDP10-02196R000300010003-8

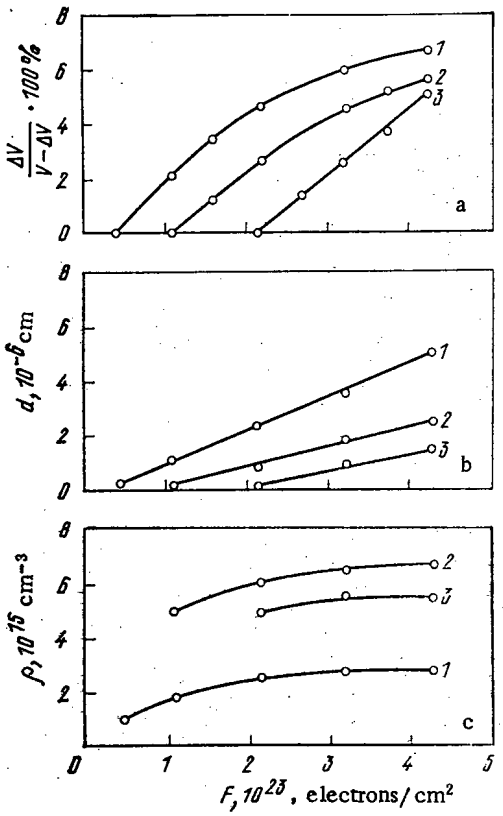

Fig. 5. Dependence of the swelling (a), mean pore size (b), and pore concentration ρ (c) on dose F for 5 (1), 10 (2), and 15% (3) cold deformation.

For all the specimens, the curves relating the pore concentration ρ to dose (Fig. 5c) consist of two parts: initially there is a relatively slow increase in ρ, and a a dose of about 15 displacements per atom the increase in concentration ceases, and the concentration becomes practically constant. The change in ρ in the first part is the less the higher the degree of cold deformation. The peak in the dependence of the pore concentration on degree of cold deformation ε occurs at 10% deformation. A similar peak at 13% deformation has been observed previously [13] in research on the effects of preliminary deformation on the pore concentration in nickel irradiated in a high-voltage electron microscope.

The data on the rise in pore concentration (Fig. 5) indicate that the growth of porosity in type OKh16N15M3B steel in a high-voltage electron microscope is due in the main to growth of the existing pores. The pore growth is retarded the more the higher the degree of preliminary cold deformation.

There is no doubt that the degree of cold deformation influences the growth of porosity in these austenitic steels via its influence on the concentration of sinks for point defects in the structure. There are neutral sinks identical in effectiveness for different point defects and also selective sinks that trap certain defects preferentially. For example, a sink around which there are marked local distortions in the lattice captures interstitial atoms preferentially. The existence of such sinks is a necessary condition for a constant flux of vacancies providing the pore growth.

It seems that the concentration of neutral sinks increases with the degree of preliminary cold deformation. This may be due to the elevated dislocation density, which reduces the performance as selective sinks. As a result, there is a reduced influx of vacancies to the pore nuclei.

High-temperature irradiation reduces the concentration of neutral sinks and raises that of sinks that absorb interstitial atoms preferentially. In this steel, the process may be due to dislocation collapse resulting in a reduced dislocation density or the formation of a Laves phase, which is associated with pore nucleation [3]. The higher the degree of preliminary cold deformation, the more lengthy this process. This is seen as an increase in the incubation period with the degree of deformation. When the selective sinks attain a certain concentration, which is related to the end of the incubation period, there is a change in the pore growth kinetics. From that instant the pore growth accelerates and is linearly dependent on the dose.

Declassified and Approved For Release 2013/03/04 : CIA-RDP10-02196R000300010003-8

Declassified and Approved For Release 2013/03/04 : CIA-RDP10-02196R000300010003-8

The change in neutral sink concentration is related to the peak on the curve relating the pore concentration to the degree of initial cold deformation. Our data and the results of [13] indicate that this peak corresponds to 10-13% deformation.

These results show that irradiation in a high-voltage electron microscope enables one to examine the development of porosity in constructional materials under strictly defined conditions and subject to the effects of a restricted number of factors that influence the process. This is very useful in researching pore nucleation and growth mechanisms and factors that influence these.

LITERATURE CITED

1. C. Cawthorne et al., in: Voids Formed by Irradiation of Reactor Materials, Proc. BNES European Conference (1971), p. 35.
2. T. Kenfield et al., J. Nucl. Mater., 75, 85 (1978).
3. N. P. Agapova et al., in: Actes Conf. Int. Comportem. Irradiat. Mater. Met et Composants Couers React. Rapides, Ajaccio (1979), Supplement, p. 115.
4. I. Stiegler and E. Bloom, J. Nucl. Mater., 41, 341 (1971).
5. H. Brager, ibid., 57, 103 (1975).
6. M. M. Kantor, A. M. Naletov, and V. F. Pichugip, Prib. Tekh. Eksp., No. 4, 221 (1971).
7. V. N. Bykov et al., At. Energ., 36, No. 1, 24 (1974).
8. M. Makin, in: Proc. Ninth Int. Congress on Electron Microscopy, Vol. 3, Toronto (1978), p. 330.
9. U. Wolff, Metallography, 2, 89 (1969).
10. E. Savino, Radiat. Eff., 29, 147 (1976).
11. D. Norris, J. Nucl. Mater., 40, 66 (1971).
12. L. Thomas and R. Fisher, in: Physical Metallurgy of Reactor Fuel Elements, Metal Society, London (1973), p. 161.
13. T. Takeyama, H. Takahashi, and S. Ohnuki, in: Proc. Fifth Int. Conf. on High Voltage Electron Microscopy, Kyoto (1977), p. 571.

Declassified and Approved For Release 2013/03/04 : CIA-RDP10-02196R000300010003-8

Declassified and Approved For Release 2013/03/04 : CIA-RDP10-02196R000300010003-8

STUDY OF THE DEACTIVATION MECHANISMS FOR SOME CONSTRUCTIONAL STEELS BY SECONDARY-ION MASS SPECTROMETRY

Yu. G. Bobrov, S. M. Bashilov,
G. M. Gur'yanov, and A. P. Kovarskii

UDC 621.039.53.537.534

Secondary-ion mass spectrometry SIMS [2] has been used [1] to examine the structure of the oxide films formed on 12Kh18N10T, 48TS, and 22K constructional steels under conditions simulating those in the first loop of boron-regulated pressurized water reactors type VVÉR-440, and also the changes in these films after processing with certain deactivating solutions. The concentration profiles were measured for the components of the alloys in the model films before and after chemical processing. It was found that alkali-permanganate oxidative processing produced selective dissolution of the Cr component of the surface oxide, while there was no appreciable dissolution of the Fe component. Conversely, processing in oxalic acid and also in solutions of some other acids (nitric and citric) or with trilon B produced mainly dissolution of the Fe and Ni components. This nonuniformity in the dissolution makes it necessary to alternate oxidizing and reducing treatments in dissolving chromium-bearing oxide layers.

Transformable recipes have been devised recently to improve the deactivating solutions, in which the redox potential changes without changing the solution, which reduces the amount of radioactive waste. In particular, in deactivating the first loop in a VVÉR-440 reactor with boron regulation one can provide an oxidizing medium in the loop by dispensing potassium permanganate into the boric acid solution. After oxidizing treatment, the solution can be transformed into one of the standard [3] reducing solutions by the addition of trilon B, citric acid, and hydrazine hydrate.

We have used SIMS to examine the changes in oxide films on steels 48TS, 2Kh13, and 12Kh18N10T obtained under conditions simulating those in the first loop of the VVÉR-440 (the constructional elements in this contain these steels) with this type of treatment.

Experimental Methods. The preparation conditions for the model specimens were as in [1]. The polished specimens of the steels of size 10 × 10 × 1.0 were kept for about 1600 h at 300°C in a static autoclave with a solution containing 10 mg/liter of KOH, 5 mg/liter of NH_3, 8 g/liter of H_3BO_3, and 200 mg/liter of $N_2H_4 \cdot H_2O$ (the hydrazine hydrate was introduced to remove the oxygen from the sealed solution on heating). The resulting corrosion layer simulated the dense layers of deposits in the loops of the VVÉR-440. The analysis method differed from that used in [1] in that on ionic bombardment oxygen was admitted to the chamber containing the specimen to a pressure of $4 \cdot 10^{-3}$ Pa, and O_2^+ ions were used as the primary ones with current densities from 1.7 to 2.9 A/m^2.

According to [4], under these conditions the measured current density corresponds most adequately to the elemental composition of the oxide and the substrate alloy.

The figures show the distributions of the components as the ion current for the given element I in pulses/sec in relation to the sampling depth l, which is given in relative units proportional to the current density in the bombarding beams. The broken line shows the nominal oxide–metal boundary estimated from the boron distribution curve.

Figure 1 shows results for a model oxide film on 48TS steel before and after treatment with deactivating solutions: 1) 6 g/liter H_3BO_3 + 2 g/liter $KMnO_4$ + NH_4OH at pH = 7.5; 2) solution 1 + 4 g/liter of trilon B + 1 g/liter of H_3Cit + $N_2H_4 \cdot H_2O$ at pH 5.5; and solution 3 (4 g/liter of trilon B + 1 g/liter of H_3Cit + $N_2H_4 \cdot H_2O$) at pH 5.5. The composition of the steel was mass %: C 0.22-0.27; Si 0.17-0.37; Mn 0.30-0.60; S $\leqslant$ 0.025; Cr 2.5-3.0; Ni $\leqslant$ 0.40; Mo 0.60-0.80; V 0.25-0.35. The following components of the alloy were taken for analysis: Fe, Cr, Mo, and Ni; the processing conditions are indicated in the figure.

Translated from Atomnaya Énergiya, Vol. 53. No. 3, pp. 171-174, September, 1982. Original article submitted August 11, 1981.

 0038-531X/82/5303-0638$07.50 © 1983 Plenum Publishing Corporation

Declassified and Approved For Release 2013/03/04 : CIA-RDP10-02196R000300010003-8

Declassified and Approved For Release 2013/03/04 : CIA-RDP10-02196R000300010003-8

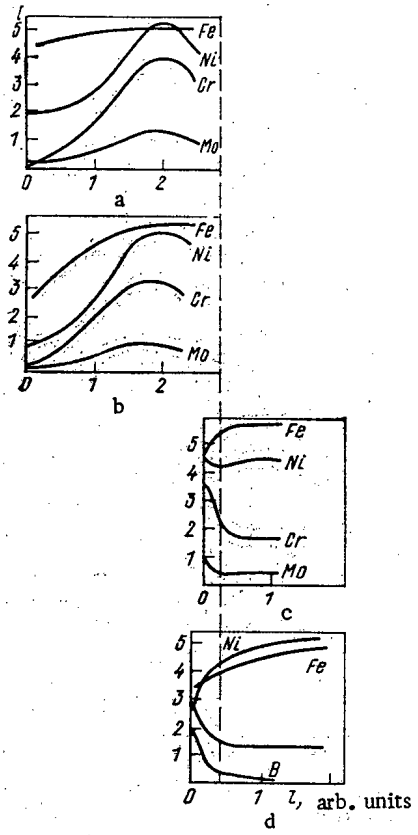

Fig. 1

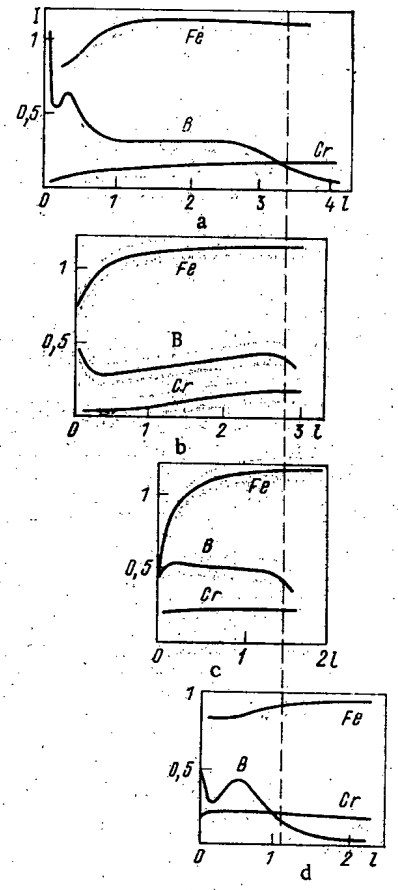

Fig. 2

Fig. 1. Results for SIMS analysis of a model oxide film on 48TS steel before and after processing with deactivating solutions (ion currents for Fe, Cr, Ni, Mo, and B reduced by factors of $2 \cdot 10^6$, 10^6, 10^5, 10^4, and $0.5 \cdot 10^3$, correspondingly): a) initial oxide; b) after oxidative processing in solution 1 (8 h, 97°C); c) after oxidative–reductive processing in solution 1 (8 h, 97°C) and solution 2 (12 h, 97°C); d) after reducing treatment with solution 3 (4 h, 97°C).

Fig. 2. Results of SIMS analysis for a model oxide film on 2Kh13 steel before and after treatment with deactivating solutions (ion currents for Fe, Cr, and B reduced by factors of 10^7, 10^8, and 10^4): a) initial oxide; b) after oxidative treatment with solution 1 (8 h, 97°C); c) after oxidative–reduction treatment with solution 1 (8 h, 97°C) and solution 2 (12 h, 97°C); d) after oxidative–reductive treatment with solution 1 (8 h, 97°C) and solution 4 (15 h, 97°C).

The curves of Fig. 1a show that the model film on 48TS steel is depleted from the surface in the alloy elements Ni, Cr, and Mo. Treatment with boric permanganate (pH $\approx$ 7.4) removes small amounts of Fe and Ni oxides (Fig. 1b), while subsequent treatment of the film with boric permanganate transformed to a reducing system by addition of trilon B, citric acid, and hydrazine hydrate causes almost complete dissolution apart from the chromium-rich layer at the boundary with the metal (Fig. 1c). A similar result is produced in trilon-citrate processing alone (Fig. 1d). Therefore, treatment with the boric permanganate is not essential to remove the oxide film from this steel.

Figure 2 shows results for a model film on 2Kh13 steel before and after chemical treatment with solutions 1, or 1 and 2, or 1 and 4 (solution 1 + 15 g/liter OEDP* + 15 g/liter H_3Cit + KOH) at pH 4. We analyzed for Cr, Fe, and B. The boron distribution curve shows

*Oxyethylidene diphosphoric acid.

Declassified and Approved For Release 2013/03/04 : CIA-RDP10-02196R000300010003-8

Declassified and Approved For Release 2013/03/04 : CIA-RDP10-02196R000300010003-8

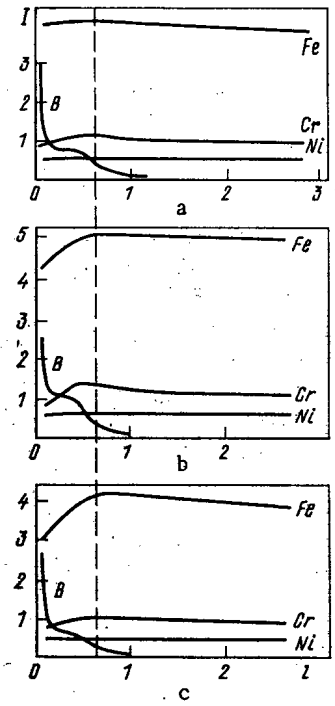

Fig. 3

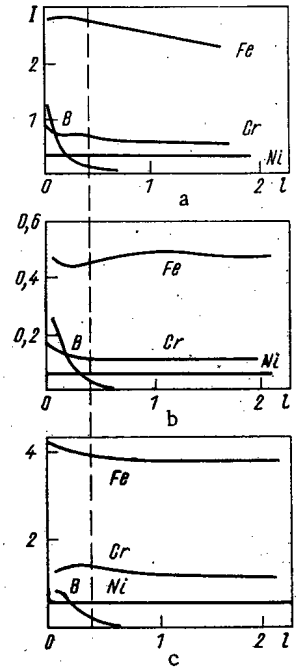

Fig. 4

Fig. 3. Results of SIMS analysis for a model oxide on 12Kh18N10T steel before and after treatment with deactivating solutions (ion currents for Fe, Cr, Ni, and B reduced by factors of $2 \cdot 10^5$, 10^6, $2 \cdot 10^6$, and $5 \cdot 10^3$): a) initial oxide; b) after oxidative treatment with solution 1 (4 h, 97°C); c) after oxidative–reductive treatment with solution 1 (4 h, 97°C) and solution 5 (4 h, 97°C).

Fig. 4. Results of SIMS analysis for a model oxide film on 12Kh18N10T steel after treatment with deactivating solutions (ion current for Fe, Cr, Ni, and B reduced by factors of 10^6, 10^7, 10^7, and 10^4): a) after processing with oxidative solution 1 (8 h, 97°C); b) after oxidative–reductive treatment with solution 1 (8 h, 97°C) and solution 2 (12 h, 97°C); c) after oxidative–reductive treatment with solution 1 (8 h, 97°C) and solution 4 (15 h, 97°C).

that the boric permanganate dissolves a small fraction of the chromium-depleted surface layer in the model film (Fig. 2b). Prolonged treatment with the trilon-citrate mixture after boric permanganate treatment leads to complete dissolution of the chromium-depleted layer, but the layer of oxide close to the metal with the maximum chromium content does not dissolve (Fig. 2c). The same result is obtained on successive treatment with boric permanganate and a mixture of OEDP with citric acid (Fig. 2d).

Figure 3 shows concentration profiles for the components of a model film on 12Kh18N10T steel and the effects of chemical processing with solution 1 and with solutions 1 and 5 (solution 1 + 6 g/liter of H_3Cit + 8 g/liter trilon B + 2 g/liter of urotropine + 1 g/liter of thiourea + NH_4OH) at pH 4.7. The surface layer of the initial film is slightly depleted of chromium (Fig. 3a). Boric permanganate treatment (Fig. 3b) removes some of the iron from the surface. Subsequent trilon-citrate treatment also basically produces this. The boron distribution curve shows that both treatments produce no appreciable dissolution of the film.

Figure 4 shows data for an oxide film on 12Kh18N10T steel obtained by more prolonged maintenance of the specimen in the model coolant (about 2200 h). Under these conditions, the surface layer of the film is substantially depleted in chromium. On treatment with boric permanganate, this layer dissolves (Fig. 4a). Subsequent trilon-citrate treatment (processing conditions as in Fig. 2) depletes the surface layer of iron without appreciable dissolution of the film, as in the previous case (Fig. 4b). On using the OEDP-citrate mixture after boric permanganate treatment there is a certain reduction in the chromium content of the surface layer and also evidently some slight dissolution (Fig. 4c).

Declassified and Approved For Release 2013/03/04 : CIA-RDP10-02196R000300010003-8

Declassified and Approved For Release 2013/03/04 : CIA-RDP10-02196R000300010003-8

CONCLUSIONS

Dense corrosion layers on steels 48TS, 2Kh13, and 12Kh18N10T obtained under conditions simulating the first loop in a boron-regulated reactor are depleted in the alloying elements at the surface. Treatment with boric permanganate (pH $\sim$ 7.4) leads to selective dissolution of the iron and partial dissolution of the iron-rich surface layer of the model oxide. Trilon-citrate recipes dissolve the oxide layers efficiently when these are enriched in iron but are ineffective in dissolving chromium-bearing oxide layers.

Because of these features, the performance in removing model oxide by treatment with these transformable deactivating recipes decreases in the series 48TS, 2Kh13, and 12Kh18N10T. Therefore, a basic problem in devising effective method of deactivating constructions containing low-alloy, stainless, and chromium steels is the prevision in the deactivating solution of conditions favoring relatively uniform dissolution of the oxides of iron (nickel) and the oxides of chromium. None of the recipes considered above satisfies this requirement. Further research is in hand on the possibility of realizing these conditions.

We are indebted to V. E. Ulanov for assistance in the experiments.

LITERATURE CITED

1. S. M. Bashilov et al., At. Energ., 52, No. 2, 122 (1982).
2. V. T. Cherenin and M. A. Vasil'ev, Secondary Ion-Ion Emission from Metals and Alloys [in Russian], Naukova Dumka, Kiev (1975).
3. K. Oertel et al., Kernenergie, 19, No. 4, 129 (1976).
4. J. Pivin, C. Roques-Carmes, and G. Slodzian, Int. J. Mass Spectrom. Ion Phys., 31, 311 (1979).

Declassified and Approved For Release 2013/03/04 : CIA-RDP10-02196R000300010003-8

Declassified and Approved For Release 2013/03/04 : CIA-RDP10-02196R000300010003-8

OPTIMIZATION OF ISOTOPE-SEPARATION PROCESSES IN COLUMNS

V. A. Kaminskii, V. M. Vetsko,
G. A. Tevzadze, O. A. Devdariani,
and G. A. Sulaberidze

UDC 621.039.34

The production of stable isotopes requires large material expenditures, and therefore the optimization of separating installations has a decisive effect on the economics of production. In connection with the separation of isotopes of light elements, it was impossible until recently to solve this problem in general form, owing to the absence of a theory describing the interrelation between the technological parameters of columns and the characteristics of the packings used.

In the present paper, on the basis of [1-3], we propose for the first time a general method for the multiparameter optimization of cascade installations consisting of packed columns. As the target function for the optimization, we selected the cost of the isotope product, which provides a comprehensive characterization of the total expenditures required for the production process and also determines the choice of the most efficient lines of capital investment and the rational limits of improving the quality of production.

In the design of cascade installations consisting of columns, an effort is made to minimize the total volume and to minimize the time required for attaining the stationary state. Both of these conditions are satisfied in ideal cascades. In actuality, an ideal cascade is approximated by a rectangular-section cascade, and the volume of the latter, to which the bulk of the capital expenditures for constructing the installation is proportional, according to [4, 5], can be expressed as follows:

$$V = \frac{4H}{\eta\gamma Q^*\varepsilon^2}\left[P\Phi(c_P) + W\Phi(c_W) - F\Phi(c_F)\right], \tag{1}$$

where $\Phi(c) = (2c - 1)\ln[c/(1 - c)]$; η, efficiency of the shape; H, height of a stage (HETP); Q^*, limiting flow density permitted by the packing; γ, relative load; P, physical productivity of the installation. It should be noted that the expression $\gamma Q^*\varepsilon^2/4H$ is the separating capacity per unit volume of the packed portion of the column.

Low enrichment factors in the separation of nuclides also mean that we must take account of the amount contributed to the cost by the time required to attain a stationary state, t_p, which may reach large values in industrial installations. This quantity may be taken into account by considering the average productivity of the installation per run. If we denote by t_r the time required for one run, then the average productivity P may be expressed as follows:

$$\overline{P} = P(t_r - t_p)/t_r. \tag{2}$$

We shall start with the most general scheme for a rectangular-sectioned cascade, consisting of a stripping section and n enrichment sections, each of which includes m_n parallel-connected columns of identical diameter D with identical packing and identical flow density values. If the length of a section exceeds the permissible column length Z_o, determined on the basis of technical considerations, then in addition to a parallel connection of the columns, a series connection may also be used within the limits of each section, and the number of these columns (rounded off to the nearest unit) will be S_nH/Z_o. Obviously, if the section includes series-connected columns each of which has its own devices for phase conversion, both the operating cost and the capital expenditure will be increased.

Translated from Atomnaya Énergiya, Vol. 53, No. 3, pp. 174-178, September, 1982. Original article submitted June 22, 1981.

 0038-531X/82/5303-0642$07.50 © 1983 Plenum Publishing Corporation

Declassified and Approved For Release 2013/03/04 : CIA-RDP10-02196R000300010003-8

Declassified and Approved For Release 2013/03/04 : CIA-RDP10-02196R000300010003-8

TABLE 1. Structure of the Cost of the Isotope Product for Rectification and Chemical-Exchange Processes

Expenditures	Determining factor	Components of cost	Notation
Capital	Volume of cascade	Unit volume of packing	a_{hv1}
		Columns per unit volume of the packed portion	a_{hv2}
	Circulation flow	Nodes of phase conversion per unit flow	a_{hL1}
		System for utilizing wastes from phase conversion per unit flow	a_{hL2}
	Number of columns	Accessories per column	
		Equipment per column	a_{hm1}
		Automatic devices per column	a_{hm2}
	Feed flow	Purification system per unit feed flow	a_{hm3}
		System of utilization of tailings flow per unit flow	a_{hF1}
			a_{hF2}
Operating	Circulation flow	Energy per unit flow	a_{eL1}
		Coolant per unit flow	a_{eL2}
		Reactants per unit flow	a_{eL3}
	Feed flow	Unit feed flow, taking account of the possibility of realizing tailings	a_{eF1}
		Energy for purifying unit feed flow	a_{eF2}
		Coolant required to purify unit feed flow	a_{eF3}
		Reactants for utilization of unit tailings flow	a_{eF4}
		Wages of operating personnel	a_W
		Shop expenses	$a_{s.e}$

On the basis of the structure of the cost of the isotope product, shown in Table 1, and the expressions (1) and (2) for the cost function C_0, we can write:

$$C_0 = \frac{t_r}{t_a P(t_r - t_p)}\left\{\frac{4H}{\eta\gamma Q^* \varepsilon^2}[P\Phi(c_P) + W\Phi(c_W) - F\Phi(c_F)]\sum_i a_{hvi} + \frac{H}{Z_0}\left(\sum_n L_n S_n + L_W S_W\right)\sum_i a_{hLi} + \right.$$
$$\left. + \frac{H}{Z_0}\left(\sum_n m_n S_n + m_W S_W\right)\sum_i a_{hmi} + F\sum_i a_{hFi}\right\} +$$
$$+ \frac{t_r}{P(t_r - t_p)}\left[\frac{H}{Z_0}\left(\sum_n L_n S_n + L_W S_W\right)\sum_i a_{ei} + F\sum_i a_{eFi} + a_W + a_{s.e}\right], \quad (3)$$

where t_a is the amortization time of the installation; L_n and S_n, flow of one of the phases and the number of stages in the n-th section; F and W, feed and tailings flows. Taking account of the fact that

$$m_n = 4L_n/\pi D^2 \gamma Q^*; \quad (4)$$

$$F/P = (c_P - c_W)/(c_F - c_W); \quad (5)$$

$$W/P = (c_P - c_F)/(c_F - c_W), \quad (6)$$

we can change the expression (3) to the form

$$C_0 = \frac{t_r}{t_r - t_p}\left\{\frac{4H}{t_a \eta\gamma Q^* \varepsilon^2}\left[\Phi(c_P) + \Phi(c_W)\frac{c_P - c_F}{c_F - c_W} + \Phi(c_F)\frac{c_P - c_W}{c_F - c_W}\right]\sum_i a_{kvi} + \frac{H}{Z_0 P}\left[\frac{1}{t_a}\left(\sum_i a_{rLi}\right.\right.\right.$$
$$\left.\left. + \frac{4}{\pi D^2 \gamma Q^*}\sum_i a_{hmi}\right) + \sum_i a_{eLi}\left.\right]\left(\sum_n L_n S_n + L_W S_W\right)$$
$$\left. + \left(\frac{1}{t_a}\sum_i a_{hFi} + \sum_i a_{eFi}\right)\frac{c_P - c_W}{c_F - c_W} + \frac{a_W}{P} + \frac{a_{s.e}}{P}\right\}, \quad (7)$$

Declassified and Approved For Release 2013/03/04 : CIA-RDP10-02196R000300010003-8

Declassified and Approved For Release 2013/03/04 : CIA-RDP10-02196R000300010003-8

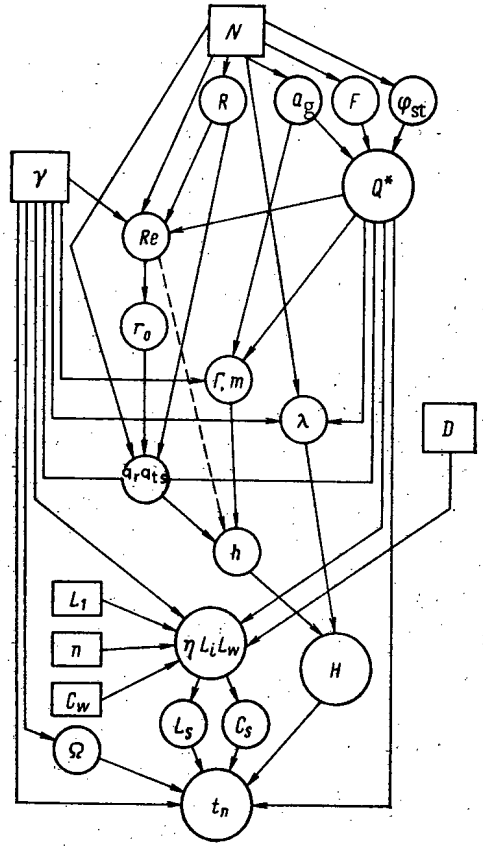

Fig. 1. Scheme for calculating the parameters of the cost function (the squares indicate optimization parameters, the large circles indicate the parameters which are dependent on them and appear in the target function).

where we have summed the expenditures proportional to the volume of the installation, to the total circulation flow, and to the feed flow.

Equation (7) is a multiparameter function with nonlinear relations which is valid in the general case both for a distillation process and for chemical exchange. However, the connections between the parameters for these processes will be somewhat different. For distillation, on the basis of [1-3], they will have the form

$$Q^* = 0.247 \frac{M}{V_{p.r}} \left[\frac{i\rho_l g (F_{fr} - \varphi_{st} - \varphi_d^{*})^3 \varphi_d^{*}}{\rho_g^{0.36} a_k^{1.64} \mu_g^{0.64} (F_{fr} - \varphi_{st})} \right]^{0.735}, \tag{8}$$

where φ_d^* is the dynamic retaining capacity (holdup) of the packing when $\gamma = 1$;

$$H = \frac{iel}{\ln [(1-\lambda) \exp (el/h) + \lambda]}, \tag{9}$$

where

$$h = \frac{1}{\pi D g} \left(1 - \frac{r_0^2}{R^2}\right) \left(\frac{q_r}{6} + \frac{q_{ts}}{4}\right) + \frac{q_{ts}}{12\pi\beta^4 v_*^4 R^2 r_0^2} \times \tag{10}$$

$$\times \left[6 (D_g + \beta v_* r_0)^3 \ln \frac{D_g + \beta v_* r_0}{D_g} - 11\beta^3 v_*^3 r_0^3 - 15 D_g \beta^2 v_*^2 r_0^2 - 6 D_g^2 \beta v_* r_0\right] + \frac{11}{40} \frac{\Gamma_m}{D_l},$$

and the quantities appearing in it are determined according to the formulas

$$q_r = \frac{1.5 V_{o.g}}{N^{2/3}} \frac{R^2 - r_0^2}{R^2 + r_0^2}. \tag{11}$$

Declassified and Approved For Release 2013/03/04 : CIA-RDP10-02196R000300010003-8

Declassified and Approved For Release 2013/03/04 : CIA-RDP10-02196R000300010003-8

TABLE 2. Geometric Parameters of the Packing as a Function of the Number of Elements, and Its Dynamics Retaining Capacity as a Function of the Relative Load

No. of elements per cm^3	Geometric parameters of the packing				ν	φ_d
	R, cm	a_g, cm^{-1}	F_{fr}	l, cm		
5	0,190	13,2	0,884	0,60	0,2	0,069
10	0,150	19,0	0,866	0,47	0,3	0,085
15	0,126	21,3	0,858	0,42	0,4	0,098
20	0,116	23,5	0,853	0,39	0,5	0,109
30	0,104	26,8	0,846	0,35	0,6	0,118
40	0,094	29,0	0,838	0,31	0,7	0,126
60	0,080	33,1	0,825	0,27	0,8	0,133
80	0,070	36,2	0,807	0,24	0,9	0,140
100	0,062	38,0	0,790	0,22	1,0	0,144

Here

$$V_{o.g}=\frac{\gamma Q^* V_{pT}}{M}; \tag{12}$$

$$q_{ts}=\frac{1.5V_{o.g}}{N^{2/3}}-q_r; \tag{13}$$

$$r_0=R\frac{\ln(\mathrm{Re}_g-200)}{\ln(\mathrm{Re}_g-6\cdot10^6/\mathrm{Re}_g)}; \tag{14}$$

$$\mathrm{Re}_g=\frac{3V_{o.g}\rho_g}{\pi N^{2/3}\mu_g R}; \tag{15}$$

$$v_*=\sqrt{\frac{\tau_0}{\rho_g}}=\frac{3.88V_{o.g}}{\pi R^2 N^{2/3}}\left(\frac{a_r\mu_g}{\rho_l V_{o.g}}\right)^{0.32}; \tag{16}$$

$$\Gamma=\gamma Q^*/a_r\rho_l; \tag{17}$$

$$m=\sqrt[3]{\frac{3\Gamma\mu_l}{i\rho_l g}}. \tag{18}$$

In the laminar regime of gas flow in packings with $\mathrm{Re}_g < 1000$, the coefficient $\beta = 0$, and formula (10) reduces to the form

$$h=\frac{q_r}{6\pi D_g}\left(1-\frac{r_0^2}{R^2}\right)+\frac{q_{ts}}{4\pi D_g}\left(1-\frac{1}{2}\frac{r_0^2}{R^2}\right)+\frac{11}{40}\frac{\Gamma_m}{D_l}. \tag{19}$$

In the turbulent region, when $\mathrm{Re}_g > 1000$, we have $\beta = 0.25$.

It should be noted that the height of a stage, determined from formulas (8)-(19), affects not only the capital expenditures but also the operating costs, since it affects the value of the time at which a stationary regime is attained and the number of columns connected in series in one section.

The geometric parameters of the packing – the average dimension R of the inner channel, the specific geometric parameter a_g, and the free-volume fraction F_{fr} – depend on the shape and determining dimension l of the elements, and ultimately on their number per unit volume, N. For one of the most widely used packings – segments of triangular wire spiral – these relations are shown in Table 2. Equation (14) is valid in the range $\mathrm{Re}_g > 200$; when $\mathrm{Re}_g \leq 200$, the initial portion of the hydrodynamic flow is not observed, and $r_0 = 0$. The value of λ, the fraction of the total-stagnation zones, is a function of the number of packing elements per unit volume, the diameter of the column, the relative load, and the limiting discharge capacity. The value of λ is calculated on the basis of the model described in [6] for the flow of a liquid through a packing.

Declassified and Approved For Release 2013/03/04 : CIA-RDP10-02196R000300010003-8

Declassified and Approved For Release 2013/03/04 : CIA-RDP10-02196R000300010003-8

The value of η and the values of L_n and L_W, the flow in each section of the cascade, are determined by solving the problem of approximating an ideal cascade by means of a rectangular section cascade, with given values of the number of sections n and the flow L_1 in the first section. For each section we must satisfy the condition

$$L_n \geqslant \frac{\pi D^2}{4} \gamma Q^*, \tag{20}$$

which precludes an unduly low liquid flow density in the columns when the profile of the cascade is narrowed. In the solution of the approximate problem, the profiles of flows and concentrations required for finding the time it takes to attain a stationary regime are also determined at the same time, as functions of the number of stages. For rectangular-section cascades, this time value may be calculated with satisfactory accuracy on computers by using the method described in [7].

The sequence of operations in the preparation of the parameters appearing in the target function for the optimization is shown in Fig. 1. From the scheme of Fig. 1 it can be seen that there are six independent optimization parameters: N, the number of packing elements per unit volume, which depends on the dimension of the element; the relative load γ; the column diameter D; the flow L_1 in the first section of the cascade; the number n of sections of the cascade; and the concentration in the tailings, c_W. The other parameters appearing in formula (7), such as Q^*, η, L_n, L_W, and t_p, are found in the calculation process. In solving the problem we must start from a specific separation problem in which we are given the productivity P of the installation and the product concentration c_p. We must also determine in advance the duration of a run and the amortization period of the installation, t_a.

The physical parameters of the working fluid, such as the gas and liquid densities ρ_g and ρ_{liq}, viscosities μ_g and μ_{liq}, autodiffusion coefficients D_g and D_{liq}, volume of a gram-mole under operationg conditions $V_{p,T}$, and enrichment factor ε will, in the general case, be functions of temperature and may vary if we introduce the temperature of the process as one the optimization parameters. In this case the relations between the parameters of the target function given by conditions (8)-(20) and the sequence of their calculation shown in Fig. 1 will not change. The minimum of the target function may be determined by various methods, of which the most attractive from the viewpoint of rapid convergence is the deformed-polyhedron method [8].

In Figs. 2-4 we show the results obtained by using the proposed method on the example of optimization of an installation for the production of 10 kg/yr of ^{13}C with a concentration of 95%, produced by the method of rectification of carbon monoxide. The optimal values of the optimization parameters are: N = 80 cm^{-1}; γ = 0.65; D = 6.2 cm; L_1 = 14.1 g/sec; c_W = 0.44%; n = 2. The optimal installation is a three-section cascade with 10 parallel-connected columns in the first section and the stripping section and with one column in the second section. The total length of the cascade is 38 m, the shape efficiency is 0.75, and the ratio of the first-section flow to the minimum flow is 1.56.

The optimal packing was found to be one with fairly small dimensions; the cost was found to be only slightly dependent on the optimization parameters in the region of their optimum values. This factor increases the possibilities of acceptance of convenient technical solutions when specific installations are designed.

Analyzing this example, especially the relation between the various types of expenditures, we should bear in mind that it cannot be of a general nature, since it depends to a large extent on the scale of the production, the site of the installation, marked-price conditions for the raw material, other materials, and equipment, the degree of automation, etc. Therefore, the nature of this relation may vary considerably not only for processes in which different isotopes are separated by also when the same process is handled by different approaches. Thus, if we increase the productivity of the installation, the fraction of the cost represented by wages and shop expenses will be substantially decreased, while the fraction represented by capital expenditures will correspondingly increase. A considerable increase in the fraction represented by capital expenditures also results from a decrease in the separation factor and from a low cost of the initial raw material.

At the same time, the proposed approach to the optimization process is fairly general, since it enables us, by using the appropriate cost coefficients and parameters of the mixture being separated, not only to take account of all of the above-mentioned factors but also to

Declassified and Approved For Release 2013/03/04 : CIA-RDP10-02196R000300010003-8

Declassified and Approved For Release 2013/03/04 : CIA-RDP10-02196R000300010003-8

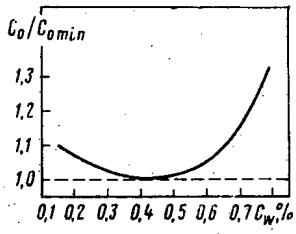

Fig. 2. Cost as a function of the concentration of ^{13}C in the tailings.

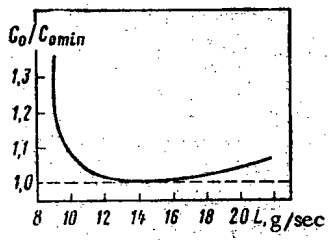

Fig. 3. Cost as a function of the flow in the first section of the cascade.

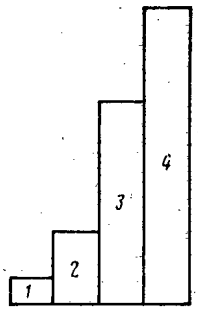

Fig. 4. Relation between various types of expenditures in the production of 10 kg/yr of ^{13}C: 1) capital expenditures; 2) raw-materials costs; 3) cost of energy and coolant; 4) wages and shop expenses.

solve a number of special problems relating to the desirability of using heat-pump schemes, determining the rational level of automation, etc. In the first case it is the relation between the capital and energy expenditures that varies, and in the second case it is the relation between the capital expenditures and the wages. Furthermore, by using a subdivided approach, we can carry out an optimization with respect to the conditions of realization of the process (temperature and pressure conditions), taking account of the way in which the parameters of the mixture being separated vary with temperature; it should be noted that the solution of this problem within the bounds of a multiparameter optimization of the installation, designed for the solution of a specific separation problem, is more correct than considering a process selected for an individual case, as was done in the past.

LITERATURE CITED

1. V. A. Kaminskii and N. A. Giorgadze, Isotopenpraxis, 9, No. 1, 1 (1973).
2. V. A. Kaminskii, N. A. Giorgadze, and V. P. Kovtun, ibid., 14, No. 9, 321 (1978).
3. V. A. Kaminskii and N. A. Giorgadze, Kernenergie, 14, No. 6, 194 (1971).
4. M. Benedict and T. Pigford, Chemical Technology of Nuclear Materials [Russian translation], Atomizdat, Moscow (1960), p. 423.
5. A. M. Rozen, Theory of Isotope Separation in Columns [in Russian], Atomizdat, Moscow (1960), p. 240.
6. V. A. Kaminskii, et al., Teor. Osn. Khim. Tekhnol., 11, No. 6, 872 (1977).
7. N. I. Laguntsov, E. V. Levin, and G. A. Sulaberidze, Inzh.-Fiz. Zh., 31, No. 3, 506 (1976).
8. J. Nelder and R. Mead, Computer J., 7, 308 (1964).

Declassified and Approved For Release 2013/03/04 : CIA-RDP10-02196R000300010003-8

Declassified and Approved For Release 2013/03/04 : CIA-RDP10-02196R000300010003-8

DETERMINING DISTRIBUTION AND CONCENTRATION OF CERTAIN ELEMENTS WITH THE AID OF A CHARGED-PARTICLE BEAM

I. G. Berzina, É. B. Gusev,
A. V. Drushchits, V. S. Kulikauskas,
and A. F. Tulinov

UDC 539.172.12/16:549.1

The methods used in practice to determine the elements of which a substance is composed usually require destruction of the object to be examined and do not allow a selective simultaneous determination of both the distribution and the concentration of several elements. The distribution of the local concentration of elements in the object to be examined must be studied in many problems which are associated with the development of techniques of introducing microimpurities into various materials to improve their properties or of determining the paths over which elements migrate in the crust of the earth (search for useful minerals). Only a small number of methods of determining the local concentration of elements without destroying the object to be examined are known; practically no methods are available for the simultaneous determination of the local concentration and the selective determination of the distribution of several elements, particularly those with $Z \leqslant 20$ in multicomponents objects.

The present work refers to a method of elementary analysis which can be used for the selective simultaneous determination of the local concentrations of lithium, boron, oxygen, nitrogen, and fluorine with the aid of the (p, α) reaction and, besides that, with the (α, n) reaction for determining beryllium in micro- or macrosections of multicomponent objects. The analysis was made with equipment consisting of a source of charged particles (accelerator), a collimating device, an evacuated measuring chamber, and recording apparatus [1].

In order to increase sensitivity and resolution of the analysis, a doublet of magnetic quadrupole lenses and a scanning instrument were built. The dimensions of the ion beam were defined with a collimator which consisted of two blocks of removable diaphragms. These diaphragms could be used to cut from the beam an almost monoenergetic central portion with a diameter between 1 and 0.1 mm. This central portion was focused with the magnetic lenses. Depending upon the dimensions of the inhomogeneities in the object to be examined, the proton beam diameter was varied between 200 and 10 μm. The scanning instrument consisted of two perpendicular deflectors, sawtooth voltage generator, and a high-voltage supply with continuous voltage adjustment. The beam wobbling at a distance of 200 mm from the end of the deflector plates reached about 10 mm at a plate voltage of 1 kV.

When a focused beam of charged particles was used for the analysis, the current density at the target could reach values which led to burning and destruction of the sample in the section where the beam was incident. Therefore the beam density must be chosen for each object to be examined so that the analysis does not lead to burning of the sample, i.e., to a falsification of the results of the analysis. The fact that no burning occurs can be recognized from the stability of the secondary radiation density measured over successive time intervals in a local microsection of the object to be examined.

Multicomponent analysis is performed as follows: the sample to be examined, which has a polished surface, is inserted into the vacuum chamber of the accelerator. First the sample surface to be examined is irradiated with a proton beam the energy of which ($500 \leqslant E_p \leqslant 1000$ keV) is chosen in accordance with the combination of the elements to be determined at the same time. The α particles which are formed as a result of the (p, α) reaction are recorded with a silicium surface-barrier detector having a solid angle of ∿0.8 sr. An ∿7-μm-thick aluminum foil is placed before the detector to protect it from elastically scattered protons and light. The pulses generated by the α particles incident on the detector are amplified and applied to a multichannel amplitude analyzer performing an energy analysis of the α particles which result from the (p, α) reaction at the nuclei of the elements to be determined [1, 2].

Translated from Atomnaya Énergiya, Vol. 53, No. 3, pp. 178-181, September, 1982. Original article submitted December 1, 1981.

0038-531X/82/5303-0648$07.50 © 1983 Plenum Publishing Corporation

Declassified and Approved For Release 2013/03/04 : CIA-RDP10-02196R000300010003-8

Declassified and Approved For Release 2013/03/04 : CIA-RDP10-02196R000300010003-8

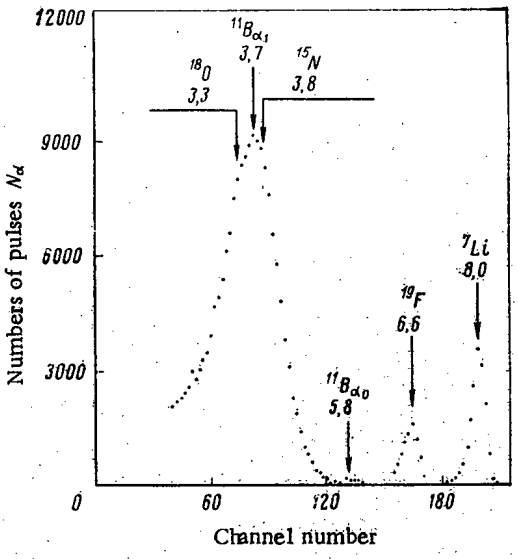

Fig. 1. Energy spectrum (MeV) of alpha particles emitted from nuclei of lithium, boron, nitrogen, oxygen, and fluorine irradiated with a proton beam having the energy E_p = 500 keV.

At proton energies of 500-1000 keV, ^{7}Li, ^{11}B, ^{15}N, ^{18}O, and ^{19}F have the greatest cross section of the (p, α) reaction among all the chemical elements [3]. For a simultaneous determination of the local concentration of lithium, boron, and fluorine and, in certain cases, of oxygen, a 500-600 keV proton beam is employed. The energy spectrum of the α particles originating from the nuclei of the elements to be analyzed is shown in Fig. 1 (E_p = 500 keV; angle of the detector relative to the incident beam 150°). It follows from Fig. 1 that the α particles emitted from lithium and fluorine with an energy of 8.0 and 6.6 MeV, respectively, are clearly recognizable on the spectrum. Boron, oxygen, and nitrogen emit α particles with an energy of 3.7, 3.3, and 3.8 MeV, respectively. Though oxygen and nitrogen emit α particles forming narrow peaks on the spectrum, and though the detector has high resolution, the peaks are covered by a broad α particle peak produced by boron. It was established in the epxeriments of [4] that at $500 \leqslant E_p \leqslant 600$ keV, nitrogen noticeably contributes to the total number of α particles only when the nitrogen concentration in the sample microsection under examination exceeds the boron concentration by about three orders of magnitude. In this case one must either use another method to determine local nitrogen-containing inclusions or determine the nitrogen concentration with an 850-1000 keV proton beam. The contribution of oxygen to the overall spectrum can be taken into consideration when the oxygen concentration exceeds the boron concentration in the sample microsection examined by a factor of more than 100. The reason is that the cross section of the (p, α) reaction at ^{18}O is smaller than the cross section of this reaction at ^{11}B by about two orders of magnitude in the proton energy interval of 500-600 keV [4]. When the form of the α particle spectra produced by oxygen and boron standards is known, the contribution of those elements to the resulting particular experimental spectrum can be assessed.

Once the number of recorded α particles corresponding to each element has been determined, the relative concentration of the elements in the sample can be found by comparison with standards. The standards are selected so that their density resembles that of the material of the test sample. For example, in the analysis of rocks, quartz and borax glass can be used as standards.

In the selective analysis of the local concentration of another combination of elements, e.g., of oxygen, nitrogen, and lithium, the proton energy must be within the limits $850 \leqslant E_p \leqslant 1000$ keV. In this interval, the cross section of the (p, α) reaction at nuclei of boron is substantially reduced but increased at nuclei of nitrogen and oxygen; therefore boron does not disturb the determination of the nitrogen and oxygen concentrations. If necessary, the presence of boron in an object under investigation can be determined with the (p, α) reaction at $500 \leqslant E_p \leqslant 600$ keV or with (n, α) radiography [1, 2].

Declassified and Approved For Release 2013/03/04 : CIA-RDP10-02196R000300010003-8

Declassified and Approved For Release 2013/03/04 : CIA-RDP10-02196R000300010003-8

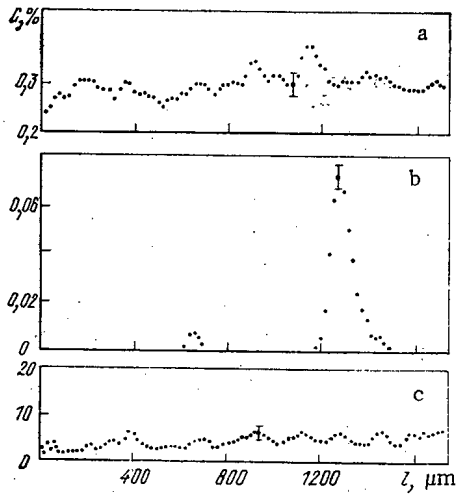

Fig. 2. Distribution of a) ^{11}B, b) ^{7}Li, and c) ^{19}F along a selected direction in a chondrite grain.

In order to determine the local concentration of beryllium, the sample surface under inspection is irradiated with an α particle beam with an energy of 2-2.5 MeV. The neutrons resulting from the (α, n) reaction are recorded with helium counters or proportional boron counters.

With this energy of the α particles, apart from beryllium only two elements emit neutrons, viz., oxygen and boron. The neutron yield resulting from beryllium nuclei is in this case about ten times greater than that of the boron nuclei and about one hundred times greater than that of the oxygen nuclei. In order to determine the number of neutrons emitted from beryllium nuclei, the boron and oxygen concentrations in the sample microsection under inspection must be known and their contribution to the total number of neutrons recorded must be brought into account. The beryllium concentration is determined from the number of neutrons recorded on the sample under inpsection and a standard, taking into account the background and the number of neutrons resulting from boron and oxygen nuclei. Beryllium foils and beryllium single crystals, in which the concentrations of beryllium, boron, and oxygen had been determined with another method, were used as standards for determining beryllium concentrations.

A multicomponent elementary analysis can be made in various ways: determination of the concentrations of lithium, beryllium, boron, oxygen, nitrogen, and fluorine in local microsections of an object, with the dimensions of the object being limited by the cross section area of a fixed ion beam; determination of the distribution of the cited elements by determining their local concentrations at several points situated in a certain direction or on a selected area (in this case the sample is shifted in well-defined steps parallel to selected directions); or determination of the distribution of the local concentration of the elements under consideration in a certain direction by continuous scanning with an ion beam.

In the first and second technique, the multichannel amplitude analyzer works in the multichannel counting mode and records the energy spectrum of the secondary radiation, e.g., of the α particles, when the local concentration of boron, lithium, oxygen, and fluorine or other combinations of these elements is to be determined. In the third technique, a simultaneous determination of the local concentration of elements is possible when several multichannel amplitude analyzers are employed (their number is given by the number of elements to be analyzed); the analyzers are connected in parallel in the measuring circuit. A multichannel amplitude analyzer in this case provides the distribution of a particular element along the time of scanning. The beam is made incident on the starting point of the scan by switching on the sawtooth voltage generator of the multichannel amplitude analyzer with a trigger pulse at the moment at which the charged particle beam starts to move in a particular direction. Multiple scanning substantially reduces the destruction of the object's surface by the charged particle beam in comparison with a fixed beam, because the time during which the beam dwells at each point on the line of scanning is reduced.

Declassified and Approved For Release 2013/03/04 : CIA-RDP10-02196R000300010003-8

Declassified and Approved For Release 2013/03/04 : CIA-RDP10-02196R000300010003-8

The main factors which define the limits of detecting elements with this technique are: maximum current density at which the charged particles do not yet burn the sample; the counting rate of the secondary radiation; and the presence of interfering elements and a background which affect the results of an analysis. Therefore, the maximum sensitivity and accuracy must be separately determined for each real object.

When no interfering elements are present, when the background is 1-5 pulses/h, when the counting rate is 100 pulses/h, and when the time of measurement is 1 h, the detection limits for the above elements in local microsections of objects are 10^{-5}% for lithium, 10^{-3}% for beryllium, 10^{-6}% for boron, 10^{-2}% for fluorine, 10^{-2}% for oxygen, and 1% for nitrogen. The statistical error of the measurements does not exceed 10%.

The technique was tested in several practical applications. For example, the elementary analysis of a technical beryllium foil was made to determine whether the foil could be used as a standard in determinations of the local concentration of beryllium. It was found that the particular foil had concentrations of beryllium, boron, lithium, and oxygen of 92.0, $1 \cdot 10^{-3}$, $6 \cdot 10^{-2}$, and 8.8%, respectively. Within the limits of the resolving power of the technique, the elements were found to be uniformly distributed in the foil. Impurity elements which were present set the applicability limit for the beryllium foil as standard in elementary analyses.

In order to determine the influence which the uniformity of the elementary distribution has upon the properties of ceramic ferroelectric materials, the lithium distribution was studied in these materials. The analysis was made by determining the local concentration of lithium at several points situated along the length of the object to be examined. It was found that the lithium was uniformly distributed in the sample and that the lithium concentration was (1.00 ± 0.04)% at a resolution of 20 μm of the technique.

A natural beryl crystal was analyzed to determine the composition of microimpurities in the crystal. It was found that the microimpurities contained beryllium, oxygen, boron, and lithium in concentrations of 5.2, 43.7, $2 \cdot 10^{-3}$, and 1.6%, respectively.

The spatial distribution of boron, lithium, and fluorine was studied on samples of the mineral chondrite. The analysis was made by continuously scanning the ion beam over the mineral grain to be examined. Each energy group of α particles emitted from boron, lithium, and fluorine was recorded with three multichannel amplitude analyzers. Figure 2 shows the spatial distribution of these elements in digital representation. In view of the dimensions of the grains and the required spatial resolution of the analysis, a beam size of 70 μm was adopted. In investigating this mineral with (n, α) radiography, a practically uniform distribution of the tracks on the detector was observed. A uniform distribution of boron (C_B = 0.30 ± 0.05%) was found in scanning the grain with a proton beam; in addition, local inclusions of lithium (up to 0.07%) were observed. In a subsequent detailed mineralogical analysis of a particular grain, inclusions of amber mica were found, and increased lithium concentrations are confined to this mica. The distribution of fluorine in the grain, as well as the distribution of boron, were practically uniform, with the concentration amounting to (5 ± 1)%. The investigation of the boron, lithium, and fluorine distributions in the chondrite grain made it possible to determine the migration paths of the elements during the formation of the mineral. This will help to develop criteria for the search for sites of the corresponding mineral.

The investigations have shown that this technique of elementary analysis facilitates the selective determination of the spatial distribution of certain elements and of their local concentrations. It is advantageous to introduce the spatial distribution of the elements to be analyzed in digital representation. Elementary analysis making use of charged particle beams can be used in, say, the development of techniques for introducing microimpurities in various melts and materials, for obtaining firm welded joints, for investigating the distribution of microimpurities of elements in crystals, for determining indicator minerals in the search for sites of useful minerals, etc.

The authors thank G. N. Flerov for suggesting this line of research and for useful discussions and S. V. Malinko for providing the minerals for the investigations.

Declassified and Approved For Release 2013/03/04 : CIA-RDP10-02196R000300010003-8

Declassified and Approved For Release 2013/03/04 : CIA-RDP10-02196R000300010003-8

LITERATURE CITED

1. I. G. Berzina et al., At. Energ., 44, No. 5, 418 (1978).
2. Nuclear Data Tables, A6, A7 (1969).
3. G. N. Flerov and I. G. Berzina, The Radiography of Minerals, Rocks, and Ore [in Russian], Atomizdat, Moscow (1979).
4. E. Ligeon and A. Bontemps, J. Radioanal. Chem., 12, No. 1, 335 (1972).

TECHNIQUE FOR PREPARING MICROFILTERS WITH HIGH SPECIFIC CAPACITY

G. N. Flerov, E. D. Vorob'ev,
V. I. Kuznetsov, V. A. Shchegolev,
G. N. Akap'ev, P. Yu. Apel',
T. I. Mamonova, and L. I. Samoilova

UDC 66.067.1

As is well known, the rate of flow of a fluid or gas through a filter is inversely proportional to its thickness. The thickness of the usual nuclear microfilter [1] is 10 μm, which does not always ensure high filter capacity, especially with small pore diameter. In order to increase the specific capacity of a filter, even thinner films can be used as the starting material, but it is extremely difficult to work with such filters, since their mechanical strength is inadequate.

In the present work, we investigated the possibility of obtaining microfilters with a thin filtering layer by irradiating a polymer film through a mask, consisting of a plate with openings, with accelerated ions with a free path in the bulk of the polymer less than the thickness of the film and with an irradiation dose that ensures complete subsequent etching of regions that are not protected by the mask to a depth equal to the path length of the ions. In the remaining thin polymer layer, it is possible to form a microporous structure by subsequent irradiation from the opposite side by ion beams with low intensity and with chemical working. The sections of the film protected by the mask with the first irradiation form a reinforced grid and ensure the necessary mechanical strength.

Formation of a Cellular Structure

Choice of Energy of Bombarding Particles. The minimum thickness of the filtering layer is limited by the spread of the particle path lengths. For the chosen ions ^{129}Xe with initial energy of 125 MeV, an approximate calculation using Bohr's equation gives a normal distribution of path lengths with standard deviation $\sim$0.03 μm. However, the variance of the energy losses and path lengths of particles passing through the absorbing layer greatly exceed the value predicted by the Bohr and Landau–Vavilov equations [2, 3]. In order to obtain results that are close to the experimental data, it is necessary to check the calculations using more complex techniques [4], but even in this case the desired result will not be achieved, since it is still necessary to include the inhomogeneity of the irradiated material (density fluctuations, presence of microinclusions).

We finally determined the energy of the bombarding particles and thickness of the starting film experimentally. In so doing, it is necessary to take into account the fact that the layer remaining after irradiation and etching must be as thin as possible and at the same time sufficiently strong and defect-free.

We performed the experiments with Dacron films with a thickness of 20 and 50 μm using ^{129}Xe and ^{40}Ar ion beams. The energy of the ions was varied with the help of absorbing foils. Good results were obtained by irradiating 20 μm films with 125-MeV xenon ions, whose average path length in Dacron was 17 μm. Since the film is inhomogenous over its thickness (up to ±1 μm), it is not expedient to use particles with longer path lengths.

Translated from Atomnaya Énergiya, 53, No. 3, pp. 181-182, September, 1982. Original article submitted November 3, 1981.

 0038-531X/82/5303-0652$07.50 © 1983 Plenum Publishing Corporation

Declassified and Approved For Release 2013/03/04 : CIA-RDP10-02196R000300010003-8

Declassified and Approved For Release 2013/03/04 : CIA-RDP10-02196R000300010003-8

TABLE 1. Specific Capacity of Anisotropic Filters*

Specimen number	Pore diam., μm	Porosity, %	Capacity with respect to distilled water, ml/min·cm²	Capacity with respect to air, liters/h·m²
25	0,2	6	20	$5{,}2\cdot10^6$
30	0,2	6	26	$5{,}2\cdot10^6$
38	0,2	6	38	$4{,}4\cdot10^6$
39	0,2	6	58	$6{,}4\cdot10^6$
53	0,55	5	70	$8{,}1\cdot10^6$

*Pressure differential is 101.325 Pa.

Choice of Etching Conditions. As a result of etching, the material in the region irradiated by ions must be completely removed. It was found that for an irradiation density of $5\cdot10^9$ particles/cm² etching over a period of 15 min in a 6 moles/liter NaOH solution at 50°C from the irradiated side of the film is sufficient. Here, many channels from separate tracks coalesced, forming a "well" with a thin bottom. It is evident that as a result of the spread of the ion path lengths, the thickness of a thin layer is not necessarily equal to the difference between the film thickness l_0 and the average free path R_0, while depending on the chemical etching time it can be somewhat longer or shorter than $l_0 - R_0$. The duration of etching was chosen so that the average thickness of the bottom of the "well" was equal to 2 μm. This value was determined with the help of conductometric measurements during the etching process, as well as by optical observations of specimens and their sections.

Formation of a Porous Filtering Layer

The following order of operations is chosen for working the starting film:

Irradiation through the mask by 125-MeV ^{129}Xe ions with a track density equal to $5\cdot10^9$ particles/cm² (the condition $R_0 + 3\ \mu m \approx l_0$ is satisfied);

irradiation of the entire film surface from the opposite side with ^{129}Xe ions. The density of tracks was 10^7-10^8 particles/cm² (the condition $3\ \mu m < R_0 < l_0$ is satisfied);

etching of the film from the side of the first irradiation.

As a result of a single etching, we obtained simultaneously well-shaped depression in the starting matrix and a formed, porous structure in the filtering layer.

Comparison of the Characteristics of Cellular and the Usual Nuclear Filters

Comparative measurements of the specific capacity of the usual nuclear filters and filters prepared using the technique described above were performed (see Table 1). In order to make a quantitative comparison, we point out that the specific capacity of the usual nuclear filters with pore diameters 0.2 μm and porosity 6% is 5.4 ml/min·cm² for water and $1.8\cdot10^6$ liters/h·m² for air; for filters with pore diameter 0.55 μm and 5% porosity these values are 33 ml/min·cm² and $4.0\cdot10^6$ liters/h·m², respectively (these characteristics were measured with a pressure differential of 101.325 Pa). The pore diameter and density were monitored with the help of a transmission ÉMMA-2 electron microscope. The transparency of the mask through which the first irradiation was performed was 55%. Three hundred specimens were prepared and studied. It was established after the measurements that the capacity of the new type of filters is 3 to 4 times greater than the capacity of the filters with the usual structure with a thickness of 10 μm. The mechanical strength of the cellular microfilters permits performing all the necessary operations during the course of filtration. In addition, during the filtration process, contact with the substrate does not decrease the effective area of the cellular filter. In the future, using improved methods of physicochemical processing, strong cellular structures could be obtained with a filtering layer having a thickness of 0.5 μm and less.

LITERATURE CITED

1. G. N. Akap'ev et al., "Technique for making nuclear filters," Dep. st. OIYaI, Dubna (1974), B1-14-8214.

Declassified and Approved For Release 2013/03/04 : CIA-RDP10-02196R000300010003-8

Declassified and Approved For Release 2013/03/04 : CIA-RDP10-02196R000300010003-8

2. K. Schmidt et al., Nucl. Instrum. Methods, 134, No. 1, 157 (1976).
3. H. Schmidt-Bocking and H. Hornung, Z. Phys., A286, No. 3, 253 (1978).
4. A. F. Burenkov et al., Preprint IAE-3337/9, Moscow (1980).

Declassified and Approved For Release 2013/03/04 : CIA-RDP10-02196R000300010003-8

Declassified and Approved For Release 2013/03/04 : CIA-RDP10-02196R000300010003-8

RUSSIAN JOURNALS IN THE PHYSICAL AND MATHEMATICAL SCIENCES

AVAILABLE IN ENGLISH TRANSLATION

ALGEBRA AND LOGIC
Algebra i Logika
Vol. 21, 1982 (6 issues) $270

ASTROPHYSICS
Astrofizika
Vol. 18, 1982 (4 issues) $320

AUTOMATION AND REMOTE CONTROL
Avtomatika i Telemekhanika
Vol. 43, 1982 (24 issues) issues) $495

COMBUSTION, EXPLOSION, AND SHOCK WAVES
Fizika Goreniya i Vzryva
Vol. 18, 1982 (6 issues) $345

COSMIC RESEARCH
Kosmicheskie Issledovaniya
Vol. 20, 1982 (6 issues) $425

CYBERNETICS
Kibernetika
Vol. 18, 1982 (6 issues) $345

DIFFERENTIAL EQUATIONS
Differentsial'nye Uravneniya
Vol. 18, 1982 (12 issues) $395

DOKLADY BIOPHYSICS
Doklady Akademii Nauk SSSR
Vols. 262–267, 1982 (2 issues) $145

FLUID DYNAMICS
Izvestiya Akademii Nauk SSSR, Mekhanika Zhidkosti i Gaza
Vol. 17, 1982 (6 issues) $380

FUNCTIONAL ANALYSIS AND ITS APPLICATIONS
Funktsional'nyi Analiz i Ego Prilozheniya
Vol. 16, 1982 (4 issues) $320

GLASS AND CERAMICS
Steklo i Keramika
Vol. 39, 1982 (6 issues) $460

HIGH TEMPERATURE
Teplofizika Vysokikh Temperatur
Vol. 20, 1982 (6 issues) $400

HYDROTECHNICAL CONSTRUCTION
Gidrotekhnicheskoe Stroitel'stvo
Vol. 16, 1982 (12 issues) $305

INDUSTRIAL LABORATORY
Zavodskaya Laboratoriya
Vol. 48, 1982 (12 issues) $400

INSTRUMENTS AND EXPERIMENTAL TECHNIQUES
Pribory i Tekhnika Eksperimenta
Vol. 25, 1982 (12 issues) $460

JOURNAL OF APPLIED MECHANICS AND TECHNICAL PHYSICS
Zhurnal Prikladnoi Mekhaniki i Tekhnicheskoi Fiziki
Vol. 23, 1982 (6 issues) $420

JOURNAL OF APPLIED SPECTROSCOPY
Zhurnal Prikladnoi Spektroskopii
Vols. 36–37 (12 issues) $420

JOURNAL OF ENGINEERING PHYSICS
Inzhenerno-fizicheskii Zhurnal
Vols. 42–43, 1982 (12 issues) $420

JOURNAL OF SOVIET LASER RESEARCH
A translation of articles based on the best Soviet research in the field of lasers
Vol. 3, 1982 (4 issues) $95

JOURNAL OF SOVIET MATHEMATICS
A translation of Itogi Nauki i Tekhniki and *Zapiski Nauchnykh Seminarov Leningradskogo Otdeleniya Matematicheskogo Instituta im. V. A. Steklova AN SSSR*
Vols. 18–20, 1982 (18 issues) $680

LITHOLOGY AND MINERAL RESOURCES
Litologiya i Poleznye Iskopaemye
Vol. 17, 1982 (6 issues) $420

LITHUANIAN MATHEMATICAL JOURNAL
Litovskii Matematicheskii Sbornik
Vol. 22, 1982 (4 issues) $205

MAGNETOHYDRODYNAMICS
Magnitnaya Gidrodinamika
Vol. 18, 1982 (4 issues) $325

MATHEMATICAL NOTES
Matematicheskie Zametki
Vols. 31–32, 1982 (12 issues) $400

continued on inside back cover

Declassified and Approved For Release 2013/03/04 : CIA-RDP10-02196R000300010003-8